

UNIVERSITY OF NOVA GORICA
GRADUATE SCHOOL

**ELECTRONIC TRANSPORT PROPERTIES OF
GRAPHENE AND GRAPHENE-RELATED
MATERIALS**

DISSERTATION

Srinivasa Rao Pathipati

Mentor: Prof. Dr. Gvido Bratina

Nova Gorica, 2014

UNIVERZA V NOVI GORICI
FAKULTETA ZA PODIPLOMSKI ŠTUDIJ

**TRANSPORT ELEKTRIČNEGA NABOJA V
GRAFENU IN GRAFENSKIH MATERIALIH**

DISERTACIJA

Srinivasa Rao Pathipati

Mentor: Prof. Dr. Gvido Bratina

Nova Gorica, 2014

ACKNOWLEDGEMENTS

It is a pleasure to thank the many people who made this thesis possible.

Working in the group *Prof. dr. Gvido Bratina* has been one of the most challenging and knowledge building experiences in my career so far. I thank him for providing that impetus to succeed while enjoying my work. In addition I would particularly like to acknowledge the encouragement and freedom he gave for self motivated ideas. His suggestions and discussions have always led me back on track whenever I have been lost or confused.

I am indebted to *Dr. Egon Pavlica* for streamlining my thoughts to work in the right direction, for instilling in me dedication towards every aspect of work however small it might be and for having supported me both technically and personally.

First of all I would like to thank my master thesis supervisor *Dr. Vikas Rana*, who introduced me to organic electronics.

I am indebted to *Prof. dr. Vincenzo Palermo, Emanuele Treossi, Andrea Schierf* from CNR, Bologna for a fruitful and friendly collaboration. Thank you so much!

I am thankful to *Prof. dr. Xinliang Feng, Akimitsu Narita, Parvez Khaled* from Max Planck Institute, Mainz for a fruitful and friendly collaboration. Thank you very much!

I am very grateful to my friend, philosopher and guide *G. Venkateswara Rao*, who encouraged me throughout my career.

I specially would like to thank the colleagues *Raveendra, Mirela, Metka, Jampani, Iulia, Qinggou Liu, Artem Badasyan, Katerina, and Uroš* for their help.

My sincere gratitude to all my teachers from my school to IIT Delhi.

Now it is a pleasure for me to thank all my friends and my family members.

I specially would like to thank all our secretaries in the department and special thanks for *Vesna*. All of them have been very helpful in arranging the things on time. A special “thank you” go to *Tea*, she has been very helpful in making my arrival and stay in Slovenia possible.

And last but the most important of all, I am grateful to my beloved wife *Sridevi* and my parents, for being always with me and for taking care of me, no matter what their physical condition and coordinates are.

ABSTRACT

Graphene, an atom thick layer of carbon, has attracted a lot of attention due to its peculiar properties like ballistic transport, zero band gap, high mobility and ease of modulation of its electrical properties. Graphene has zero density of states where the conduction and valence band meet and has very low density of states near the Dirac point. Since graphene is one atom thick, its whole volume is exposed to the surroundings and its properties are very sensitive to the surrounding atmosphere including temperature, substrate and adsorbate molecules. The most established technique for the production of high-quality graphene is mechanical exfoliation. But this method is limited to very small areas. An alternative scalable, high yield and cost-effective method for the production of graphene involves the reduction of graphene oxide. Electrical characterization of reduced graphene oxide (rGO) shows ambipolar behavior similar to that of mechanically exfoliated graphene, albeit with moderate performance. Due to the presence of oxygen functionalities, carbonyls, epoxies and holes, the charge transport in rGO is a complex process that can include transport on extended states of graphene via variable range hopping and/or on percolation, resulting in conductivity being three orders of magnitude lower than the conductivity of exfoliated single-layer graphene. When rGO is exposed to suitable organic molecules, it shows significant effects on charge transport properties. The ability to control charge transport in rGO through exposure to adsorbates is of considerable importance, given the high level of processability of this material, excellent conductivity and its possible applications in the fields of composites, structural materials and electronics.

Electrical charge transport in semiconductors is typically studied by monitoring the current of the charge carriers that are either photogenerated or injected from metallic electrodes into the organic semiconductor (OS). But the ohmic contacts for the OS are prerequisite for the lossless transport, which is difficult to find especially for ambipolar OSs, like graphene-related materials. In order to avoid the role of metal/OS interface, we have employed photogeneration inside the OS layer, and the drift current of the charge carriers under the applied bias, known as displacement current measured in the external circuit. This method is called time-of-flight (TOF) photocurrent measurement technique.

Our rGO-based field effect transistor (FET) measurements reveal that the

connectivity of graphitic domains has important implications on the conductivity, as well as on mobility. In addition to that we have performed TOF measurements on rGO on different substrates like fused silica, sapphire and Si/SiO₂. The mobilities estimated on rGO on Si/SiO₂ from both FET and TOF measurements are in good agreement. The conductivity of rGO on fused silica and sapphire is two orders of magnitude higher than rGO on SiO₂, due to the well connected regions of graphitic domains. Previous reports indicate that the resistance between the graphene flakes is higher than resistance of an individual flake. The coupling between the adjacent nanosheets (high internanosheet resistance) is an important factor for the device performance. The conduction is limited by hopping between individual graphitic domains.

The first part of this thesis explores the effect of controlled amount of adsorbates on the electronic properties of rGO by charge transport measurements and state-of-the-art TOF technique. For this purpose we have chosen both p-type dopants and n-type dopants. We have chosen pyrene compounds, 1-pyrene butyric acid (PBA) and 1-pyrene sulfonic acid sodium salt (1-PSANa), which are weak electron acceptors and also strong electron acceptors like tetracyanoethylene (TCNE) and tetrafluoro-tetracyanoquinodimethane (F4-TCNQ). We have chosen tetrathiafulvalene (TTF), which is an electron donor. The conductance of rGO based FETs is measured with these adsorbates to investigate relationship between added adsorbates and the symmetry of the Dirac-like conductance. The measurements demonstrate that the molecules with electron withdrawing groups shifts the conductivity minimum towards the positive gate voltages (p-type doping) and the molecules with electron donating group shifts the conductivity minimum towards negative gate voltages (n-type doping). In addition, the molecules with cyano groups (TCNE and F4-TCNQ) completely suppress the electron mobility and pyrene compounds reduce the electron mobility moderately. These results indicate that the level of doping depends upon the charge transfer between the adsorbates and rGO.

We have performed TOF measurements on rGO on fused silica to gain deeper insight into charge transport mechanism between rGO and adsorbates. When the electron acceptors are present on the surface of rGO, electron charge transfer takes place from rGO to adsorbate, leaving a hole in rGO. These localized holes act as traps for electrons, increasing thereby the transit time for the charge carriers, and

reducing the electron mobility. By using time-resolved photocurrent measurements we were able to detect a reduction of electron mobility in rGO for coverage as low as 0.08% of PBA. The same effect is also observed with 1-PSANa and the reduction of electron mobility is observed for coverage of 1.3×10^{-10} moles/cm² on rGO for the first three coverages and then the electron mobility is slightly recovered. This effect is also observed with TCNE on rGO, but the amount of increase in transit time is relatively large compared to pyrene compounds on rGO. With increasing the surface coverage, the molecular interaction between the negatively charged ions increases, hence the charge transfer between rGO and adsorbates decreases. The trend of variation of transit time with the applied bias is same for all the materials and the variation of transit time depends on the charge transfer. These measurements reveal that the capture probability for the charge carriers at lower velocities is higher, than at higher voltages, where the velocity of charge carriers is higher. The molecules with cyano groups not only reduce the electron mobility but also reduce the electron photocurrent and make the determination of the transit time unreliable.

TOF measurements on rGO with TTF shows effect on hole mobility. Due to the absorption in TTF at the excitation wavelength in rGO, the electron photocurrent and hole photocurrent decreases, but the transit time for the electrons doesn't change. But due to presence of TTF molecules, the electrons are transferred from TTF into rGO and recombine with the holes in rGO, consequently the hole photocurrent is completely quenched. TOF measurements show the extreme sensitivity of rGO to the adsorbates.

The next part of the thesis deals with the improving the charge carrier mobility of organic semiconductors. Solution processed organic field-effect transistors (OFETs) usually have high I_{on}/I_{off} ratio but suffer from low mobilities. Graphene has high mobility but low on/off ratio. Here we have explored the possibility of improving the mobility OSs by mixing with graphene nanoflakes (GNs). We have exploited poly(3-hexylthiophene) (P3HT) and N,N'-0-1H,1H-perfluorobutyl dicyanoperylene carboxydiimide (PDIF-CN2) as two representatives of p-type and n-type OSs. We have used FET-based measurements to assess their transport properties. These highly conducting and highly ordered GNs act as conducting bridges between the grains of OSs. The charge carriers starting from the source electrode flows some part in low conductivity OS and some part in high

conductivity GNs, thereby reducing the channel length, hence the transconductance can be improved as well as the mobility. The mobility in blend P3HT and GNs shows an improvement at low concentration, but decreases at higher concentrations. The I_{on}/I_{off} ratio continuously decreases with increasing the concentration and reaches the graphene I_{on}/I_{off} ratio. Due to the presence of non-percolation networks, the on current increases and the presence of percolation networks increases the off current. As the concentration of GNs increases, the separation between the GNs drops and the charge carriers in graphene starts to percolate through low conductive OS, consequently, the off current increases and hence the I_{on}/I_{off} ratio decreases. These GNs not only improve the I_{off} current but also disturb the molecular ordering of P3HT molecules, which is also decreases the mobility. In addition, the energy level alignment between the GNs and OS is a prerequisite for the lossless transport. Due to the mismatch between the highest occupied molecular orbital (HOMO) and the work function of graphene, contact resistance exists resulting in a bottle neck for flow of charge carriers. As the number of interconnecting junctions increase, the contact resistance between these interfaces dominates the channel resistance, consequently the mobility drops. With further increasing the concentration of GNs, agglomeration of them taking place.

We have used both TOF and FET based measurements to assess transport properties of GNs and PDIF-CN2. These two materials have similar solubility that are typically used for processing of perylenediimides such as chloroform, and similar position of Fermi level with respect to the lowest occupied molecular orbital (LUMO) in PDIF-CN2. The mobility estimated from FET based measurements increases from $1.3 \times 10^{-4} \text{ cm}^2/\text{Vs}$ to $0.2 \text{ cm}^2/\text{Vs}$ in PDIF-CN2 without and with the addition of GNs. The mobility estimated from the TOF measurements by exciting the charge carriers in PDIF-CN2 at 530 nm wavelength has increased from $10^{-4} \text{ cm}^2/\text{Vs}$ to $3 \times 10^{-3} \text{ cm}^2/\text{Vs}$ upon addition of GNs in PDIF-CN2. The difference between the absolute value of the mobility is due to difference between the two experiments and the assumption of constant electric field. When the carriers excited in graphene at 210 nm incident wavelength, the transit time shifted to shorter times resulting in mobility of $\mu=0.1 \text{ cm}^2/\text{Vs}$. This is one order of magnitude higher than the mobility of electrons obtained with low-energy photons and compares to the mobility obtained with FETs. The hot electrons generated at this wavelength, move through the blends

of GNs and PDIF-CN2 (GN:PDIF-CN2) layer, essentially absent of lattice, vibronic and electronic polarizations. Their only significant recombination events are likely to occur at the GN:PDIF-CN2 interfaces.

But the blends are limited to materials that can be solution processed only. This method introduces the problem of contact resistance due to number of interconnecting junctions and energy level misalignment. In addition to that molecular ordering of organic molecules will be disrupted due to addition of GNs into OS matrix. We have proposed an alternative approach to avoid the problems that are encountered in blends, by placing mechanically exfoliated micron-sized graphite flakes between the source drain electrodes. The P3HT saturation mobility has increased from 10^{-4} cm²/Vs to 0.01 cm²/Vs with the incorporation of graphite flakes without decreasing the on/off ratio. Since the charge carriers take advantage of the highly conducting graphite flakes, thereby reducing the effective channel length and reducing the interconnecting junctions and hence the improvement in the mobility. But the main difficulty in this method is in the control over the number of graphene layers and the size of the flakes. Also it is difficult to place them in the desired locations of the wafer precluding thereby the use of the top contact (TC) configuration.

To avoid the problem of controlling of the flake size and surface coverage, we have proposed an alternative approach that can replace the mechanically exfoliated graphite flakes. Single-layer-graphene (SLG) flakes produced by the electrochemically exfoliation method are deposited on the Si/SiO₂ surface by dip coating method. The size of the flake is from several μm to 30 μm. Hence we can reduce the number of interconnecting junctions and the surface coverage can be easily controlled. The P3HT linear mobility has increased from 0.005 cm²/Vs to 0.2 cm²/Vs in the TC configuration. The linear mobility has increased from 2.2×10^{-3} cm²/Vs to 0.033 cm²/Vs in the bottom contact (BC) configuration. The 40 fold improvement in the mobility in TC configuration and 15 fold improvement in the BC configuration is due to the presence of graphene flakes in the conduction channel. In addition to that only I_{on} increases, I_{off} doesn't and these graphene flakes are p-type due to chemical residues that are present on the surface due to the solvent, thus reduces the barrier for hole injection into P3HT. FET with BC configuration is inferior to that of the TC configuration FET with the same active material. The

reduction of FET performance on BC configuration results from poor thin film growth on and close to metal contact electrodes due to large surface energy difference between the electrodes and gate dielectrics. The poor growth results in lowering of charge carrier mobility and also causes large electric contact resistance between FET-channel and contact electrodes.

Since graphene has no band gap, thus limits its potential for electronic applications. Quantum confinement of the charge carriers induces a band gap. This dissertation examines the electronic properties of graphene nanoribbons (GNRs) formed by intramolecular oxidative cyclodehydrogenation of polyphenylene precursors at the microscopic level as a function of channel length. The intrinsic mobility of these individual GNR is relatively high. These GNRs are characterized by FET measurements and TOF technique. These GNRs are synthesized with insulating alkyl chains at the edges, which will act as traps for the charge carriers. This is evidenced by the hysteresis in the transfer characteristics of FET and mobility decreases with increasing channel length. As the channel length increases, the carriers will encounter more traps which will reduce the mobility.

Key words: graphene, reduced graphene oxide, charge transport, time-of-flight, organic transistor, adsorbates, doping, blends, perylenes, polythiophene, graphene nanoribbons.

POVZETEK

Grafen, en atom debela plast ogljika, je pritegnil veliko pozornosti zaradi svojih značilnih lastnosti, kot so balističen transport, odsotnost energijske špranje, visoka gibljivost elektronov in enostavnost modulacije električnih lastnosti. V točki, kjer se stikata prevodni in valenčni pas (Diracova točka), je v grafenu gostota stanj enaka nič. Ker je grafen debel en atom, je njegov celoten volumen izpostavljen okolici in njegove lastnosti so zelo občutljive na atmosfero vključujoč temperaturo, substrat in adsorbirane molekule. Najbolj uveljavljena tehnika za proizvodnjo visoko kakovostnega grafena je mehanski piling, vendar je ta metoda omejena na zelo majhne površine. Alternativna visoko donosna, stroškovno učinkovita in razširljiva metoda za pripravo grafena vključuje zmanjšanje grafen oksida. Električna karakterizacija zmanjšane plasti grafena oksida (rGO) kaže ambipolarno vedenje podobno kot mehansko (exfoliated) plastoviti grafen, čeprav z zmerno uspešnostjo. Zaradi prisotnosti funkcionalnosti kisika, karbonili (carbonyls), epoksidne smole in lukenj, je gibanje nabojev v rGO kompleksen proces, ki lahko vključuje gibanje na razširjenih stanjih grafena, poskakovanja (hopping) ali perkolacijo, kar povzroči tri velikostne rede nižjo prevodnost od prevodnosti plastovitega enoplastnega grafena. Ko je rGO izpostavljen ustreznim organskim molekulam, kaže znaten učinek na lastnosti gibanja nabojev. Precejšen pomen daje sposobnost nadzora gibanja naboja v rGO, preko izpostavljanja adsorbentom, saj visoka predelovalna stopnja tega materiala, odlična prevodnost in njegove morebitne aplikacije na področju kompozitov, strukturnih materialov in elektronike.

Električni prenos naboja v polprevodnikih se običajno preučuje s spremljanjem toka nosilcev naboja, ki so bodisi foto-vzbujeni ali preneseni iz kovinskih elektrod v organske polprevodnike (OP). Vendar ohmski kontakti za OS so predpogoj za "lossless" promet, ki ga je težko najti zlasti za ambipolarne OP, kot so snovi podobne grafenu. Z namenom, da bi se izognili vplivu stika kovine / OP, smo uporabili foto-generacijo naboja znotraj OP plasti in prenesli tok nosilca naboja z uporabo napetosti, znan kot premikalni tok izmerjen v zunanjem tokokrogu. Ta metoda je znana kot foto-tokovna merilna tehnika čas preleta (time of flight - TOF).

FET meritve na osnovi reduciranega grafen-oksida (rGO) so pokazale, da imajo grafitne domene pomemben vpliv na prevodnost, kot tudi na gibanje elektronov. V nadaljevanju smo izvedli TOF meritve na rGO na različnih substratih,

kot so kremen, safir in Si/SiO₂. Ocenjene mobilnosti na rGO na Si/SiO₂ pridobljena iz obeh meritev (FET in TOF) dobro sovpadajo. Prevodnost rGO na kremenovi in safirni podlagi je za dva velikostna razreda višja od rGO na SiO₂, zaradi dobro povezanih področji grafitnih domen. Dosedanje objave kažejo na to, da je upornost med skupki grafenovih plasti (flakes) večja od upornosti med posameznimi plastmi. Sklopitev med sosednjimi nanolističi (med katerimi je visoka upornost) je pomemben dejavnik delovanja naprave. Prevodnost je omejena na preskakovanja med posameznimi grafitnimi domenami.

Prvi del te disertacije razkrije efekt kontrolirane količine adsorbentov na elektronske lastnosti rGO z merjenjem gibanja nabojev in najsodobnejšo tehniko "času preleta" (TOF). Za te namene smo izbrali obe vrsti dopantov, tj. p-tip in n-tip. Izbrali smo spojine pirena, 1-piren masleno kislino (butanojska kislina) – PBA in 1-piren sulfonsko kislino z natrijevo soljo (1-PSANa), katera je šibak prejemnik elektronov in tudi močne prejemnike elektronov, kot sta tetracianoetilen (TCNE) in tetrafluoro-tetracianoquinodimetan (F4-TCNQ). Izbrali smo tetrathiafulvalen (TTF), kateri je donator elektronov. Delovna prevodnost TTF-jev na rGO podlagi je izmerjena z uporabo omenjenih adsorberjev z namenom poizvedovanja razmerja med dodanim adsorbentom in simetrijo Dirac (delovne) prevodnosti. Meritve kažejo, da molekule z elektron-odvzemajočimi funkcionalnimi skupinami premikajo minimum prevodnosti proti pozitivnim napetostim na vratih (p-tip dopiranje) in, da v molekulah z elektron-oddajajočimi funkcionalnimi skupinami premikajo minimum prevodnosti proti negativnim napetostim na vratih (n-tip dopiranje). Poleg tega, molekule s ciano skupinami (TCNE in F4-TCNQ) popolnoma zatirajo gibanje (mobilnost) elektronov, spojine s pirenom pa znatno znižajo mobilnost elektronov. Slednji rezultati kažejo, da je stopnja dopiranja odvisna od prenosa naboja med adsorbenti in rGO.

Izvedli smo TOF meritve rGO na kremenu (fused silica) z namenom podrobnejšega vpogleda na mehanizem prenosa naboja med rGO in adsorbenti. Ko so prejemniki elektronov prisotni na površini rGO, prenos elektronskega naboja steče iz rGO na adsorbat, kar povzroči vrzeli v rGO. Te lokalizirane vrzeli delujejo kot pasti za elektrone, s čimer večajo čas prehoda za nosilce naboja in zmanjšujejo gibljivost elektrona. Z uporabo časovno rešene foto-tokovne meritve, smo zaznali zmanjšano gibljivost elektronov v rGO za pokritost, ki znaša 0,08% PBA. Podoben

pojav je ugotovljen tudi pri 1-PSANa, kjer je zaznano zmanjšanje mobilnosti elektronov za pokritost 1.3×10^{-10} mol/cm² na rGO za prve tri pokritosti, potem se gibanje elektronov rahlo povrne. Ta pojav je tudi zaznan pri uporabi TCNE na rGO, ampak je količina povečanja časa prenosa relativno visoka v primerjavi s pirenovimi spojinami na rGO. Z večanjem pokritosti površine, se zvišuje molekularna interakcija med negativno nabitimi ioni, zato se prenos naboja med rGO in adsorbenti znižuje. Trend variacije v času prenosa za uporabljen napetosti, je enak za vse materiale in variacije časa prenosa so odvisne od prenosa naboja. Te meritve razkrivajo, da je za nosilce naboja verjetnost zajema pri nižjih hitrostih večja, kot pri višjih napetostih, kjer je hitrost nosilcev naboja večja. Molekule s ciano skupinami ne samo znižujejo gibljivost elektrona, ampak tudi znižujejo elektronski foto-tok in s tem nezanesljivo ugotavljanje časa prenosa. TOF meritve na rGO s TTF kažejo vpliv na gibljivost vrzeli. Zaradi absorpcije v TTF pri vzbujevalni valovni dolžini v rGO, se elektronski fototok in vrzeli fototoka znižujejo, ampak se čas prehoda za elektrone ne spremeni. Ampak zaradi prisotnosti molekul TTF, so elektroni preneseni iz TTF v rGO, kjer se prerazporedijo z vrzeli v rGO in posledično je fototok vrzeli popolnoma zaustavljen. TOF meritve kažejo ekstremno občutljivost rGO na adsorbate.

Naslednji del disertacije obravnava izboljšanje gibljivosti nosilcev naboja v organskih polprevodnikih. Organski tranzistorji z učinkom polja, kojih izdelamo iz raztopine (Organic field-effect transistors (OFETs)) imajo navadno visoko razmerje $I_{\text{vklop}}/I_{\text{izklop}}$, ampak trpijo nizko gibljivost. Grafen ima visoko gibljivost ampak nizko razmerje $I_{\text{vklop}}/I_{\text{izklop}}$. V tej točki smo raziskali možnosti izboljšanja gibljivosti OSs z umešanjem grafenovih nanolističev (GNs). Uporabili smo poli(3-heksil tiofen) (P3HT) in N,N0-1H, 1H – perfluorobutil dicianoperilen carboxydiimide (PDIF-CN2) kot dva predstavnika za p-tip in n-tip OSs. Uporabili smo meritve na bazi OFET za ocenitev njihovih gibalnih lastnosti. Ti zelo prevodni in zelo urejeni GN-ji se delujejo prevodni mostovi med zni OS-jev. Nosilci naboja, ki izhajajo iz elektrode, tečejo v določenem delu skozi nizko prevodno OS in v določenem delu skozi visoko prevodne GN-je, s čimer zmanjša dolžino kanala, zato je mogoče izboljšanje transprevodnosti ter gibljivosti elektronov. Gibljivost v zmesi P3HT in GN kaže na izboljšanje pri nizkih koncentracijah, vendar znižanje pri visokih koncentracijah. Razmerje $I_{\text{vklop}}/I_{\text{izklop}}$ se nadaljnje znižuje z večanjem koncentracije in doseže razmerje $I_{\text{vklop}}/I_{\text{izklop}}$ grafena. Ob prisotnosti neperkolacijskih mrež se tok vklopa

zveča, v prisotnosti perkolacijskih mrež pa se zveča tok izklopa. Če se koncentracija GN-jev zvišuje, se znižuje ločevanje med GN-ji in nosilci naboja v grafenu pričnejo perkolirati skozi nižje prevodne OS, kar posledično povzroči zvišanje toka izklopa in znižanje $I_{\text{vklop}}/I_{\text{izklop}}$ razmerja. Ti GN-ji ne samo izboljšajo izklopni tok, ampak tudi motijo molekularno urejenost P3HT molekul, katerim se tudi zniža gibljivost. Dodatno, poravnava nivoja energije med GN in OS je predpogoj za manjšo izgubo med prenosom. Zaradi neuskklajenosti med najvišje zasedenimi molekulskimi orbitalami (HOMO) in delovnimi funkcijami grafena, se kontaktna upornost kaže v zmanjšanem pretoku nosilcev naboja. Ker se število povezovalnih križišč povečuje, kontaktna upornost med temi vmesniki dominira upornosti kanala kar posledično zniža gibanje. Z dodatnim povečevanjem koncentracije GN-jev nastopi aglomeracija.

Uporabili smo TOF in OFET meritve za oceno lastnosti prenosa GN-jev in PDIF-CN2. Ta dva materiala imata podobno topnost, ki se običajno uporablja za predelavo perilendiimidov, kot so kloroform ter podobni s položaji v ravni Fermi, glede na najnižjo zasedeno molekularno orbito (LUMO) v PDIF-CN2. Gibljivost ocenjena z osnovami OFET meritev narašča od $1,3 \times 10^{-4} \text{ cm}^2/\text{Vs}$ za $0,2 \text{ cm}^2/\text{Vs}$ v PDIF-CN2 brez in z dodatkom GN-jev. Gibljivost, ocenjena z TOF meritvami z vzbujanjem nosilcev naboja v PDIF-CN2 pri valovni dolžini 530 nm se je povečalo iz $10^{-4} \text{ cm}^2/\text{Vs}$ na $3 \times 10^{-3} \text{ cm}^2/\text{Vs}$ ob dodatku GN-jev v PDIF-CN2. Različne absolutne vrednosti gibljivosti je posledica razlik med eksperimentoma in predpostavkah o konstantnem električnem polju. Ko so nosilci stimulirani v grafenu pri valovni dolžini 210 nm se čas prenosa skrajša, kar se kaže v gibljivosti $\mu = 0,1 \text{ cm}^2/\text{Vs}$. To je en red velikosti višje kot gibljivost elektronov pridobljena z nizkoenergijskimi fotoni in je primerljivo z gibljivostjo pridobljeno z OFET. Vroči elektroni ustvarjeni na tej valovni dolžini, se premikajo skozi plast zmesi GNjev in PDIF-CN2 (GN:PDIF-CN2), v bistvu z odsotnostjo mrežne (lattice), vibronske in elektronske polarizacije. Njihova edina znatna rekombinacija se lahko pojavi pri GN:PDIF-CN2 vmesnikih.

Vendar so mešanice omejene le na materiale, ki se jih lahko obdela kot raztopine. Ta metoda se sooča tudi s problemom kontaktne upornosti zaradi številnih medsebojno povezanih stičišč in neporavnosti energijskih nivojev. Poleg tega je molekularna urejenost organskih molekul motena zaradi dodajanja GNs v OS matriko. Z namenom, da bi se izognili tem težavam, smo predlagali drugačen pristop,

pri čemer plastoviti grafit mikronske velikosti mehansko postavimo med izvirne in ponorne *elektrode*. Mobilnost P3HT nasičenosti se je povečala z 10^{-4} cm^2/Vs na 0.01 cm^2/Vs z vključitvijo grafitnih lističev, brez zmanjšanja razmerja vklop/izklop. Ker je za nosilce naboja uporaba visoko prevodnih grafitnih plasti velika prednost, se učinkovita dolžina kanala in medsebojno povezana stičišča zmanjšajo, kar pripomore k večji mobilnosti. Toda glavna težava pri tej metodi je nadzor nad številom grafitnih plasti in njihove velikosti. Prav tako je težko postaviti grafitne plasti na določeno mesto v celotni strukturi, kar izključuje uporabo konfiguracije zgornjega stika. Da bi se izognili problemu kontroliranja velikosti lističev in površinske pokritosti, smo predlagali drugačen pristop, ki lahko nadomesti mehansko eksfoliacijo lističev. Eno-plastoviti grafitni (single-layer-graphene-SLG) lističi, pripravljene z elektrokemično eksfoliacijo se tako odložijo na površino Si/SiO₂ z metodo potapljanja. Velikost lističev je od nekaj μm do 30 μm . Tako lahko zmanjšamo število stičišč, poleg tega pa lahko zlahka kontroliramo prekritje površine. Linearna mobilnost P3HT se je povečala z 0.005 cm^2/Vs na 0.2 cm^2/Vs v TC konfiguraciji. Tudi v konfiguraciji spodnjega kontakta (bottom contact-BC) se je linearna mobilnost povečala z 2.2×10^{-3} cm^2/Vs na 0.033 cm^2/Vs . 40-kratno povečanje v TC konfiguraciji in 15-kratno v BC konfiguraciji dosežemo zaradi prisotnosti grafitnih lističev v prevodnem kanalu. Poleg tega smo pokazali, da se povečuje samo I_{on} , medtem ko se I_{off} ne in da so grafitni lističi p-tipa zaradi kemičnih ostankov, ki so prisotni na površini zaradi topila, kar zmanjšuje energijsko bariero za prenos vrzeli v P3HT. OFET s konfiguracijo BC je slabša od OFET s konfiguracijo TC z enakim aktivnim materialom. Zmanjšanje OFET učinkovitosti v BC konfiguraciji izvira iz slabe rasti tankega filma na in v bližini kovinske kontaktne elektrode zaradi velike razlike površinske energije med elektrodami in vrati. Slaba rast znižuje mobilnost nosilnega naboja in povzroča tudi veliko električno kontaktno upornost med FET-kanalom in kontaktnimi elektrodami.

Grafen nima prepovedanega pasu, kar omejuje potencial materiala za uporabo v elektronskih aplikacijah. Kvantno zajetje nosilcev naboja povzroči prepovedan pas. Ta disertacija proučuje elektronske lastnosti grafitnih nano-trakov (graphene nanoribbons-GNRs), pripravljenih z intramolekularno oksidativno ciklohidrogenacijo polifenilenskih prekurzorjev na mikroskopskem nivoju z odvisnostjo od dolžine kanala. Intrinzična mobilnost posameznih GNR je relativno

visoka. GNRs so karakterizirani s FET meritvami in TOF metodo. GNRs smo sintetizirali z izolacijo alkilnih verig na robovih, ki bodo delovale kot pasti nosilcev naboja. To je razvidno iz histereze prenosne karakteristike FET in zmanjšane mobilnosti z večanjem dolžine kanala. Z večanjem dolžine kanala, se namreč nosilci naboja srečajo z več pastmi, ki zmanjšajo njihovo mobilnost.

Ključne besede: grafen, reduciran grafenov oksid, transport naboja, čas preleta, organski tranzistor, adsorbati, dopiranje, zmesi, perileni, politiofeni, grafenski nanotrakovi

Contents

Chapter 1: Introduction	1
1.1 Introduction.....	1
1.2 Synthesis of graphene	6
1.2.1 Mechanical exfoliation.....	6
1.2.2 Graphene on metal surfaces by chemical vapor deposition.....	7
1.2.3 Reduced graphene oxide	9
1.2.4 Electrochemical exfoliation.....	10
1.2.5 Graphene nanoribbons.....	12
1.3 Potential for applications.....	13
1.4 Motivation for this research work.....	14
1.5 Summary of each chapter.....	14
Chapter 2: Theory and experimental methods	16
2.1 Charge transport in disordered materials	16
2.2 Time-of-flight method.....	17
2.2.1 Sandwich time-of-flight method (S-TOF)	18
2.2.2 Coplanar time-of-flight method (C-TOF)	19
2.3 Sample preparation and experimental details of C-TOF	20
2.4 Determination of transit time: Dispersive and non-dispersive transport.....	21
2.4.1 Non-dispersive charge transport.....	21
2.4.2 Dispersive charge transport.....	24
2.5 Scher and Montroll model.....	26
2.6 Bässler's Gaussian disorder model.....	27
2.7 Conditions to be met for TOF measurements	29
2.7.1 Metal/organic semiconductor interface and blocking contacts.....	29
2.8 Field-effect transistor characterization.....	30
2.9 Atomic force microscope (AFM).....	33
Chapter 3: TOF measurements on reduced graphene oxide and effect of	

adsorbates.....	36
3.1 TOF measurements on rGO on fused silica, sapphire and Si/SiO ₂	36
3.2 The effect of doping in graphene.....	48
3.2.1 Hysteresis in graphene field effect transistors.....	48
3.3 P-type doping of rGO with 1-pyrene butyric acid.....	52
3.3.1 Introduction.....	52
3.3.2 Experimental.....	53
3.3.3 Results and Discussion.....	53
3.4 N-type doping of graphene with tetrathiafulvalene.....	60
3.4.1 Introduction.....	60
3.4.2 Experimental.....	61
3.4.3 Results and Discussion.....	61
3.5 Conclusions.....	65
Chapter 4: Comparison of effect of weak and strong electron acceptors on rGO.....	67
4.1 Materials.....	67
4.2 Experimental.....	69
4.3 Results and Discussion.....	69
4.4 Conclusions.....	81
Chapter 5: Electric charge transport in blends between graphene nanoflakes and organic semiconductors.....	83
5.1 Graphene/P3HT blends.....	83
5.1.1 Experimental.....	84
5.1.2 Results and Discussion.....	85
5.2 Graphene/PDIF-CN ₂ blends.....	90
5.2.1 Experimental.....	92
5.2.2 Results and Discussion.....	93
5.3 Improvement of mobility of organic semiconductors with mechanically exfoliated graphene flakes.....	101
5.3.1 Experimental.....	101
5.3.2 Results and Discussion.....	102

5.4 Conclusions.....	104
Chapter 6: Performance enhancement of OFETs using graphene flakes and characterization of graphene nanoribbons.....	106
6.1 Performance enhancement of P3HT-based FETs with electrochemically exfoliated graphene flakes.....	106
6.1.1 Experimental.....	108
6.1.2 Results and Discussion.....	109
6.2 Graphene nanoribbons.....	113
6.2.1 Experimental.....	114
6.2.2 Results and Discussion.....	114
6.3 Conclusions.....	119
Chapter 7: Summary of the thesis.....	120
List of publications:	124
Appendix A.....	125
Appendix B.....	126
Appendix C.....	127
Appendix D.....	128
References.....	129

Chapter 1: Introduction

1.1 Introduction

The building block of all organic materials is carbon, which can form a variety of hybridization states with the neighboring carbon atoms like sp , sp^2 , sp^3 . Carbon is available in 3-dimensional (3-D) forms: diamond (sp^3 hybridization) and graphite (sp^2 hybridization). Later new allotropes of carbon were discovered. Fullerenes (0-dimensional (0-D)), nanotubes (1-dimensional (1-D)) and recently graphene (2-dimensional (2-D)) were discovered. Some of the carbon allotropes are presented in Fig. 1.1.

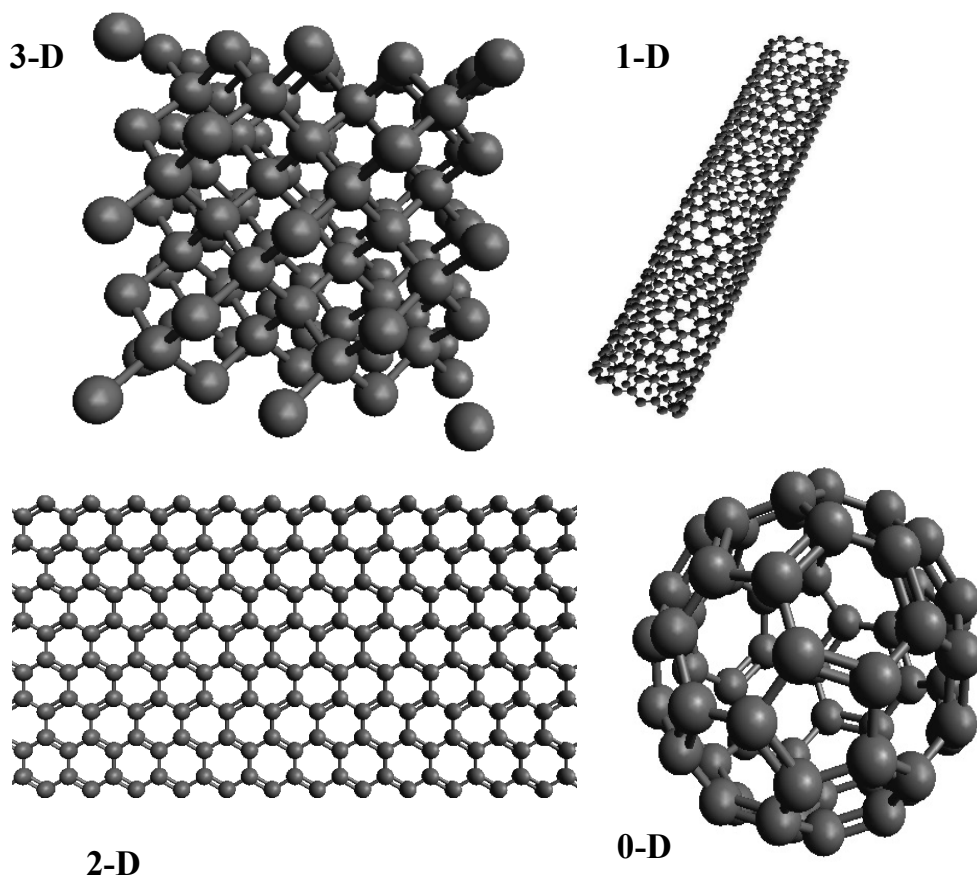


Figure 1.1: Some allotropes of carbon: diamond (3-dimensional), carbon nanotubes (1-dimensional), graphene (2-dimensional) and fullerenes (0-dimensional).

Graphene is a planar material, which can be easily integrated over large areas on a wafer, effectively eliminating the controllability problem. Graphene fills the

bridge between the 3D materials to 1D carbon nanotubes (CNTs). Graphene has benzene-like structure with each carbon atom bonded with 3 carbon atoms in sp^2 hybridization. Nanostructures of this element have generated interest ever since fullerenes were discovered [1]. CNTs offer the advantage of replacing the conducting channel in the field-effect transistors, due to its high mobility up to $100,000 \text{ cm}^2/\text{Vs}$ [2]. CNTs have always been hampered by the intrinsic difficulty of controllably placing the desired types of nanotubes in the desired locations on a wafer. Such a method has not been discovered yet. Recently graphene is replaced with CNTs which have outstanding electrical properties [3].

Electronic energy band structure of graphene was first studied theoretically by Wallace [6] in 1947, and he explained its behavior as a semimetal due to the lack of an energy gap between the valence and conduction bands and vanishing density of states at the point where the conduction and valence band meet.

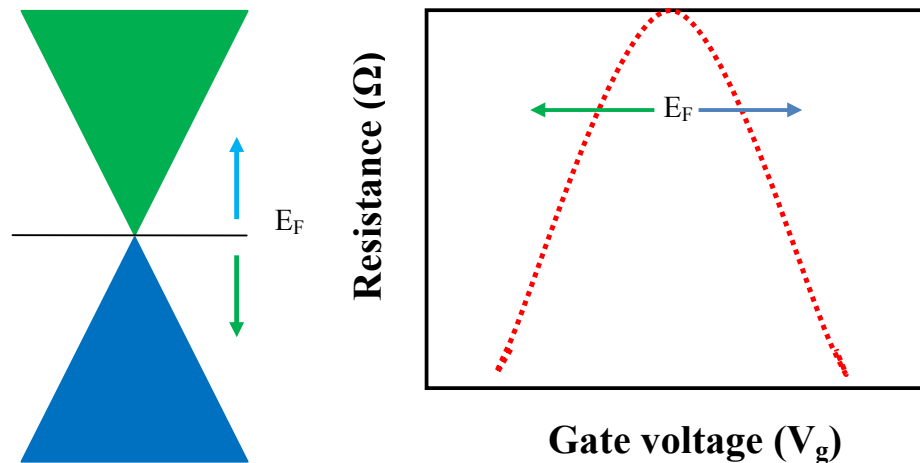


Figure 1.2: Electric field effect of a graphene device. The Fermi level of graphene is modulated using a gate electric field. A peak in the resistance will be observed when the Fermi level coincides with the Dirac point (zero density of states).

Recently A. Geim and K. S. Novoselov [3] revisited this material in 2004 and were awarded the Noble prize in 2010 for their investigation of this material. Graphene has many interesting properties like its ambipolar conductance behavior, and the ease of modulation of properties by surface dopants, external electric field (field-effect), and magnetic field (quantum Hall effect) [7]. In graphene-based field-effect transistors (GFETs), the carrier concentration and the carrier type can be

controlled using the gate voltage. The Fermi level can be shifted to valence or conduction band using the external electric field as shown in Fig. 1.2. While applying a variable external electric field to graphene, an ambipolar field effect is observed. The conductance has a minimum value at a certain applied electric field equal to zero in the absence of nearby trapped charges; this point is believed to be the charge neutrality point where the Fermi level in the graphene sits at the Dirac point [3]. Also, a zero conductance region is not observed due to the lack of an energy gap in graphene. The unique properties of graphene stem from its purely two-dimensional (2D) lattice structure. Its electronic structure can be derived by a nearest-neighbor, tight-binding approximation [6]. An important feature of the graphene energy spectrum is its resemblance to the Dirac spectrum for massless fermions [9]. As a result, quasi-particles in graphene exhibit a linear dispersion relation, $E = \hbar \vec{k} v_f$, where E is the energy, \hbar is the Planck's constant, \vec{k} is the wavevector and v_f is the Fermi velocity. The particles in graphene exhibit Fermi velocity of $v_f \sim c/300$, where c is the velocity of light [24].

The nature of the low density of states near the Dirac point makes the electronic properties of graphene very sensitive to the surroundings. Graphene has a high surface-to-volume ratio and its electrical performance is closely related to its surrounding environment, including substrate and its roughness, impurities present on the substrate, humidity and temperature [10]. Thus its electrical properties such as mobility and charge carrier density are very sensitive to the adsorbates. GFETs offer a novel approach for the characterization of molecular adsorption to planar graphitic surfaces via electrical detection. Hence GFETs can be used for single molecule detection [10]. However, precise control of the carrier type and carrier concentration in graphene is required for further development of graphene-based nanoelectronics. In addition to that, effective and controllable doping has to maintain high mobility of graphene. Doping in graphene can be obtained in two ways: substitutional doping and surface transfer doping. Substitutional doping refers to substitution of carbon atoms in the honey-comb lattice of graphene by atoms with different number of valence electrons. But this method disrupts the sp^2 hybridization of carbon atoms. A convenient way of doping graphene is via surface charge transfer doping, in which charge transfer occurs from graphene to the adsorbed dopant. The charge carrier concentration and type can be easily controlled by the molecular adsorption via

charge transfer between graphene and adsorbates at a controlled rate [115]. The charge transfer between graphene and adsorbates depends upon the type of adsorbate, its interaction with increasing concentration, and its adsorption mode. Therefore, understanding the changes in the electronic properties of graphene has the key importance to design of the graphene-based devices and to control their properties. The changes in electrical properties of graphene have been coupled to charge transfer between graphene and adsorbates and change in the position of Fermi level in graphene and metal work function [10]. Charge transfer is determined by the relative position of density of states (DOS) of the highest occupied molecular orbital (HOMO) and lowest unoccupied molecular orbital (LUMO) of the dopant and the Fermi level of graphene.

Frequently, in order to extract the information on charge transport properties in semiconducting materials three-terminal field-effect transistors (FETs) and two-terminal planar devices by the time-of-flight (TOF) photocurrent measurements were employed. In FETs, the role of metal/semiconductor interface is difficult to separate, and the contact resistance plays an important role on the device performance. In order to avoid the role of metal/semiconductor interface, we have employed photogeneration inside the channel to create free carriers inside organic semiconductor (OS) layer, and monitored the time evolution under the influence of applied electric field. Understanding the time dependence of the photogenerated current is important to understand its physical origin and to predict the behavior of OS under different conditions.

The main aim this thesis work is to understand how the charge transport properties of graphene are changing when exposed to different type of adsorbates at submonolayer coverages by the TOF technique. For this purpose we have chosen different type of molecules: Pyrene compounds, which are weak electron acceptors and tetracyanoethylene and tetrafluoro-tetracyanoquinodimethane, which are strong electron acceptors. In addition, we have chosen tetrathiafulvalene, which is an electron donor in order to achieve n-type doping. We have carried out transport measurements on graphene without and with adsorbates by the TOF method and also by the FET characterization. In addition, to have a better understanding we have carried out transport measurements both by the TOF technique and FET characterization with increasing concentration of adsorbates and how the adsorbate-

adsorbate interaction changes the charge transfer between graphene and adsorbates at submonolayer coverages.

OSs can be processed from solution at low cost and on different substrates, making it possible to produce light-weight, large-area flexible electronic applications. The solution-processed organic field-effect transistors (OFETs) suffer from low mobility but exhibit high I_{on}/I_{off} ratio. Although efforts have been made to improve the mobility of these materials, the need for high mobility OS is still compelling. Recent efforts dealing with organic semiconductor/carbon nanotube hybrid field-effect transistors [168-172], which have reported shows a remarkable increase in field-effect mobility resulting from CNTs having been inserted into or beneath the semiconductor film. These studies suggest that CNTs act as conducting bridges between the crystalline regions of the semiconductor film. However, the I_{on}/I_{off} ratio appears to decrease just as the mobility begins to increase. This is because the charge carriers in 1D CNTs start to percolate. As the concentration of CNTs reaches the percolation threshold I_{on}/I_{off} ratio decreases rapidly, thus limits the maximum mobility achievable. Along the same lines we have explored the possibility of using graphene flakes into or beneath the organic semiconductor film instead of CNTs produced by chemical exfoliation, mechanical exfoliation and electrochemical exfoliation. Since graphene is a 2D material, it has large conducting channel compared to CNTs which is 1D material. Thus we expect that graphene would improve the mobility of charge carriers compared to CNTs. In order to exploit simultaneously the excellent electronic properties of graphene and the easy of processability of OSs, efforts have been addressed to the use of blends of soluble graphene with OS in FETs [173]. In addition, since graphene is an ambipolar material, we expect that it would improve the mobility of both p-type and n-type material. In this thesis work, with the aim of enhancing the effective mobility of OS, we have developed blends containing both OS and graphene nanoflakes (GNs). We have characterized these graphene/OS composite films both by the FET characterization and TOF technique. But this method is applicable only to materials that can be solution processed only. It is expected that the electrical properties of these blends, and in particular their charge transport characteristics, depend significantly on the graphene/OS ratio used, and on the relative arrangement of the graphene sheets into the OS matrix. These blends can have a complex structure.

However, the solvents for OSs and compatibility of graphene nanoflakes with the OSs are limited. In case of poor solubility graphene nanoflakes, they can be phase separated and forming aggregates. In order to avoid the problem of solubility of materials, we have placed mechanically exfoliated graphene flakes and electrochemically exfoliated graphene flakes beneath the OS layer in the FET channel. Since the charge flow takes place in the first few monolayers of the OS, we expect that the FET mobility can be improved substantially.

Since many electronic applications rely on the use of a semiconductor with a finite band gap, thus limiting the use of graphene for these applications. Transport gap in the graphene spectrum can be obtained by carving graphene into a narrow ribbon, or a graphene nanoribbon. In this dissertation, we examine the charge transport properties of graphene nanoribbons at the macroscopic level produced by the intramolecular oxidative cyclodehydrogenation of polyphenylene precursors using TOF technique and FET characterization.

1.2 Synthesis of graphene

After the first isolation of graphene by Geim *et al.* [3], researchers developed several methods for the production of graphene. The state-of-the-art in production techniques to make graphene, which we used in this work are briefly explained below.

1.2.1 Mechanical exfoliation

This technique involves repeated peeling off thick graphite by a Scotch tape. After repetition of exfoliation several times, the Scotch tape is pressed onto the surface of a Si/SiO₂ substrate it leaves single-layer-graphene (SLG) and few-layer-graphene (FLG) flakes, whose optical interference contrast can be observed under an optical microscope. The sizes of these flakes are typically from 10 μm to 100 μm. The films produced by this method, exhibit mobility up to 10,000 cm²/Vs, show 98% transparency in the visible region and exhibit the quantum hall effect, which indicates their high-quality [3, 7, 8]. Optical microscope image of graphene flakes on Si/SiO₂ substrate of thickness 300 nm is shown in Fig.1.3. Single-layer-graphene flakes and few-layer-graphene flakes are indicated.

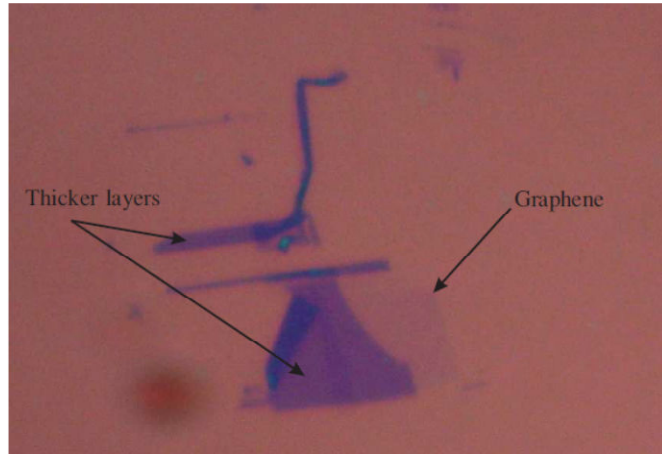


Figure 1.3: Graphene flakes on Si/SiO₂ substrate of thickness 300 nm under an optical microscope. Single-layer-graphene (SLG) flakes and few-layer-graphene (FLG) flakes are indicated.

However, the yield of this method in the production of SLG flakes is limited on laboratory-scale.

1.2.2 Graphene on metal surfaces by chemical vapor deposition

The most promising and readily accessible approach for deposition of reasonably high quality graphene is chemical vapor deposition (CVD) onto transition metal substrates such as Ru [14], Ir [15], Ni [16-18], and Cu [19-23]. In particular, a recent development on uniform SLG deposition on copper foils over large areas has allowed access to high-quality material [20, 21]. Although CVD of graphene on copper is relatively new, several groups around the world have already reported excellent device characteristics such as mobilities of up to 16,000 cm²/Vs [21] at room temperature and large area growth (up to 75 cm along the diagonal direction) [20]. This process involves decomposition of carbon precursors at elevated temperatures onto a metallic substrate, which plays the role of a catalyst for graphene growth. The grain size of the graphene layer depends on the grain size of the metal substrate. Upon contact with the metal substrate the precursor carbon atom dissolves in the metal and starts forming bonds with the neighboring carbon species. The thickness of the graphene layer is mainly controlled by the solubility of carbon in the metallic substrate. Copper has lowest solubility compared to all other metals, hence the quality of the graphene films on copper is relatively good. Carbon solubility and

growth conditions ultimately define the morphology and thickness of the graphene films [21]. Growth of graphene on Cu substrates has so far shown the best results in terms of uniform deposition of SLG over as large as 75 cm. The films have sheet resistances as low as 125 Ω /sq with 97.4% optical transmittance, and exhibit the half-integer quantum Hall effect, indicating their high quality [20-23].

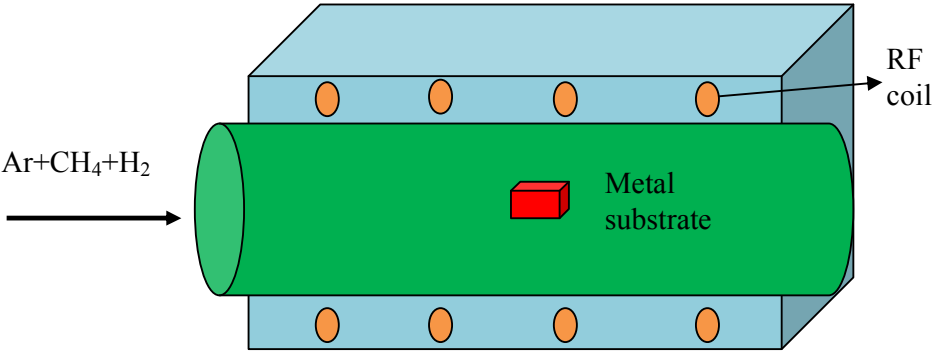


Figure 1.4: Schematic illustration of the growth process for the synthesis of graphene using chemical vapor deposition (CVD).

The schematic shown in Fig. 1.4 depicts the system setup employed in the CVD deposition of graphene layers. The metallic substrate is loaded into the furnace and then it is heated to the elevated temperature by radio frequency (RF) coils.

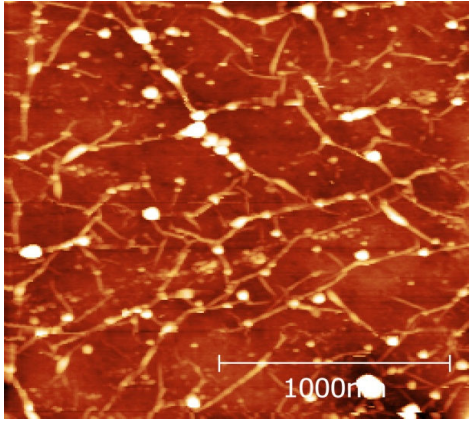


Figure 1.5: 2 μ m \times 2 μ m atomic force microscope (AFM) image of graphene on copper foil. The height scale is 0 to 12 nm.

A carbon precursor like methane gas is introduced to the system and hydrogen catalyzes the reaction between methane and the copper, separating the hydrogen and carbon in the methane, and depositing the carbon onto the copper. The atomic force

microscope (AFM) image of topography of graphene on copper foil is shown in Fig. 1.5. The ripples and wrinkles are formed on the graphene layer. These are formed by differential thermal expansion, as the metal contracts more than the graphene during post growth cooling, leaving an excess area of graphene.

1.2.3 Reduced graphene oxide

The most exciting advantages of this method are its relative low-cost and potential scalability. The starting material is graphite, and the technique can easily be scaled-up to produce gram-quantities of chemically-derived graphene, dispersed in liquids. Owing to its superior mechanical properties of graphene oxide (GO) is also an interesting material in its own right for applications in composites [25, 26]. GO is an insulator, removal of oxidative species is required to retain its conductivity. Three steps are involved in this process of obtaining graphene.

1. Oxidation of graphite
2. Exfoliation of graphite oxide.
3. Reduction of graphene oxide.

1. Oxidation of graphite: GO has been mainly produced by the Brodie [27], Staudenmaier [28] or Hummer [29] methods. These methods involve oxidation of graphite in the presence of strong acids and oxidants. Hummer's method is relatively well established and involves combination of potassium permanganate and sulfuric acid. The degree of oxidation can be controlled by the oxidizing agents, synthesis conditions and the precursor graphite used. The active species in the oxidation process are dimanganese heptoxide (Mn_2O_7). The oxidation process starts with the defects in the graphite flake which act as seeds to start oxidation. After several steps graphite is functionalized with oxygen containing groups.

2. Exfoliation of graphite oxide: Functionalization of graphite with oxygen-containing groups causes weakening of the van der Waals forces between the layers, which facilitates exfoliation in aqueous solutions. Resulting graphene oxide suspensions are placed in an ultrasonic bath and then centrifuged in order to remove thick graphite flakes. High powers of ultrasonication can destroy the graphite sheets, so that sonication has decisive significance in determining the flake size. The resulting solution is deposited onto the desired substrate either by spin-coating or

drop-casting.

3. Reduction of graphene oxide: The carbon framework of GO can be restored by either thermal annealing or by treating with chemical reducing agents. Earlier efforts mainly involved the use of hydrazine vapor for this purpose [30]. The use of hydrazine, however, requires great care because it is both, highly toxic and potentially explosive. Therefore, there have been a number of alternative techniques explored. Sodium borohydride was demonstrated to effectively reduce the graphene oxide [36], but the process is slow, because it is slowly hydrolyzed in water. Several other reductants have also been used for the reduction of graphene oxide including hydroquinone [37], gaseous hydrogen [38], vitamin C (ascorbic acid) [39] and strongly alkaline solutions [40]. Further improvements are developed to reduce graphene oxide by treating with Hydrogen plasma and finally reduced by thermal annealing in high vacuum or inert gas atmosphere [41].

The rGO samples studied in this thesis work were prepared by the group of Vincenzo Palermo, Istituto per la Sintesi Organica e la Fotoreattività, Bologna, Italy.

1.2.4 Electrochemical exfoliation

Mechanically exfoliated graphene exhibit mobility up to $10,000 \text{ cm}^2/\text{Vs}$ but are not suitable for large-area production [3]. CVD growth of graphene films on metallic substrates gives large area films but it involves high temperature and also expensive substrates [19-24]. Chemical route based on Hummer's method for making GO, followed by reduction into graphene either thermally or chemically are more advantageous because of its low cost and large area production [31-35]. But this method also involves high temperature processing and the resistivities of the resulting layers are from $1 \text{ k}\Omega$ to $70 \text{ k}\Omega/\text{sq}$. In this method the structure of graphene can't be completely recovered and oxygen functionalities are still present. Liquid phase exfoliation and expansion of graphite by intercalates micron size graphene flakes [42]. The resistance of these films is from 5 k to $8 \text{ k}\Omega/\text{sq}$ and the transparency of these films in the visible region is 83-90% [42, 44, 45]. This method involves the immersion of highly oriented pyrolytic graphite into the electrolyte solution, which will act as intercalant. Many different electrolytes for the electrochemical exfoliation, including HBr, HCl, HNO₃, and H₂SO₄ have been examined, and only the electrolytes containing H₂SO₄ exhibit ideal exfoliation efficiency. The size of

electrochemically exfoliated graphene films ranges from several μm to 30 μm .

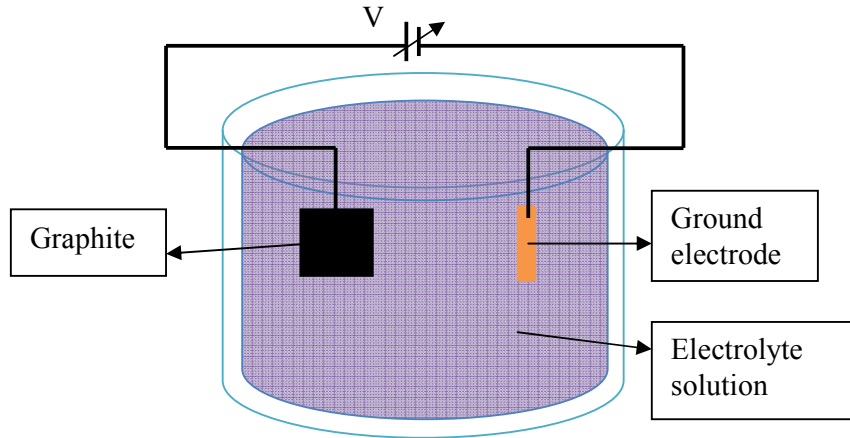


Figure 1.6: Schematic illustration of electrochemical exfoliation of graphite [46].

The schematic illustration of electrochemical exfoliation of graphite is as shown in Fig. 1.6. Here graphite will act as one electrode, while the other metallic electrode which acts as a grounded electrode will also immersed in the electrolyte solution. Initially, low bias is applied between the electrodes in the solution, to make acidic ions completely wet the sample and likely causes the gentle intercalation of ions to the grain boundaries of graphite. Then a high bias is applied between the electrodes and ramped between the positive the negative voltages until graphite is completely exfoliated. The acidity of the solution causes oxidation of graphite. In order to reduce the level of oxidation KOH-like solution can be added.

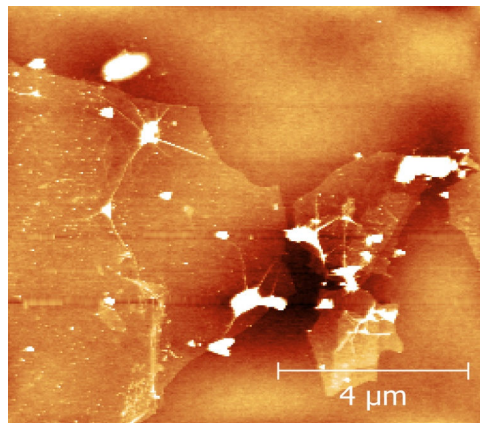


Figure 1.7: $10\mu\text{m}\times 10\mu\text{m}$ AFM image of the electrochemically exfoliated graphene flakes on Si/SiO₂ substrates.

AFM image of topography of SLG flakes produced by this method is shown

in Fig. 1.7. These flakes are predominantly SLG flakes and of variable size. The chemical residues of the solvent are present on the surface, which is used to dissolve these flakes.

The electrochemically exfoliated graphene samples studied in this thesis work were prepared by the group of Xinliang Feng from Max Planck Institute for Polymer Research, Ackermannweg, Mainz, Germany.

1.2.5 Graphene nanoribbons

Graphene is a high mobility material but its potential for applications is limited due to the lack of an electron energy bandgap. But the quantum confinement of the carriers induces a bandgap. It has been proved both experimentally [47] and theoretically [49] that the width and the edge structure of GNRs governs their electronic properties. Top-down and bottom-up approaches have been established for the production of GNRs. There are top-down approaches developed for the reliable and reproducible build-up of well defined GNRs for precise lateral and longitudinal dimension like lithographic cutting of graphene [48], longitudinal unzipping [50], etching of carbon nanotubes [54,55] and the surface-assisted extraction from graphite dispersions. But these methods give low yield and lack of structural precision. Another method is bottom-up chemical synthetic approach based on solution-mediated [56, 59, 61, 62], surface assisted [63], cyclodehydrogenation namely graphitization, planarization of tailor made three dimensional polyphenylene precursors.

GNRs produced by solution-mediated methods give limited amount of material, which is further bound to a metal surface, and so impedes wider applications in electronics [59, 61]. On the other hand, surface assisted assemblies of GNRs have to be characterized by STM and also give low yield [63]. Large scale processing of GNRs relies on intramolecular oxidative cyclodehydrogenation of polyphenylene precursors [64].

The electrochemically exfoliated graphene samples studied in this thesis work were prepared by the group of Xinliang Feng from Max Planck Institute for Polymer Research, Ackermannweg, Mainz, Germany.

1.3 Potential for applications

The high mobility of the charge carriers and ease of doping in graphene makes it a promising candidate for future electronics [10]. The biggest issue concerning GFET is the lack of an energy gap at the Dirac point, where the valence and conduction bands meet. The carrier mobility of 200,000 cm²/Vs has been measured in suspended samples [11] and 20,000 cm²/Vs on the substrate [65]. Perhaps even more relevant for electronics than carrier mobility is saturation velocity. Graphene has been shown to have a saturation velocity of up to 5×10⁷ cm/s on a silicon dioxide substrate [66]. This is a five-fold increase over the saturation velocity in silicon, 1×10⁷ cm/s. Graphene, however, has one major advantage that may allow it to succeed where carbon nanotubes have not. Graphene is a planar material, which means in principle, it can be seamlessly integrated into well-developed top-down fabrication processes.

Graphene's two-dimensional structure has other advantageous differences from both bulk 3-D materials and conventional 2-dimensional electron gas (2DEG), since all of its atoms are exposed on the surface, it can be easily doped either chemically or electrostatically. In combination with the ambipolar band structure and the linear density of states at low energies, this allows for the fabrication of graphene heterostructures with n- and p-type graphene separated by sharp electric field gradients [67], and also makes graphene a useful material for chemical sensing [68], or for applications like solar cells, where control of the workfunction is important.

Graphene is also studied for spintronic applications. In addition graphene, can absorb only 2.3% visible light and its workfunction is nearly the same as that of In_xSb_{1-x}O (ITO), which makes graphene a promising candidate as an electrode for solar cells. Graphene is extremely light and extremely strong material. Its composites may replace steel that can reduce weight.

In addition to that graphene may act as a source drain electrode material for organic field effect transistors (OFETs). Recently it has been proved that the transconductance of OFETs based on the solution-processed organic materials can be improved by making blends of them. Graphene-based supercapacitors will likely be developed for use in low energy applications such as smart phones and portable computers.

1.4 Motivation for this research work

The SiO₂-supported graphene devices are highly disordered due to SiO₂'s surface roughness, impurities of charges distribution and surface optical phonons. As a one-atom-thick monolayer crystal, graphene has very high surface-area-to-volume ratio. Thus, its electrical performance is closely related to its surrounding environment. Frequently, even slight changes in the surrounding conditions can induce significant effects to the performance; include temperature, moisture or the organic residue left on top of graphene during the device fabrication. As the size of objects reaches the nanometer scale, surface properties gradually dominate owing to the increasing surface-area-to-volume ratio. It is therefore important not only to thoroughly understand the surface structure but also to engineer the surface in a controllable way. In this thesis, modifying the surface chemical and physical processes will be carried out in a controllable way and characterized at submonolayer coverages through charge carrier transport measurements and advanced time-of-flight (TOF) technique.

One of the most often asked questions when working with graphene transistors is, why the conduction through a graphene flake changes while exposed to different environments, mainly in ambient or organic molecules. Is still not clear whether this change is caused by chemical reactions occurring at the surface of the flake or in the oxide layer beneath it, or by a physical phenomena taking place at the interface of the oxide layer and the graphene flake, or even a combination of all of the above. As demonstrated in this thesis, superior sensitivity of the TOF technique allowed us to probe the role of sub-monolayer coverages of adsorbates on charge transport properties of graphene.

OFETs exhibit low mobility but high I_{on}/I_{off} ratio. GFETs on the other hand exhibit high mobility but suffer from low I_{on}/I_{off} ratio. Since graphene is an ambipolar material it can improve the mobility of charge carriers of both p-type and n-type materials.

1.5 Summary of each chapter

The first chapter includes the background, properties, applications and motivation of the research. The second chapter gives the theoretical background

necessary for the analysis of the coplanar time-of-flight (C-TOF) photocurrent measurements, experimental setup, and its limitations. It also describes the different models that are used to explain the dispersive and non-dispersive charge transport and to determine the transit time.

The first part of the third chapter includes the transport properties of reduced graphene oxide (rGO) by the TOF technique on different substrates like fused silica, sapphire and on Si/SiO₂ and its FET characterization. The second part of the third chapter describes the concept of doping and the effect of adsorbates on rGO, and their modulation of the charge transport behavior. It also includes the quantitative analysis of the p-type and n-type doping of graphene with p-type and n-type dopants.

The fourth chapter consists of the modulation of charge transport properties with strong electron acceptors by the conventional FET characterization and by the TOF technique.

The fifth chapter focuses on the improvement of organic semiconductors by making FETs with blends of P3HT (Poly 3-hexylthiophene) and graphene nanoflakes. We have presented the study of variation of mobility and I_{on}/I_{off} ratio of P3HT with varying concentration of graphene nanoflakes. The second part of this chapter contains the experimental results obtained on the PDI (perylene-diimide)-graphene blends by the TOF technique at different wavelengths and the FET characterization. Experimental results obtained on FETs by incorporating mechanically exfoliated graphene in the channel between the source and drain electrodes are presented the end of the chapter.

The first part of sixth chapter includes an alternative approach to enhance the performance of P3HT-based FETs by incorporating electrochemically exfoliated graphene and the second part of the chapter includes the experimental results on the graphene nanoribbons characterized by the FET and TOF technique at the microscopic level. The main conclusions are reported in the seventh chapter.

Chapter 2: Theory and experimental methods

This chapter describes sample preparation and experimental set up of TOF measurements, the theory necessary for the estimation of the transit time for dispersive and nondispersive charge transport and the models that explain the charge transport behavior. The experimental setup for the characterization of the FETs and the working principle of the atomic force microscope (AFM) for the surface analysis is also included.

2.1 Charge transport in disordered materials

The charge transport in disordered organic semiconductors is via hopping as charge carriers must overcome large barriers between the molecules or localization sites [155]. In a region of crystalline order, the charge carrier mobility is relatively high due to short and organised (hopping) distance among molecules. The hopping site arrangement within a disordered material varies both positionally and energetically. Disorder includes structural disorder (defects) and the presence of chemical inhomogeneties and impurities [69]. These abnormalities introduce trapping sites. These sites are due to presence of water, chemical residues and grain boundaries in semicrystalline materials [70-72]. Relatively low charge carrier mobility in disordered OSs is a consequence of weak intermolecular interactions and resulting localization of charge carriers or trapping by chemical impurities and other trap states formed by structural disorder. Mobility is an important parameter that has been investigated to understand charge transport in OSs. Mobility of an organic material is dependent on its temperature, applied electric field, atmospheric conditions and molecular ordering. Two ways are used to experimentally determine mobility. Most frequently it is determined from the current-voltage characteristics of FET. Recently, however TOF is emerging as a viable method to assess mobility in FET-like structures.

2.2 Time-of-flight method

The charge carrier transport has been studied extensively before in both inorganic and organic semiconductors. TOF is one of the most established experimental techniques for mobility measurements in disordered organic materials. The TOF method is based on the measurement of the carrier transit time (t_{tr}), namely, the time required for a sheet of charge carriers photo-generated near one of the electrodes by pulsed light irradiation to drift across the sample to the other electrode under an applied electric field. Electron-hole pairs are generated by photo-excitation of the film through irradiation with a short pulse laser (the wavelength of which depends on the absorption band of materials). Photo-generated charge carriers will start moving to the other electrode depending on the polarity of the applied bias. The drifting carriers build a current equal to Nev/d ; where N is the number of charge carriers in the material, e is the elementary charge, d is the film thickness and v is the velocity. One of the advantages of using TOF technique is that the hole and electron mobility can be studied separately. The TOF technique was suggested by W. E. Spear in 1957 [73] as a method to study charge carrier transport in low conductivity semiconductors.

The TOF method used for determining mobility of charge carriers through detection of their field-induced transport through a sample start from at one electrode to the arrival at the opposite electrode. This method avoids the intrinsic effects of the microscopic interface environment between the material and electrodes. In addition it also presents itself as a source of information for understanding injection into the semiconductor and determining the trap distribution. This method also avoids high injection based currents in conventional transport measurements.

There are mainly two types of TOF methods

1. Sandwich time-of-flight method (S-TOF), in which the material under investigation is sandwiched between two electrodes, and charge transport occurs in the direction perpendicular to the electrode surface.
2. Coplanar time-of-flight method (C-TOF), in which the material under investigation is deposited between two coplanar electrodes, and charge transport occurs in the direction parallel to the electrode surface.

2.2.1 Sandwich time-of-flight method (S-TOF)

Schematic view of the S-TOF is as shown in Fig. 2.1. In this configuration the semiconducting material is sandwiched between the two electrodes, of which one is transparent (ITO) for exciting photons. A strongly absorbed laser flash creates electron–hole pairs beneath the illuminated electrode. The applied voltage sweeps the appropriate type of carriers through the sample, while the other type of carriers is instantly collected at the illuminated electrode. The wavelength of the incident light corresponds to the maximum absorption of the material. The displacement current of the carriers moving across the sample is measured in the external circuit and allows the determination of the t_{tr} , identified as a sudden drop in the current that corresponds to the carriers reaching the collecting electrode [74-77]. If two electrodes parallel to each other, are kept at a constant separation d and a constant voltage V is applied between them, assume that the electric field, E produced between them is uniform, defined as $E = \frac{V}{d}$, the mobility is then calculated as

$$\mu = \frac{d^2}{vt_{tr}} \tag{2.1}$$

since $v_d = \mu E$ and $v_d = \frac{d}{t_{tr}}$.

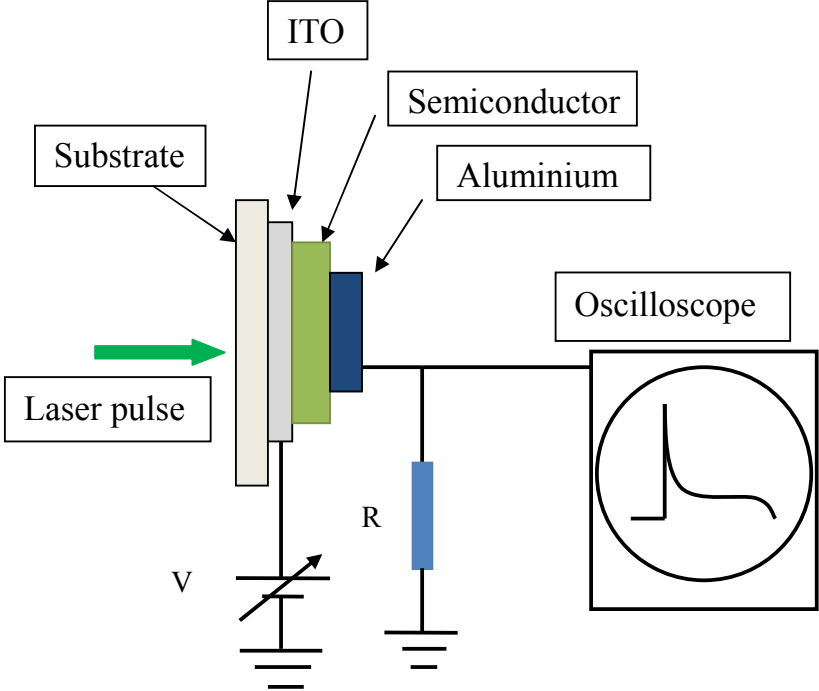


Figure 2.1: Schematic representation of the sandwich time-of-flight method [73].

2.2.2 Coplanar time-of-flight method (C-TOF)

Schematic view of C-TOF is as shown in Fig. 2.2. In this configuration, the semiconducting material under investigation is deposited between two coplanar electrodes, and charge transport occurs in the direction parallel to the electrode surface. In this method, the material is excited with the incident light near the bias electrode and electron-hole pairs (excitons) are created. If a positive voltage is applied to the illuminated electrode, the electrons from dissociating excitons at the electrode/sample interface will rapidly move into the illuminated electrode leaving holes to drift across the sample to the counter electrode where they will discharge.

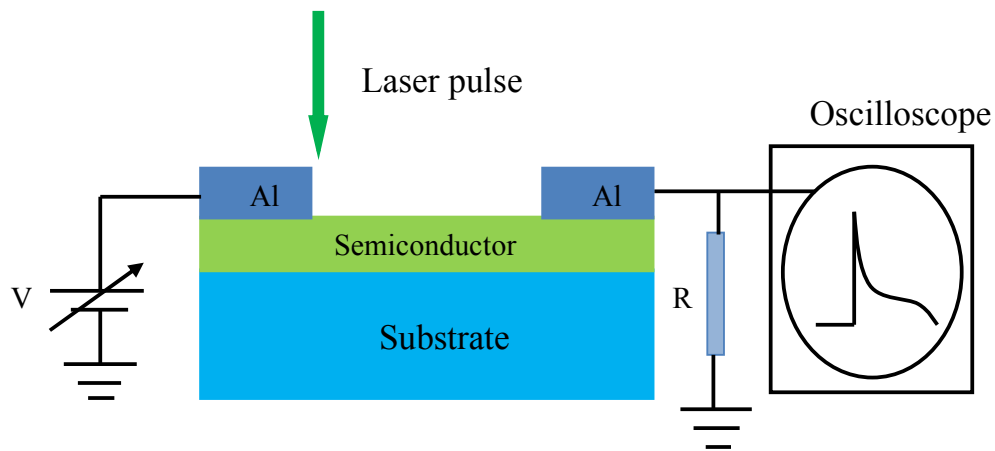


Figure 2.2: Schematic representation of a typical C-TOF circuit [147].

Similarly, if a negative voltage is applied to the illuminated electrode, then the holes will be attracted to the negatively charged electrode while electrons will drift in the opposite direction, enabling us to observe electron transport. The counter electrode is connected to the oscilloscope.

There are important differences of C-TOF compared to S-TOF method as listed below.

1. Charge transport in the S-TOF method is in the bulk of the material. But in the C-TOF method the charge is flowing across the thin film structure.
2. The channel length can be easily varied using a shadow mask or lithography technique. But in S-TOF method the thickness of the sample must be over several tens of microns and a lot of material is required for deposition. It is almost impossible to study the thin film materials especially the graphene-like materials.
3. C-TOF allows us to study structures that are similar or identical to FETs.

2.3 Sample preparation and experimental details of C-TOF

The schematic view of the samples prepared for the C-TOF measurements is as shown in Fig. 2.3. The semiconducting material to be studied is deposited onto the desired substrate and the contacts are deposited on top of it using a shadow mask. In this work we have used fused silica, sapphire, glass and degenerately doped silicon substrates with a thermally grown SiO_2 layer of 300 nm are used as the substrates. These substrates are cleaned with acetone and isopropanol and then blow dry with nitrogen. The OS material to be studied is deposited on to these substrates. Semitransparent aluminum electrodes were deposited via vacuum evaporation at a pressure of 2×10^{-6} mbar using a shadow mask of desired channel length. The evaporation is controlled at a rate of 0.1 nm/s using quartz crystal thickness monitor.

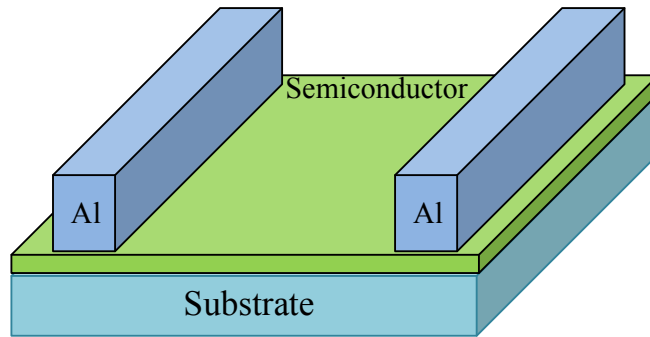


Figure 2.3: Schematic view of the samples prepared for the C-TOF measurements.

The sample is placed on a sample holder and bonded the aluminium electrodes using a bonder machine in order to connect the sample to the amplifier (Miteq) via a Bayonet-Neill-Concelman (BNC) connector. The carrier generation was performed by a Q-switched Nd:YAG laser. The maximum repetition rate is 10 Hz and the pulse width of 3-5 ns. The laser can emit wavelengths from 210 nm to 2300 nm. The laser power was controlled by the neutral density filters. The laser spot is aligned into a straight line using planoconvex lens to a width of approximately 10 μm parallel to the electrode. The illuminated electrode is connected to a DC power supply (Keithley 2400 sourcemeter or Keithley 6487 picoammeter) and the counter electrode is connected to the oscilloscope via BNC connectors. The displacement current of the sample is monitored as a voltage drop across the load resistor using LeCroy oscilloscope having band-pass frequency of 2.5 GHz with a 50 Ω termination. The

resulting photocurrents are displayed as current versus time on a computer connected to the oscilloscope [145-147]. All these electrical measurements were performed in nitrogen filled glove box.

2.4 Determination of transit time: Dispersive and non-dispersive transport

In an ideal case, when an external electric field is applied, the thin sheet of charge created by a laser flash will propagate with a drift velocity v_d , and will reach the opposite electrode in a time t_{tr} after traversing a distance d ,

$$t_{tr} = \frac{d}{v_d} \quad (2.2)$$

But in common practice, the charge sheet encounter defects, recombination centers and trap sites, which would resulting in reduction of effective mobility. Consequently, the charge carriers exhibits a distribution of arrival times and detrapping of the carriers from shallow traps in the curve of time dependence of photocurrent, leads to presence of a long tail after the transit time. In the case where the trap density is low, the majority of charge carriers will drift as a thin sheet of charge. A longer or broader tail corresponds to a greater density of trapping states localized within the bulk [78, 82].

There are two types of photocurrent transients possible known as dispersive and non-dispersive transients.

2.4.1 Non-dispersive charge transport

An ideal case of photocurrent pulse moving across the sample is shown in Fig. 2.4. This is a well defined square pulse of current, which is a characteristic of a narrow sheet of charge travelling across the sample at constant velocity. But the real case may be different from ideal case and it is like as exemplified in Fig. 2.5. The shape of the photocurrent transient contains mainly three parts: (1) initial spike, followed by a (2) constant current plateau or decaying current depending on the type of charge transport and a (3) slowly varying tail. When the incident photons interact the material near the biased electrode electron-hole pairs are created, and they are

separated through the action of an external electric field can participate in conduction and the corresponding initial spike is observed.

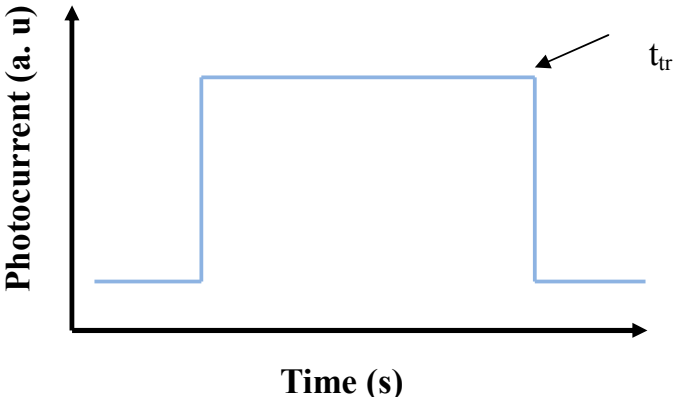


Figure 2.4: Schematic representation of a non-dispersive photocurrent transient under ideal conditions.

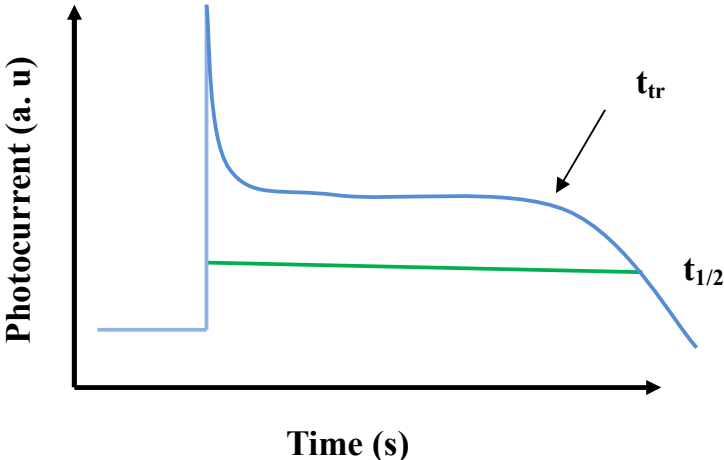


Figure 2.5: Schematic representation of a typical non-dispersive photocurrent transient.

The second stage in a photocurrent is a constant current plateau, where the observed current is due to charge carriers drifting across the sample to the counter electrode. The characteristic feature of the non-dispersive transport is a constant current plateau followed by a long tail. This represents the carriers coherently moving with constant drift velocity with minimal trapping. There is a drop in the photocurrent when the carriers reach the counter electrode. This is the time needed by the fastest carriers to move between the two electrodes. The shoulder region or onset of the tail is frequently chosen as the transit time [78, 82]. The TOF method provides information on trapping and the underlying transport mechanism in addition to the mobility measurements. For example, deviations from the ideal current shape

are expected if the carriers are get trapped. The slight rounding of the signal around t_{tr} is due to dispersion in carrier arrival times. The reason is that the width of the charge sheet can broaden during its transit due to statistical variation of the drift velocity or space charge effects causing mutual repulsion of the carriers within the generation volume. The long tail is due to the trap states, which can hold the charge carriers for certain time. During the transit, charge carriers get trapped and de-trapped in such shallow traps and ultimately reach the other electrode. A large density of shallow traps causes two noticeable effects [78]. One is that they increase the measured time-of-flight, due to the trapping and detrapping of the charge carriers while the second is that the slope of the curve during the recovery time decreases. The transit time is determined from a sharp drop in the photocurrent. This is the time taken for the fastest carriers to cross the sample. The average transit time is defined as the time taken for the current to drop to half of its value at the plateau, denoted as $t_{1/2}$ as shown in Fig. 2.5. From the transit time we can deduce the mobility of the charge carriers as a first approximation from the Eq. 2.1 $\mu = \frac{d^2}{vt_{tr}}$. But the electric field between the coplanar electrodes is not uniform and it is position dependent [147]. Numerical calculations of Laplace equation for two coplanar electrodes demonstrate that the electric field intensity drops rapidly with the distance from the electrode into the channel. This results in relatively low electric field intensity inside the channel. Monte Carlo simulations of time-dependent photocurrent ($I(t)$) in poly(3-hexylthiophene) (P3HT) channels indicate that the use of Eq. 2.1 $\mu = \frac{d^2}{vt_{tr}}$ to estimate the charge carrier mobility may result in values that are almost one order of magnitude lower than the values obtained by assuming a position-dependent electric field:

$$E_x(x) = \frac{2V_{bias}}{\pi d \sqrt{1-(2x/d-1)^2}} \quad 0 < x < d, \quad (2.3)$$

where x is the distance from the biased electrode, and V_{bias} is the potential difference between the two electrodes [147]. The electric field distribution near the bias electrodes scale with t/d ratio, where t is the electrode thickness and d is the separation between the electrodes. In this approach, these equations are numerically calculated. The electric potential U and electric field E in an OS layer on a glass substrate between coplanar electrodes are related by Poisson equation $\nabla(\epsilon \nabla U) = \rho$

and $\vec{E} = -\nabla U$, where the charge density (ρ) in OS is assumed to be zero. Eq. 2.3 is derived using conformal mapping based on the assumption that the charge inside OS layer is zero. The assumption is justified by the negligible charge injection due to blocking contacts and low amount of photogenerated charge [147]. The position-dependent electrical field distribution is a consequence of two coplanar semi-infinite electrode geometry and stems from Shockley-Ramo theorem [214,215]. The diffusion current can be neglected in the drift-diffusion equation, since we assume charge inside OS layer is negligible. The drift current is

$$J = ne\mu E_x(x) \quad (2.4)$$

where J is the current density, n is the charge carrier density, e is the charge of the carrier, μ is the mobility of the charge carriers and $E_x(x)$ is the position-dependent electric field.

2.4.2 Dispersive charge transport

In the case of dispersive charge transport, monotonic decay of photocurrent after the initial spike resembling an exponential decay is observed in contrast to the non-dispersive case, in which a constant plateau is observed. Typical dispersive photocurrent transient on a linear scale is shown in Fig. 2.6. If the carriers are deep-trapped before they transverse the sample the number of free carriers (and thus the current) will decrease monotonically, if detrapping time for these carriers is longer than the transit time and they cannot contribute to the photocurrent. Such a process

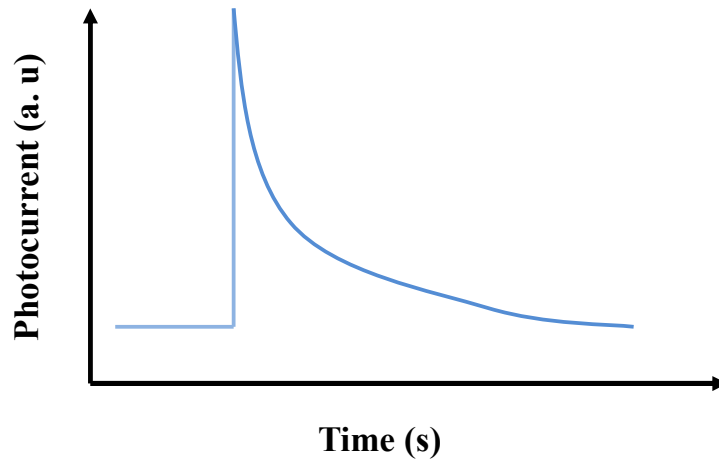


Figure 2.6: Schematic representation of a typical dispersive photocurrent transient on a linear scale.

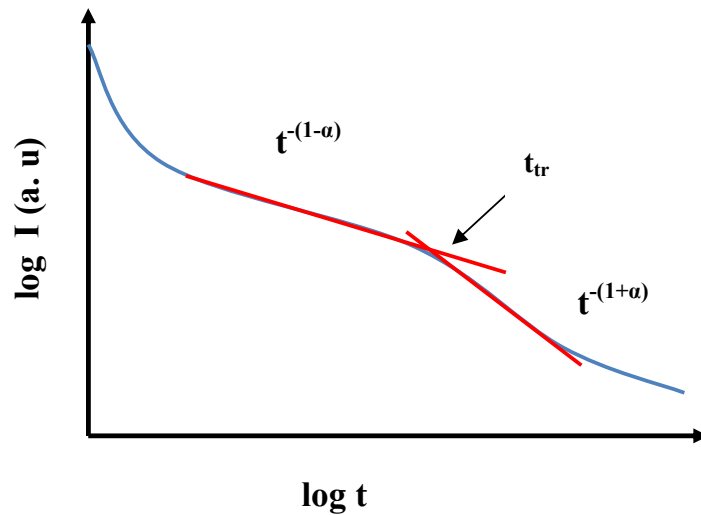


Figure 2.7: Schematic representation of a typical dispersive photocurrent transient on a double logarithmic scale.

would, for instance, occur in a disordered medium [78]. The disorder is due to material inhomogeneities, grain boundaries, and the impurities present in the material. The effect of disorder is the localization of the charge carriers in these materials. The velocity of the carriers gets much more dispersed with a variety of processes, including multiple trapping, dispersion due to material inhomogeneities, which results in a curve with a long tail and a broad knee making the extraction of the transit time more challenging. Such transport is called non-Gaussian or dispersive. In this situation the current signal is usually plotted on a double logarithmic for analysis. The transit time can be determined as the intersection of the two straight lines drawn to the current plateau and a long tail on a double logarithmic scale. Then the current may form two a nearly straight lines of different negative slopes. The intersection of the tangents to these lines clearly defines the transit time as indicated by the arrow in the Fig. 2.7. In non-dispersive transport, the peak of the packet and its mean position are located at the same position and move with the same velocity as shown in Fig. 2.8. In dispersive transport the peak of the position remain fixed at the point of origin of the carriers, while its mean position is moving away from the peak with decreasing velocity as shown in Fig. 2.8.

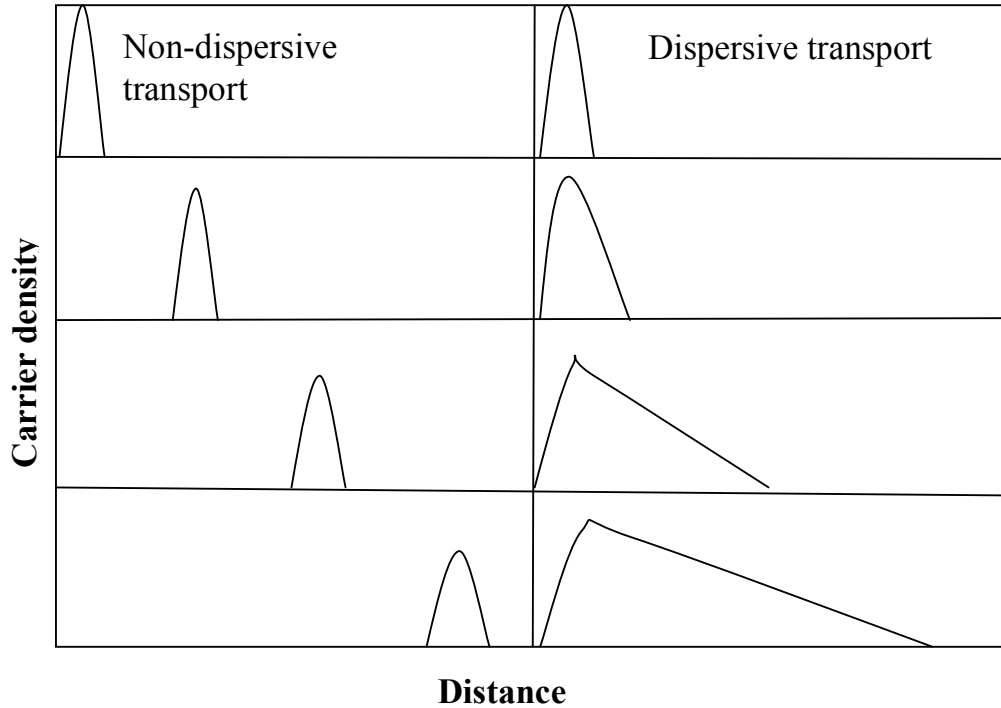


Figure 2.8: Motion of a charge packet across the electrode in case of non-dispersive transport (on the left) and dispersive transport (on the right).

2.5 Scher and Montroll model

Scher and Montroll model has been widely used to explain the behavior of dispersive transport in disordered and amorphous materials. This model links the relation between mobility and disorder and is based on stochastic (statistical) hopping [84, 85]. The charge carriers allowed to spend some time on each hopping site (dwell time) and the probability to leave the hopping site depends on the time spent on the hopping site and it is quantified using the distribution function of time $\psi \sim \exp(-\rho t)$, where ρ is a constant. In a disorder medium the dwell time varies from site to site and it is a random variable. It appears in the form of a long tail in the photocurrent after the transit time or a featureless decay. Scher and Montroll have proposed a dwell time probability distribution [86,89] to describe the effect of disorder using a time-dependent random walk of carriers on a grid of sites

characterized by a dwell time distribution, $\Psi(t)$

$$\psi(t) \propto t^{-(1+\alpha)} \quad (2.5)$$

where α is a disorder parameter and has a value from 0 to 1. Its value is 1 for crystalline material and less than 1 for disordered material. The mean position of a carrier in the packet at time t is given by

$$\langle l \rangle \propto l t^\alpha \quad (2.6)$$

where l is the mean displacement of the charge carrier.

The current which is proportional to the velocity of the charge carrier

$$I(t) \propto \frac{d\langle l \rangle}{dt} \quad (2.7)$$

The Scher-Montroll model has shown that for $t \ll t_{tr}$,

$$I(t) \propto t^{-(1-\alpha)} \quad (2.8)$$

and for $t \gg t_{tr}$,

$$I(t) \propto t^{-(1+\alpha)} \quad (2.9)$$

and the sum of the slopes at times $t \ll t_{tr}$ and $t \gg t_{tr}$, would be $[-(1-\alpha)-(1+\alpha)] = -2$.

The Scher-Montroll model, however, fails to rationalize the field-dependence of mobility and the occurrence of non-dispersive current traces.

2.6 Bässler's Gaussian disorder model

Another model proposed by Bässler and coworkers to describe the dispersive charge transport is the so called Gaussian disorder model [89]. This model assumes that the transport of charge by hopping among random localized sites whose energies are Gaussian distributed.

$$g(\varepsilon) = \frac{1}{\sqrt{2\pi\sigma^2}} \exp\left(-\frac{\varepsilon^2}{2\sigma^2}\right) \quad (2.10)$$

The energy ε is measured relative to the center of the density of states and σ describes the Gaussian width. The transport sites are subjected to diagonal disorder (σ) and off-diagonal disorder (Σ). The origin of the diagonal disorder is the fluctuation of the molecular energy levels and the origin of off-diagonal disorder is the fluctuations in the intermolecular distance and the mutual orientation of the two molecules. The jump rate from the site i to j , v_{ij} is described by the Miller-Abrahams' formula,

$$v_{ij} = v_0 \exp\left(\Gamma_{ij} \frac{\Delta R_{ij}}{a}\right) \exp\left(-\frac{\varepsilon_j - \varepsilon_i - eEr}{kT}\right) \text{ for } \varepsilon_i > \varepsilon_j \quad (2.11)$$

$$v_{ij} = v_0 \exp\left(\Gamma_{ij} \frac{\Delta R_{ij}}{a}\right) \text{ for } \varepsilon_i > \varepsilon_j. \quad (2.12)$$

where a is the lattice parameter v_0 correspond to an electronic wavefunction overlap factor, Γ_{ij} is the wavefunction overlap parameter, ε_i and ε_j are site energies and eEr is the electrostatic energy in the presence of an electric field, k is the Boltzmann's constant and T is the temperature. The probability for an upward jump is an exponential function of energy and downward jump does not need any activation energy and also is not accelerated by the electric field.

Bässler's Monte Carlo simulations based on this model show that the mobility increases with increasing Σ at constant electric field. But the lateral electric field in organic devices along the transport axis is not homogeneous. The density of accumulated charge carriers within the grain boundary is not uniformly distributed. Due to the applied lateral electric field, carrier concentration increases on one side within the grain, whereas on the other side carrier concentration reduces. This creates an internal lateral electric field which will compensate the external applied electric field. Consequently, the electric field within the grain is screened and the electric field between the grain boundaries is enhanced. Hence the electric field in polycrystalline films is dominated by the peaks at the grain boundaries along the transport axis [174]. The superimposing of off-diagonal disorder on the array of energetically ordered hopping sites ($\sigma=0$) increases the carrier diffusivity, and hence the mobility. The role of the off diagonal disorder is opposite to the diagonal disorder. The increase of the diagonal disorder not only causes a decrease of mobility but also makes the TOF signal dispersive due to dispersion in hopping times. The degree of dispersion depends on the degree of disorder. At low levels of disorder the TOF signal may be non-dispersive. The presence of the long tail of the non-dispersive TOF signal is the result of the non-thermal field-assisted spreading of the drifting carrier packet due to disorder.

This model successfully explains the connection between the features of the transient photocurrents and field and temperature dependence of the charge carrier mobility.

2.7 Conditions to be met for TOF measurements

If an arrival time is to be observed, there are essential requirements that must be met.

1. The laser photoexcitation pulse duration should be substantially smaller than the transit time to make sure that no transit occurs during the pulse duration.
2. The energy of the light pulse should be such that the total photogenerated charge is much smaller than the product of the applied voltage and the capacitance sample. Otherwise the features of the transient photocurrent will be distorted by the space charge [90, 93].

The shape of the sheet of charge carriers can be broadened as a result of the mutual repulsion and gives an error in the transit time Δt ,

$$\frac{\Delta t}{t_{tr}} \approx \frac{q}{CV}$$

3. The circuit response time must be less than the transit time ($RC \ll t_{tr}$) [94, 95].
4. The dielectric relaxation time must be larger than the transit time. Otherwise the photoexcited charge carriers will be screened by the majority carriers within the relaxation time.
5. One must be the blocking electrode in order to avoid large dark currents which can change the electric field, with the creation of a space charge in the OS.
6. The recombination time must be larger than the transit time [96].

2.7.1 Metal/organic semiconductor interface and blocking contacts

The interface between the metal and OS plays an important role in the performance of OFETs. The schematic energy level diagram of metal/OS is as shown in Fig. 2.9. The work function of the metal should match with the highest occupied molecular orbital (HOMO) of an OS for the injection of holes. The mismatching of the energy levels leads to poor injection of holes. In a similar way, the work function of the metal should match with the lowest unoccupied molecular orbital (LUMO) of an OS for injection of electrons [47]. But for TOF measurements, the electrodes should be non-injecting and hence create a blocking contact between the metal electrode and the sample to avoid large dark currents and the creation of a space charge. The space charge created inside the OS, creates some electric field. The electric field due to space charge changes the applied electric field distribution. For

this purpose, we have to choose the non-injecting contacts. e.g: for P3HT, which is a p-type semiconductor and it has HOMO at -5.1 eV [175], the work function of the metal was chosen as aluminum, which has a work function of 4.3 eV [201], hence the difference between the HOMO and metal contact is around 0.8 eV, such that it leads to poor injection of holes into P3HT [207,208,210].

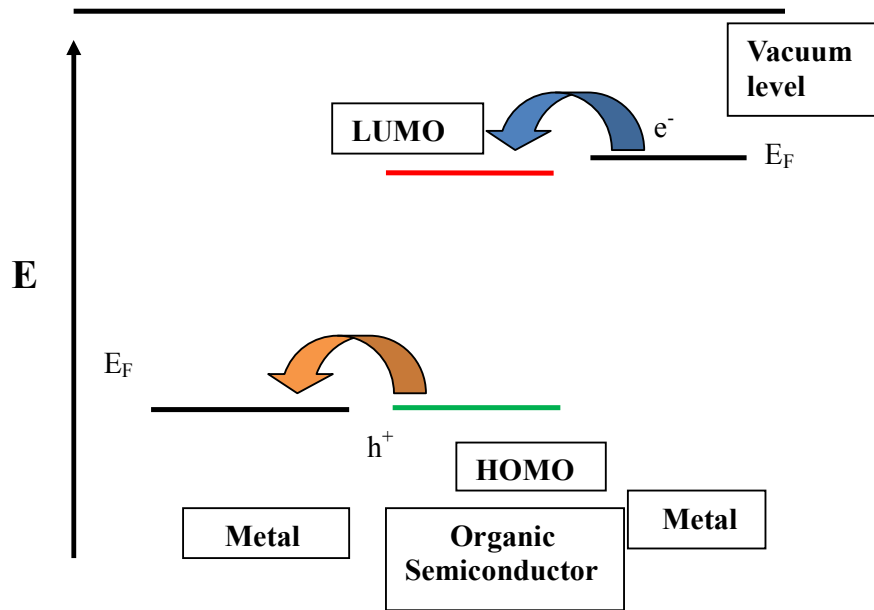


Figure 2.9: Schematic energy level diagram of metal/organic semiconductor [47,207].

2.8 Field-effect transistor characterization

The mobility extracted from the transconductance curve of an OFET operating in the linear or saturation region is termed as the field effect mobility. Study of OFETs yields the information about the transport phenomena of accumulated charge layer in the OS thin film. In addition to that it provides the information about the semiconductor type, mobility, threshold voltage and the charge trapping. Unlike traditional silicon and other doped inorganic semiconductors which can operate in both the inversion and accumulation modes, OFETs typically operate in the accumulation mode due to the difficulty to impose a stable controlled level of doping and lack of ambipolar transport. The accumulation of charge carriers at the

semiconductor dielectric interface forms a low resistance pathway or a channel for carriers to move. The concentration of carriers can be modulated using the voltage applied to the gate. Therefore a voltage differential between the source and the drain electrodes result in conduction of carriers through the channel. The current through the channel depend on the gate, source and drain biases, the mobility of the material, the geometry and a few other parameters like the injection at the metal semiconductor contacts, the morphology of the semiconductor. Schematic view of the electrical characterization of a FET is shown in Fig. 2.7

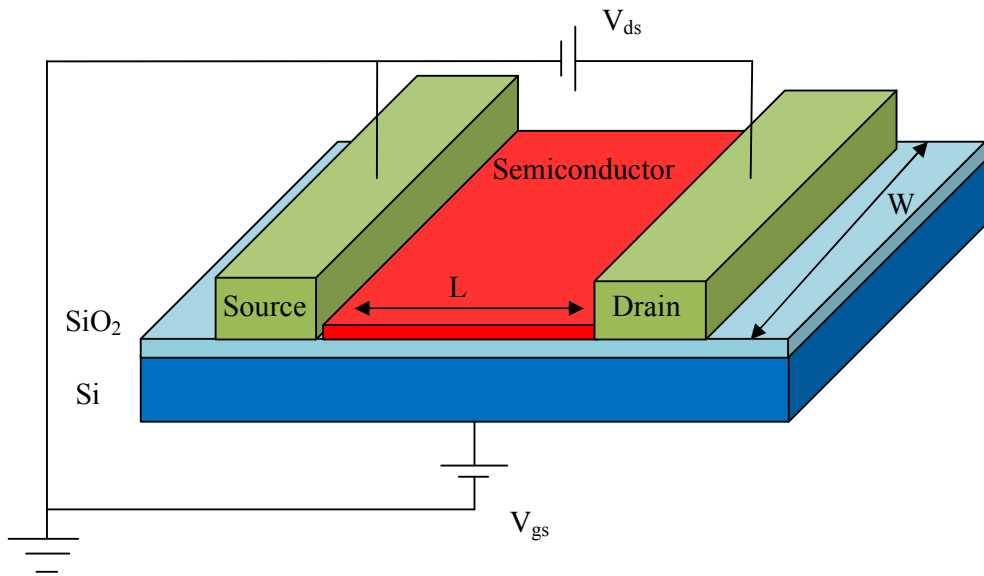


Figure 2.7: Schematic representation of the electrical characterization of the field-effect transistor.

In this work degenerately doped silicon substrates with a thermally grown SiO₂ layer of 300 nm or 230 nm thickness were used as the substrates and also as the gate electrode. Gate electrode is used to capacitively accumulated charge carriers in OS. The charge transport occurs between drain and source electrodes. All electrical measurements made in this work employed two electrodes for drain and source contacts. In bottom-contact structure, electrodes are deposited prior to the deposition of the OS by using shadow mask or optical lithography. In top-contact structure, the gold electrodes are deposited by electron beam deposition or vacuum evaporation after the deposition of OS using a shadow mask under vacuum at a base pressure of

10^{-6} mbar. The fabricated FETs were characterized using back gated configuration. All these electrical measurements were measured in a nitrogen filled glove box. Electrical measurements were measured in a probe station connected to a setup consists of the following instruments.

1. A voltage source (Keithley 2400) that supplies the drain-source bias V_{ds} .
2. For gated measurements an additional Keithley 6487 picoammeter is employed to apply a gate-source voltage V_{gs} and is equipped with the capability to monitor the leakage current (I_g) through the back-gate.

Device characterization was done depending on experimental requirements. Typically, a fabricated graphene device is tested for its I–V characteristics first by acquiring I_{ds} as a response to varying V_{ds} keeping different gate voltages constant. Transfer characteristics were measured keeping V_{ds} constant and sweeping gate voltage V_{gs} .

The net charge carrier density in graphene can be calculated from the transfer characteristics from the following formula

$$p - n = \frac{\epsilon(V_g - V_T)}{et_{ox}}, \quad (2.13)$$

where p and n are the hole and electron density, ϵ is the dielectric constant of the gate dielectric, V_T is the required gate voltage to obtain the charge neutrality, t_{ox} is the thickness of the gate dielectric [3].

Neglecting the contact resistance, the two dimensional normalized conductivity can be calculated by Drude's formula

$$\sigma = \frac{(I_{ds}/W)}{(V_{ds}/L)}, \quad (2.14)$$

where I_{ds} is the drain source current, V_{ds} is the drain source voltage, W is the width of the channel, L is the channel length.

The field effect mobility of the devices can be found from the formulae

In the linear regime ($V_{ds} < (V_{gs} - V_{th})$),

$$I_{ds} = \mu C_{ox} \frac{W}{L} ((V_{gs} - V_{th})V_{ds} - \frac{V_{ds}^2}{2}), \quad (2.15)$$

In the saturation regime ($V_{ds} > (V_{gs} - V_{th})$),

$$I_{ds} = \mu C_{ox} \frac{W}{2L} (V_{gs} - V_{th})^2 \quad (2.16)$$

μ is the mobility and C_{ox} is the gate capacitance per unit area [97].

The saturation region mobility is usually higher than the linear region mobility for an organic transistor. This is a result of the non-ideal injection of charge carriers into the

semiconductor through the metal contacts. Therefore to accurately measure the FET mobility it is necessary to have a good ohmic source and drain contact. But in C-TOF, we create the charge carriers inside the channel, thus we can avoid the effect of contacts, which include poor injection due to mismatching of energy levels, contact resistance and high injection based currents. In OFETs, the accumulated charge is at the interface between the dielectric/OS, and the charge carrier mobility is affected by the surface states, traps and impurities present on the dielectric surface. But in C-TOF the charge carriers are created on the surface of OS, hence the charge carrier transport is not affected by the dielectric/OS interface.

2.9 Atomic force microscope (AFM)

Binnig, Quate and Gerber invented the atomic force microscope (AFM) in 1985 [98]. It produces topographical images of the sample surface. AFM is a combination of the principles of STM and the stylus profilometer.

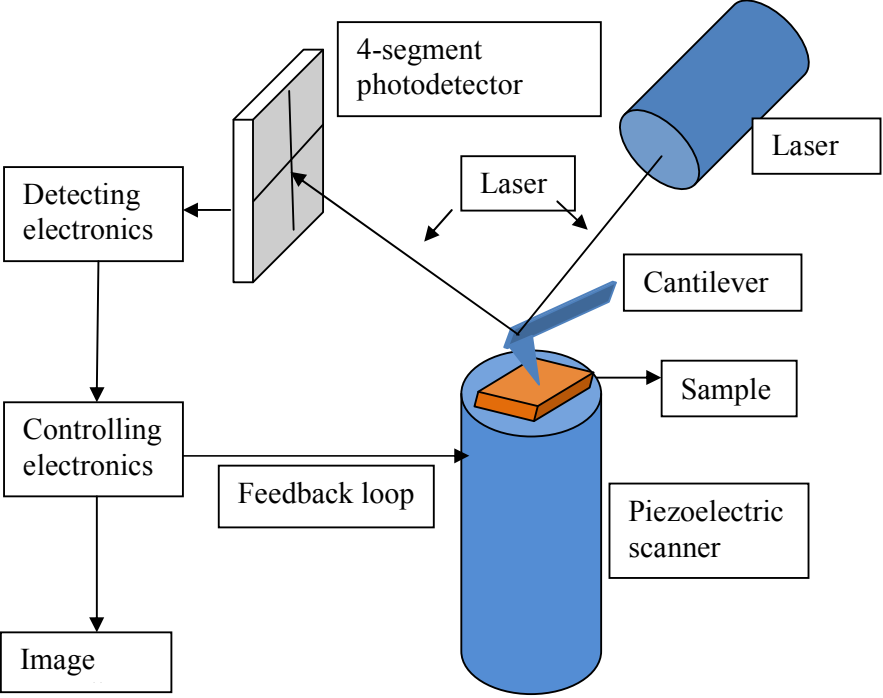


Figure 2.8: Schematic diagram of the atomic force microscope. The tip is at a fixed position and the sample is moved by the scanner [102].

Schematic diagram of the atomic force microscope is shown in Fig. 2.8. When the cantilever is in close proximity (nanometer separation) it experiences surface forces. In constant force mode, a feedback mechanism adjusts the cantilever-sample distance so the average force on the tip is constant and the variation in cantilever sample distance that ensues is recorded. Software is employed to produce topographical images from this data. Piezoelectric transducers are necessary for the movement of the cantilever system in the Z-direction which requires a feedback loop. Piezoelectric transducers are also incorporated into the mechanical design of an AFM to allow movement of the sample with respect to the tip in the X-Y plane. In constant height mode, the tip is at constant mode and the scanner of the microscope maintains fixed end of cantilever on the constant height value. So deflection of the cantilever under scanning reflects topography of sample under investigation.

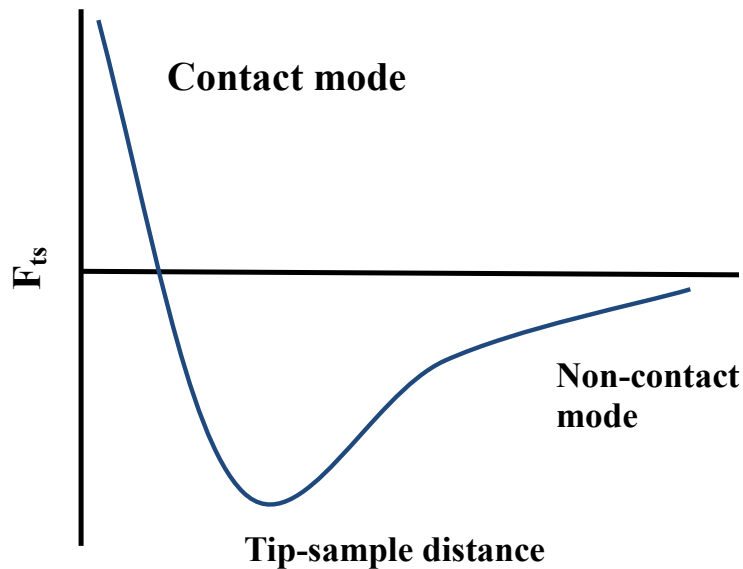


Figure 2.9: The force between the tip and sample F_{ts} as a function of the distance between the tip and sample surface [102].

The force between the tip and sample F_{ts} , as a function of the distance between the tip and sample surface is shown in Fig. 2.9. The contact mode is operated in the repulsive force regime and non-contact mode is operated in the attractive force regime. There are several AFM operational modes and for the highest quality images the mode selected typically depends on the surface being studied. There are both

attractive and repulsive contributions of the force experienced by the AFM tip and the AFM scanning parameters can be modified to image the surface primarily with attractive force contributions or repulsive force contributions to improve imaging [102]. AFM yields information about the surface morphology by operating in one of the three modes.

1. Contact mode
2. Non-contact mode
3. Tapping mode.

1. Contact mode: AFM was originally only operated in contact mode, where the cantilever is in physical contact with the surface, whilst it is scanned across the surface and the static deflection of the cantilever is recorded. However, as the tip of the cantilever scans the surface whilst in direct contact with the atoms of that surface, damage to the surface can result. In contact mode the interaction is dominated by relatively short-range repulsive interatomic forces.

2. Non-contact mode: Under ambient conditions, the sample surface is covered by a thin water layer leading to a meniscus forces. Non-contact mode AFM does not suffer from tip or sample degradation effects that are sometimes observed after taking numerous scans with contact AFM. This makes non-contact AFM preferable to contact AFM for measuring soft samples. This mode was used for all AFM investigations in this thesis work, in order to avoid tip-induced artifacts on organic molecules.

3. Tapping mode: In tapping mode, the cantilever is driven to oscillate up and down at near its resonance frequency by a small piezoelectric element mounted in the AFM tip holder similar to non-contact mode. Most of the state-of-the-art AFMs operate in this mode to characterize organic semiconductors and similar mechanically sensitive materials.

Chapter 3: TOF measurements on reduced graphene oxide and effect of adsorbates

In this chapter we present the TOF photocurrent measurements of reduced graphene oxide (rGO) on different substrates and the effect of adsorbates using the TOF technique. The first part of this chapter consists of TOF measurements on rGO on fused silica, sapphire and Si/SiO₂ substrates. The second part of the chapter includes the sensitivity of TOF measurements on rGO with the addition of adsorbates on its surface. This includes both electron acceptor and electron donor.

3.1 TOF measurements on rGO on fused silica, sapphire and Si/SiO₂

GO was prepared by the Hummer's method [148] and 3 nm of GO layer was deposited on fused silica, sapphire and Si/SiO₂ substrates and then reduced to graphene in an ultrahigh vacuum chamber by annealing at 700 °C. The thickness of the rGO sheets measured from the AFM images is 0.5±0.2 nm. However due to the overlap of rGO sheets, thickness of these layers varies in some regions 1±0.1nm, 1.5±0.1 nm. Aluminum electrodes were deposited on rGO using a shadow mask in a vacuum chamber at a pressure of 2×10⁻⁶ mbar. The channel lengths used in these measurements were 2500 μm, 2000 μm and 800 μm.

The maximum absorption of rGO is at 200 nm wavelength in the UV-visible region [103]. The measured UV-visible absorption spectrum of rGO on fused silica and bare fused silica substrate is shown in Fig. 3.1. The maximum absorption is at 200 nm wavelength and drops towards the visible region. The excitation source was pulsed Nd:YAG laser of wavelength 210 nm with pulse duration of 3 ns. The bias voltages applied to the samples were varied from -200 V to +200 V with a step of 50 V depending on the sample conductivity and channel length described in the following. The displacement of the charge carriers in the graphene channel was recorded with a 2.5 GHz (LeCroy) oscilloscope with a 50 Ω termination. To detect very small currents corresponding to low electric fields, an amplifier (Miteq AM-

1309) was used.

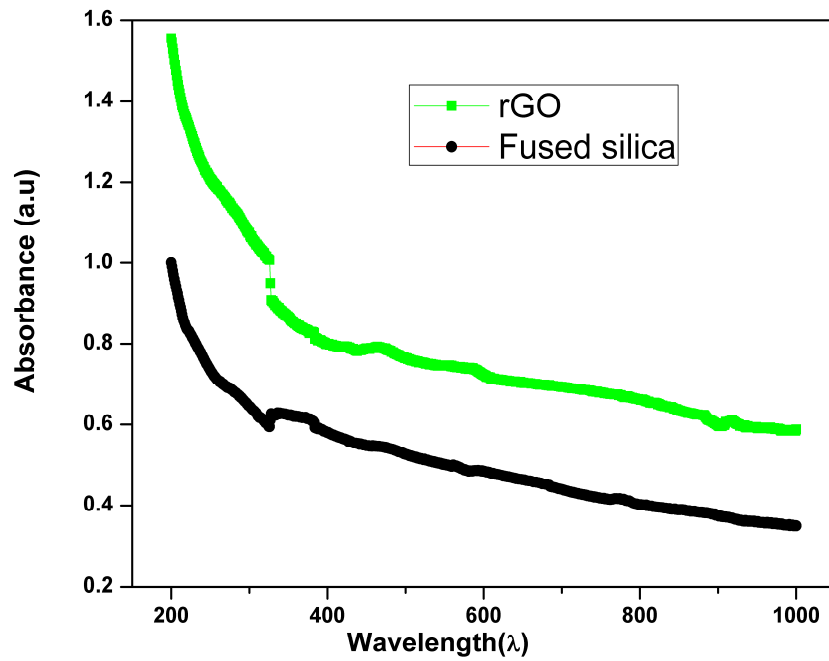


Figure 3.1 UV-visible absorption spectrum of reduced graphene oxide on fused silica and bare fused silica substrate.

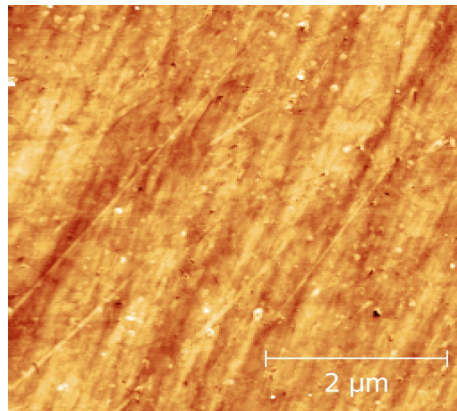


Figure 3.2: 5μm×5μm AFM image of rGO on fused silica. The height scale is 0 to 10 nm.

AFM image of topography of rGO on fused silica is shown in Fig. 3.2. The fused silica substrates are polished to reduce the roughness of the surface and root-mean-square (RMS) roughness of the surface is 0.18 nm prior to deposition of the rGO layer and it is increases to 0.72 nm after the deposition. The rGO layer has the good continuity due to the planar nature of GO sheets as well as the stacking of GO layers. The thickness of the layer is reduced to approximately 0.5 ± 0.2 nm after

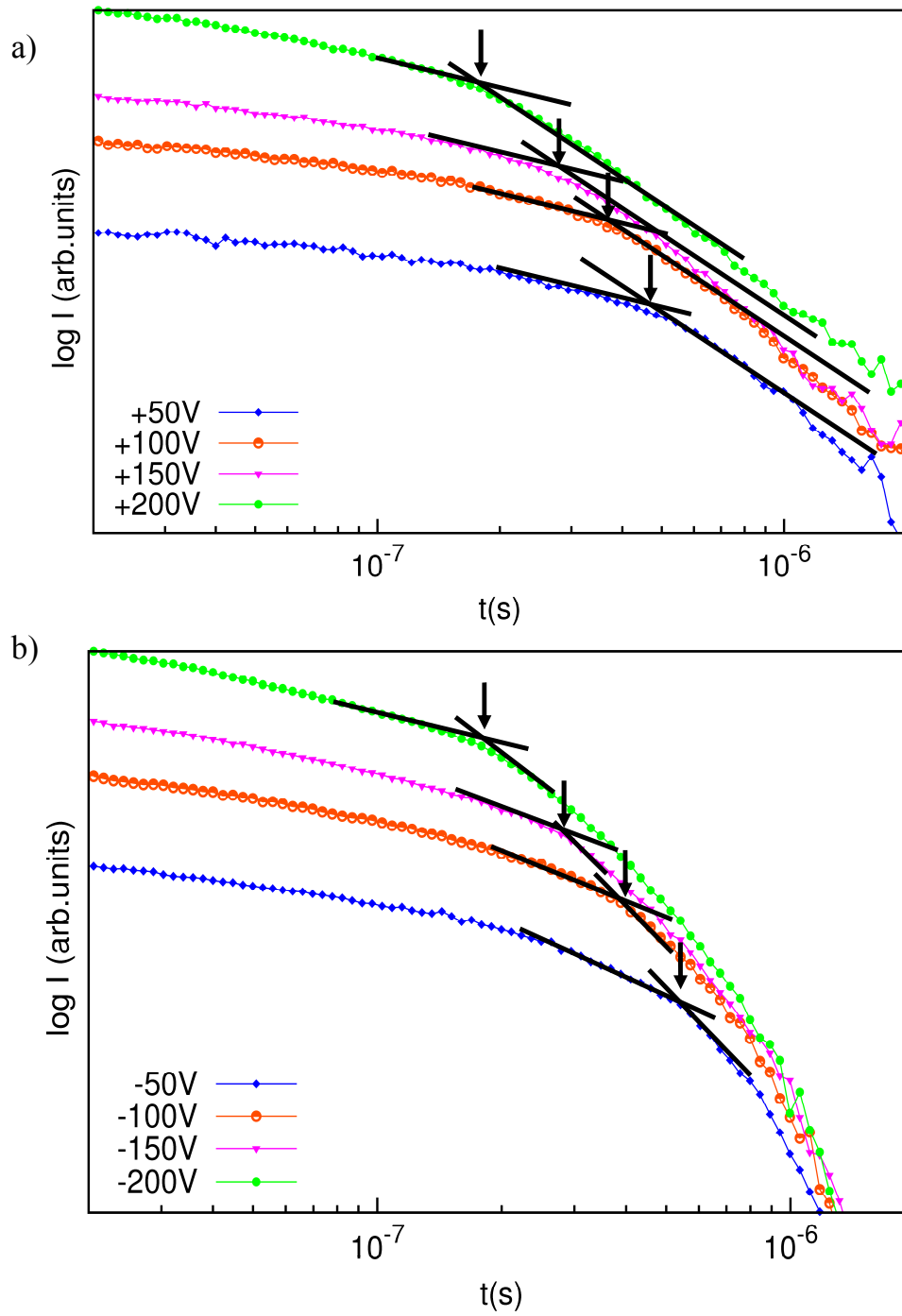


Figure 3.3: Double logarithmic plot of TOF photocurrent measurements on rGO deposited on fused silica substrate with a channel length of 2000 μm for (a) positive and (b) negative bias. The curves are shifted vertically for clarity.

annealing due to the removal of oxygen-containing groups from both surfaces and small pits are formed on the surface. TOF measurements were performed on rGO on fused silica substrates and the results are presented in Fig. 3.3 for both polarities of the applied bias. For positive bias (Fig. 3.3a)), when the carriers that are generated near the biased electrode by a laser pulse the electrons drift to the illuminated electrode and contribute only a fraction of current to the $I(t)$ curve. Holes starts to drift to the opposite electrode due to the applied electric field, and drop in the current will appear when the fastest holes reach the opposite electrode. In a similar way, when the negative bias is applied (Fig. 3.3b)), holes were immediately collected at the bias electrode, and electrons will drift towards the opposite electrode. The transit time is determined from the intersection of the asymptotes drawn to the plateau and to the long tail for different applied bias as shown in Fig. 3.3. The transit time decreases with increasing the applied voltage and its variation is as shown in Fig. 3.4. We observed that the transit time is relatively shorter for holes than electrons.

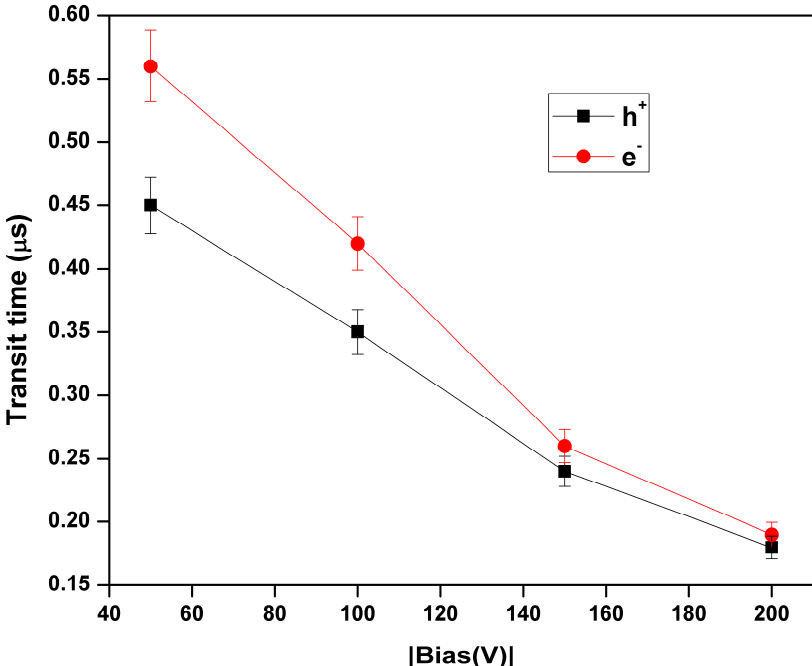


Figure 3.4: Variation of transit time as a function of applied bias for electrons and holes. The extracted mobility is 1200-1600 cm^2/Vs .

These rGO layers exhibit the ambipolar carrier transport and holes are moving slightly faster than electrons. Due to unintentional doping from the substrate,

presence of residual oxygen-containing groups and exposure to the humidity the rGO layers exhibit p-type behavior, and these impurities can trap electrons, hence the electron mobility is slightly lower than hole mobility [123, 115, 149, 150].

AFM image of topography of rGO on sapphire substrate is shown in Fig. 3.5. The RMS roughness of the layer is 0.58 nm. The rGO layer on sapphire substrate shows well connected regions of graphene with wrinkles and folds. The presence of folds and wrinkles leads to diffusive transport of charge carriers along and across them and tunneling across the collapsed region. This affects the charge transport and contributes to the significant resistance to the device [209]. Al electrodes are deposited onto rGO on sapphire substrate using a shadow mask having channel length of 2000 μm and TOF measurements were performed and the results are presented in Fig. 3.6.

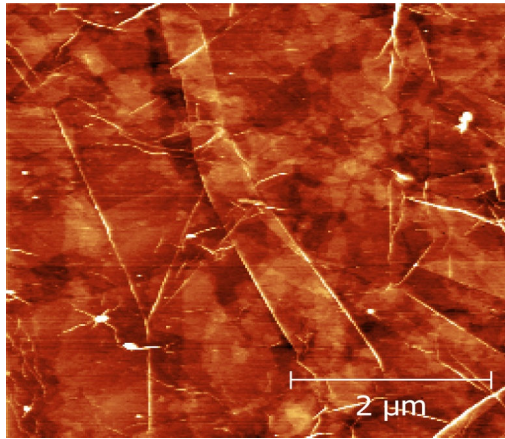


Figure 3.5: $5\mu\text{m}\times 5\mu\text{m}$ AFM image of rGO on sapphire substrate. The height scale is 0 to 4 nm.

The transit time is measured from the intersection of the asymptotes drawn to the constant plateau and to the long tail. The transit time decreases with increasing of applied voltage and its trend for both electrons and holes is shown in Fig. 3.7. These rGO layers exhibit the ambipolar carrier transport and the transit time is nearly the same for both electrons and holes. Comparing the behavior of rGO layers on fused silica and sapphire, the transit time is slightly higher for the rGO layers on sapphire substrate, which implies relatively low mobility on these substrates. The $I(t)$ curves on sapphire, the TOF curves on sapphire shows continuously decreasing photocurrent, whereas on fused silica substrates, photocurrent is constant for a period of time, and suddenly drops when the carriers reach the opposite electrode. But in case of rGO on sapphire after the initial spike, the photocurrent starts to decrease

continuously until the carriers reach the opposite electrode. This behavior can be understood from the morphological differences of rGO on fused silica and sapphire substrates. rGO on sapphire contains folds and ripples, which are known to be electrically active and can trap charge carriers [198]. When graphene is bent or folded, the electron cloud on its surface is also distorted, hindering charge carrier transport through them [209].

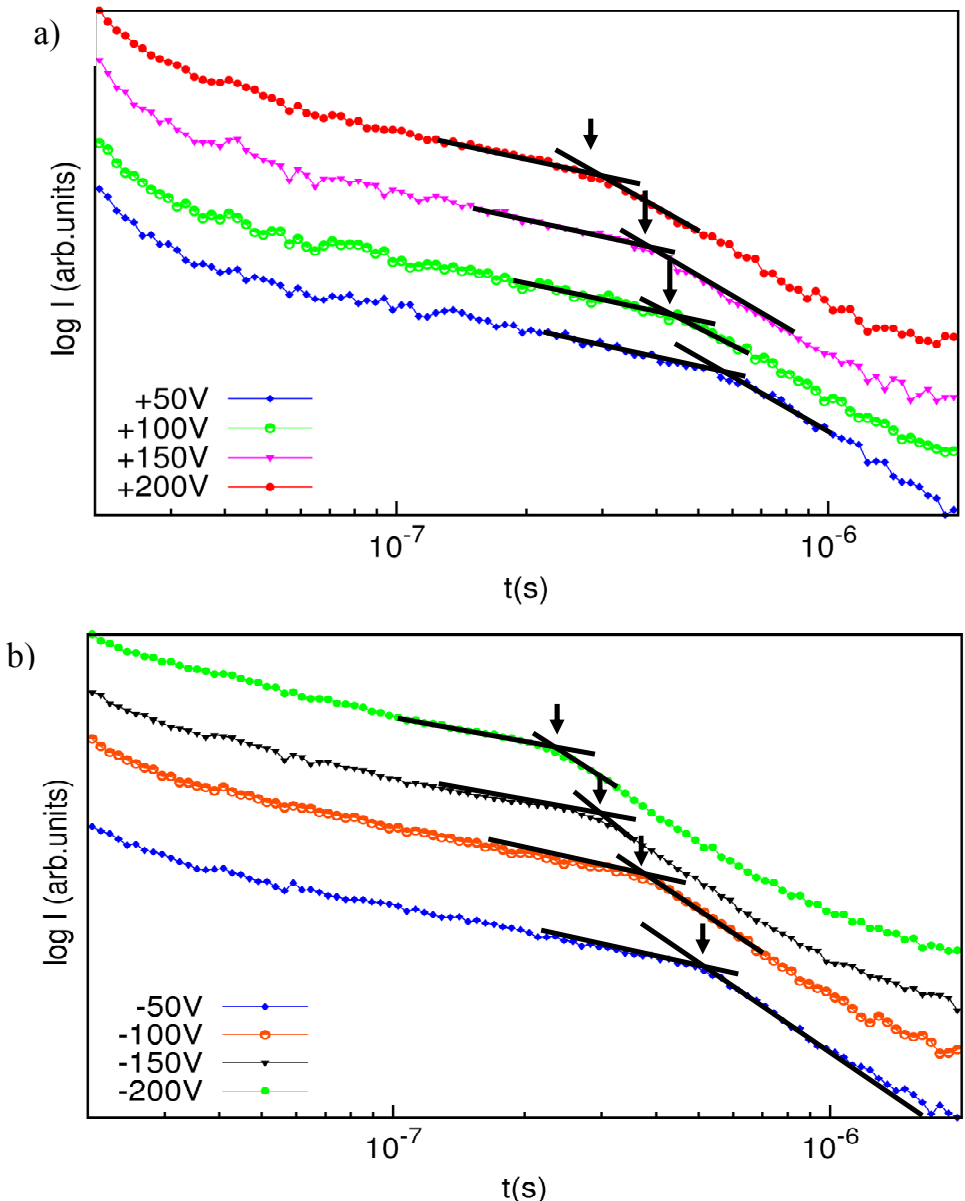


Figure 3.6: Double logarithmic plot of TOF photocurrent measurements on rGO deposited on sapphire substrate with a channel length of 2000 μm for (a) positive and (b) negative bias. The curves are shifted vertically for clarity.

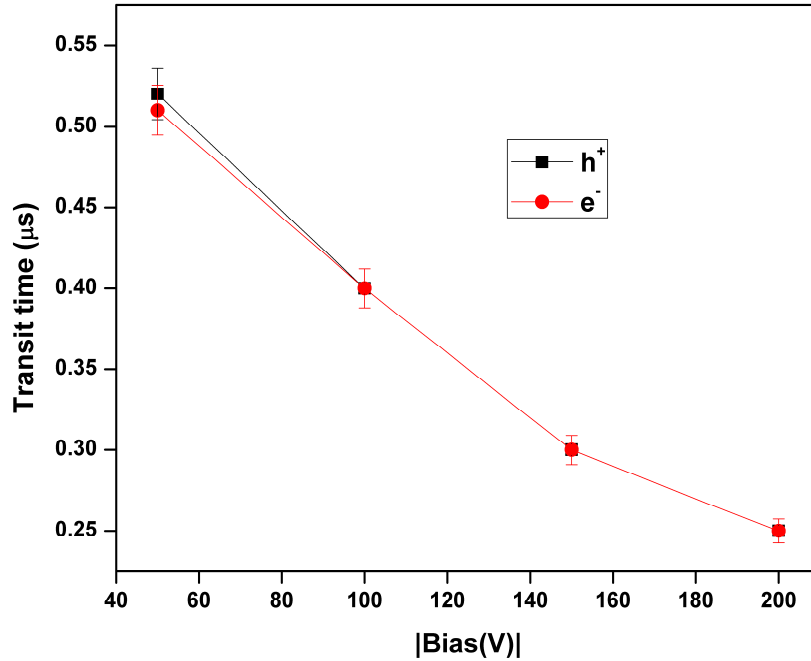


Figure 3.7: Variation of transit time as a function of applied bias for electrons and holes. The extracted mobility is 800-1600 cm²/Vs.

AFM image of topography of rGO on Si/SiO₂ substrate is shown in Fig. 3.8. The sheets are micrometer size graphene domains. Previous reports indicate that the structure of these sheets is described by intact nanometer-sized graphitic domains separated by defect clusters, which results in hopping conduction as the possible charge-transport mechanism [199]. We can observe that the graphene flakes are not well connected, and they are randomly oriented.

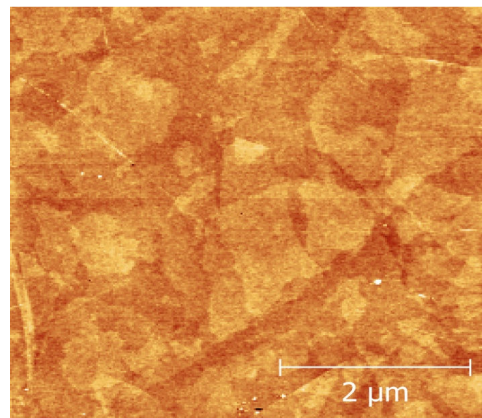


Figure 3.8: 5μm×5μm AFM image of rGO on Si/SiO₂ substrate. The height scale is 0 to 4 nm.

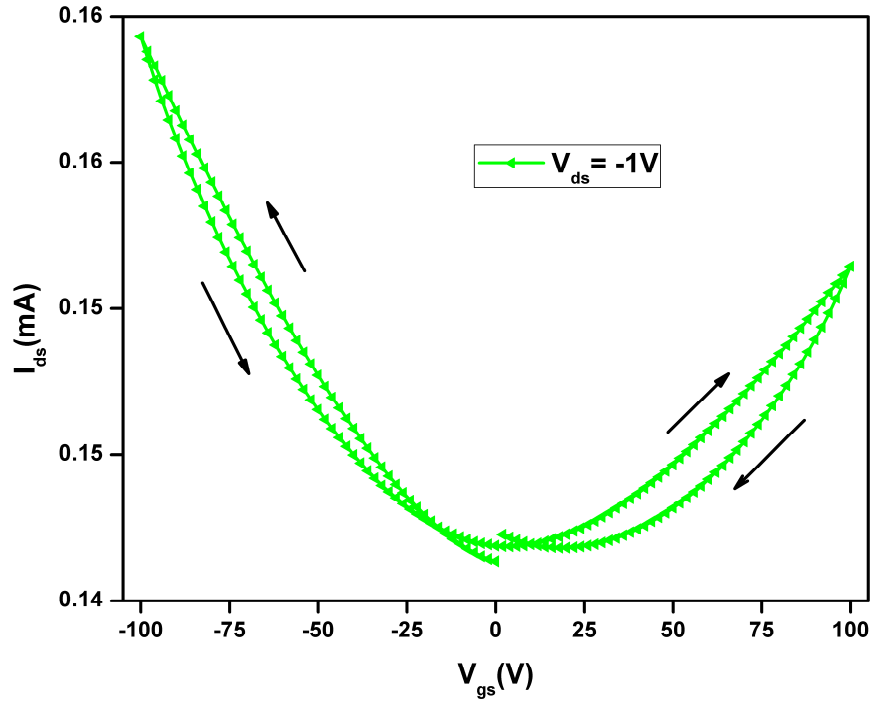


Figure 3.9: Transfer characteristics of rGO-based FET having channel length $L=150 \mu\text{m}$ and width $W=0.5 \text{ cm}$.

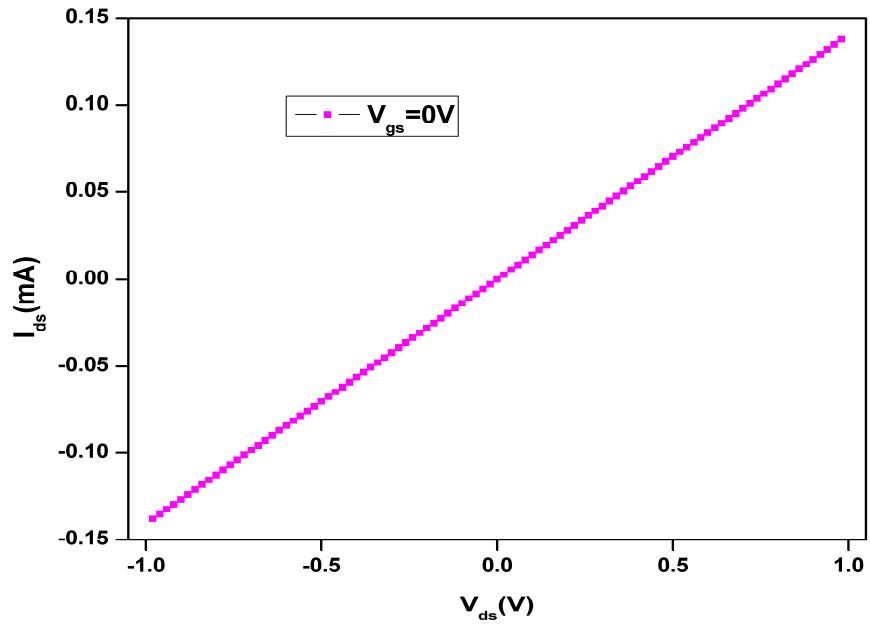


Figure 3.10: I-V characteristics of rGO-based FET at zero gate voltage having channel length $L=150 \mu\text{m}$ and width $W=0.5 \text{ cm}$.

Gold electrodes were deposited on top of it by electron beam evaporation

using a shadow mask. The channel length of the device was 150 μm and width was 0.5 cm. The resulting FETs were tested and the transfer characteristic and an I-V characteristic are presented in Figs. 3.9 and 3.10 respectively. The voltage sweep starts from 0 to -100 V and then to +100 V and then back to 0 V at constant $V_{\text{ds}}=-1$ V at a rate of 4 V/s. These rGO-based FETs are showing ambipolar behavior but poor $I_{\text{on}}/I_{\text{off}}$ ratio (1.14) and the estimated mobilities are 0.7 cm^2/Vs for holes and 0.4 cm^2/Vs for electrons. The broad Dirac minimum is a result of disorder present in rGO layer [149]. The gate voltage corresponding to the minimum conductivity of the $I_{\text{ds}}-V_{\text{gs}}$ curve is called Dirac voltage (V_{Dirac}) or charge neutrality point. In addition, strong hysteresis was observed upon sweeping V_{gs} and is related to the charge transfer across the interface between the rGO layer and SiO_2 [104,123].

The Al electrodes were deposited (to reduce the dark current which will disturb the internal electric field) onto rGO on the same substrates using a shadow mask of 800 μm . For TOF measurements we have fabricated field-effect structures comprising rGO as active material in the channel. TOF measurements were performed on these samples with 1 k Ω termination and the results are presented in Fig. 3.11 for both positive and negative polarity. We have performed these experiments with lower voltages, because higher voltages cause breakdown of the gate dielectric. Since the photocurrent is low at lower voltages, we have used 1 k Ω termination. Transit time is determined from the intersection of the asymptotes drawn on the photocurrent transient as shown in Fig. 3.11. No transit time was determined at low voltages, since the photocurrent is low, and signal/noise ratio is poor. The estimated mobility for holes 3.2 cm^2/Vs and 2.1 cm^2/Vs using Eq. 2.1, assuming the uniform electric field between the electrodes. This value is in close with the measured value on FETs, which is about 1 cm^2/Vs . The conductivity and carrier mobility were found to lag behind those of exfoliated graphene by three orders of magnitude [3]. We have performed the experiments on fused silica and Si/SiO₂ substrates without any active material in the channel, in order to check the influence of charge carriers that are generated from silicon. No appreciable influence was detected from charge carriers from silicon. The 2D conductivity of these layers is around 0.5 μS . The conductivity of rGO on Si/SiO₂ is 0.5 μS which is considerably less than the conductivity of rGO layers on fused silica and sapphire substrates, which is about 32 μS .

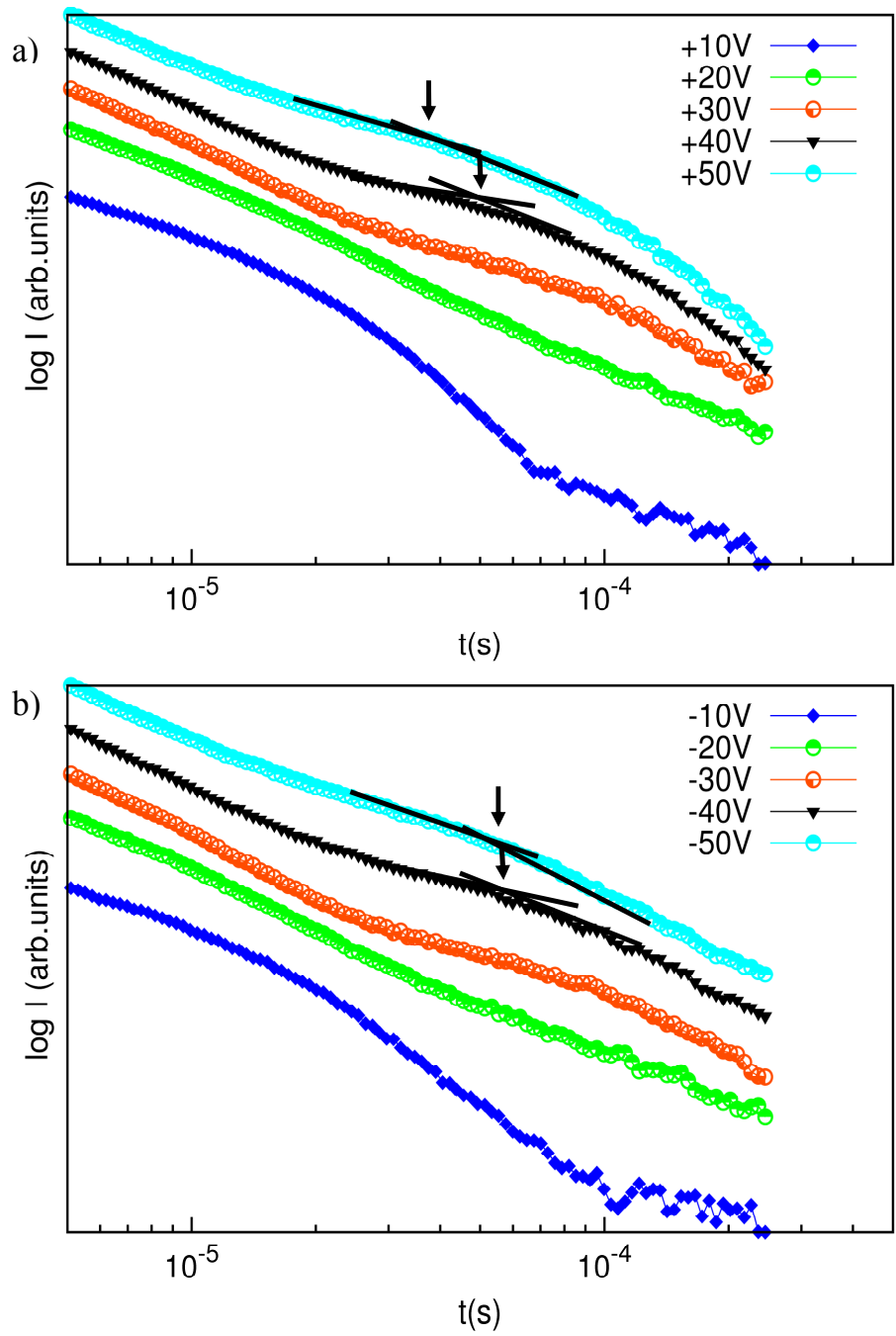


Figure 3.11: Double logarithmic plot of TOF measurements on reduced graphene oxide on Si/SiO₂ substrate at a channel length of 800 μm for a) positive and b) negative bias. These curves are shifted vertically for clarity.

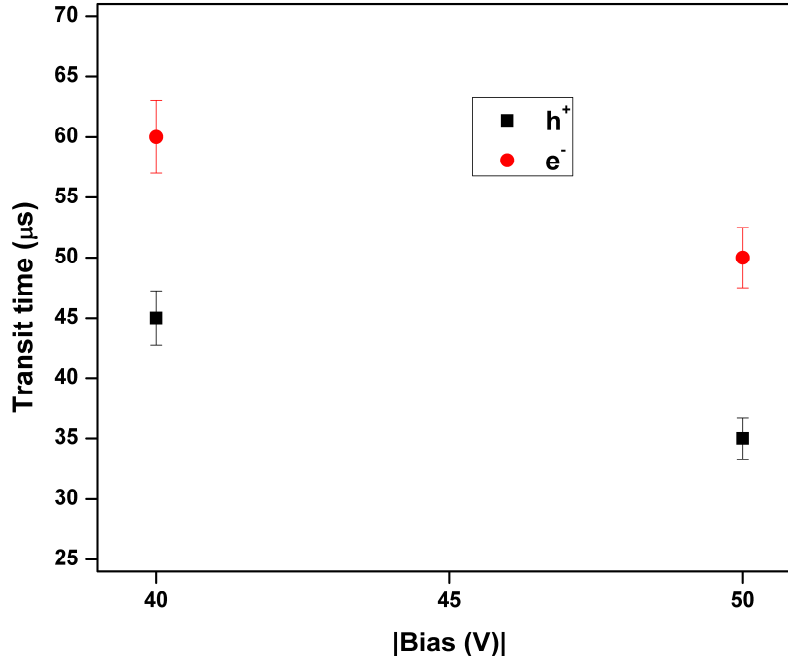


Figure 3.12. Variation of transit time as a function of applied bias for electrons and holes.

In Fig. 3.12, we present the variation of the transit time as a function of applied bias for electrons and holes. The error bar is estimated considering all the requirements for TOF measurements as explained in section 2.7. We have applied relatively low voltages, since we have reduced the channel length approximately 3 times, the charge (CV) inside the rGO layer on Si/SiO₂ is same as in case of rGO on fused silica and sapphire. Hence we neglect the contribution from it. Another parameter that changes in these measurements is circuit response time since we use 1kΩ resistor. The RC value in these measurements is 1.6×10^{-8} s, which is considerably less than the transit time, which is on the order of several μs. Hence we can neglect the error from it. Hence we estimate the error bar from the fit of both lines drawn on each curve as a function of angle. Assuming the constant electric field approximation the mobility estimated from the Eq. 2.1 $\mu = \frac{d^2}{Vt_{tr}}$ is 1200 cm²/Vs for rGO on fused silica and sapphire, which is 400 times more than on rGO on Si/SiO₂. The difference in the conductivity and carrier mobility on Si/SiO₂ substrates and the fused silica, sapphire substrates can be attributed to the morphology of the graphene layer on these substrates. The morphology is fairly different on these substrates. As per rGO on fused silica and sapphire substrates, rGO layer is continuous and no

individual graphitic domains are observed, except ripples and folds on sapphire substrate, which degrade the mobility compared to rGO on fused silica substrate. The morphology of rGO on Si/SiO₂ substrates instead is characterized by relatively large grain boundaries, which hinders efficient charge transport.

AFM images of morphology of rGO layer with different coverages on Si/SiO₂ substrates are compared in Fig. 3.13. An order of magnitude difference in the conductivity was observed between these two rGO layers. This effect is further manifested from the conductivity and TOF measurements on rGO on these substrates. The amount of photocurrent generated is nearly same in all cases.

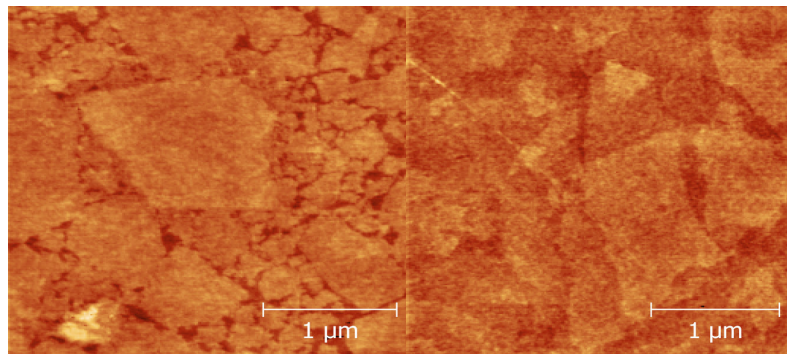


Figure 3.13: 3 μm ×3 μm AFM image of rGO on Si/SiO₂ having different surface coverage.

The electric field in the channel is position dependent and it is enhanced near the metal/channel interface and low electric field inside the channel [147]. When the carriers are excited near the biased electrode, due to electric field, it gives an initial surge in the photocurrent, when the carriers enter the low electric field region, the velocity of the carrier's decreases, when they reach the opposite electrode, a region of high electric field is experienced [147]. In case of highly ordered materials, plateau or cusp can be observed, followed by a rapid decay of the photocurrent. But in TOF curves of rGO on Si/SiO₂, no such plateau or cusp is observed, which implies that it is highly disordered. Due to discontinuity of the layer and presence of grain boundaries between the graphene domains, the mobility is reduced. Since the carrier will spend more time between these domains to pass through defect clusters, thus limiting the mobility. But in rGO on fused silica and sapphire substrates, rapid decay of the photocurrent is observed when the carriers reach the opposite electrode. Due to the well connected regions of rGO on fused

silica and sapphire, conductivity has increased by two orders of magnitude as well as mobility.

3.2 The effect of doping in graphene

Charge transfer doping is one of the best way to manipulate the electric charge transport properties of graphene. The performance of GFETs and their reliability is mainly dominated by the graphene/dielectric interface and its surrounding environment [104-106]. The impurities on the surface of the dielectric, roughness and surface polar phonon scattering from the adjacent dielectric surface can all affect the charge transport of the device.

3.2.1 Hysteresis in graphene field effect transistors

The schematic representation of the effect of charge injection from graphene to the dielectric interface and its effect on the hysteresis is as shown in Fig. 3.14.

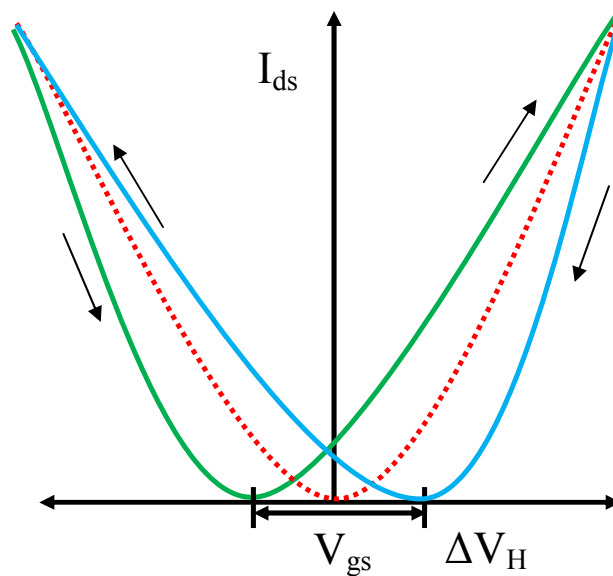


Figure 3.14: The schematic representation of the effect of charge injection from graphene to the dielectric interface. The red-dotted line represents an ideal curve with no interface traps. The arrows indicate the direction of the gate-voltage sweep. The difference between the two conductivity minima is ΔV_H .

If there are no traps between the dielectric and graphene interface, the conductivity minimum $V_{Dirac} = 0$ V (red dotted line in Fig. 3.14). When V_{gs} is at negative values,

holes from graphene are gradually injected into the traps at the graphene-dielectric interface, screening thereby the electric field due to V_{gs} , and graphene layer senses a more positive potential than that due to V_{gs} . The resulting potential of graphene relative to gate is lower. V_{Dirac} is shifted to negative gate voltages as shown in Fig. 3.14 (green curve). Similarly, when V_{gs} starts from positive voltage, electrons are injected into the trapping sites, screening thereby the electric field due to V_{gs} . The resulting potential of graphene relative to gate is lower. The V_{Dirac} is shifted to positive gate voltages as shown in Fig. 3.14 (blue curve). ΔV_H is the difference between V_{Dirac} in the forward and backward sweeps and it can be used to estimate the density of the traps between the dielectric/graphene interface n_{tr}

$$n_{tr} = \frac{\Delta V_H C_{ox}}{e} \quad (3.1)$$

where C_{ox} is the gate capacitance and e is the electron charge [104,107].

Graphene is an ambipolar material. It has been demonstrated that the ambipolar properties of graphene can be modulated by adsorption of organic molecules of either electron acceptor or electron donor that would lead to p-type or n-type graphene respectively [110-115].

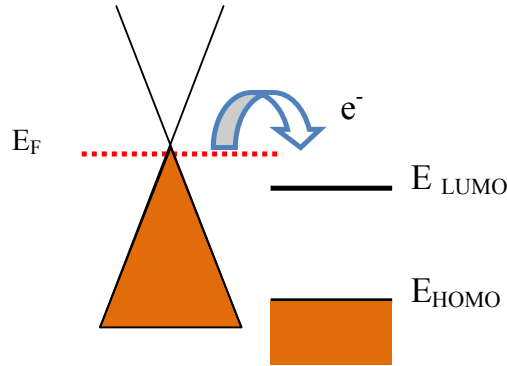


Figure 3.15: Schematic of p-type doping process of graphene [116].

The transfer of charge is determined by the relative position of the energy levels of the graphene and HOMO and LUMO of the adsorbates. The schematic view of the p-type doping process of graphene is shown in Fig. 3.15. When Fermi level of graphene is higher than LUMO of the acceptor molecule, the electrons are transferred from graphene to acceptor molecule, and the effective Fermi level shifts towards the valence band resulting in p-type doping. In a similar way, when the

Fermi level of the graphene is below than HOMO of the donor molecule, the electrons will be transferred from the adsorbate to graphene, the charge flow continues until it shifts the Fermi level of graphene causing thereby n-type doping as shown in Fig. 3.16 [116].

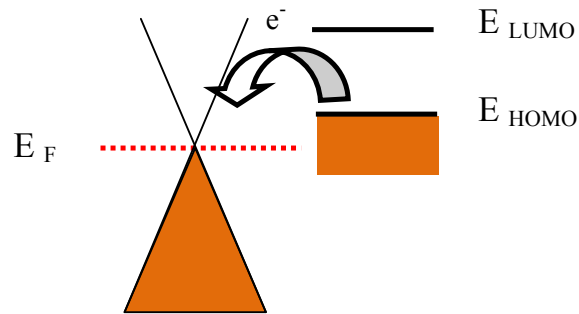


Figure 3.16: Schematic of n-type doping process of graphene [116].

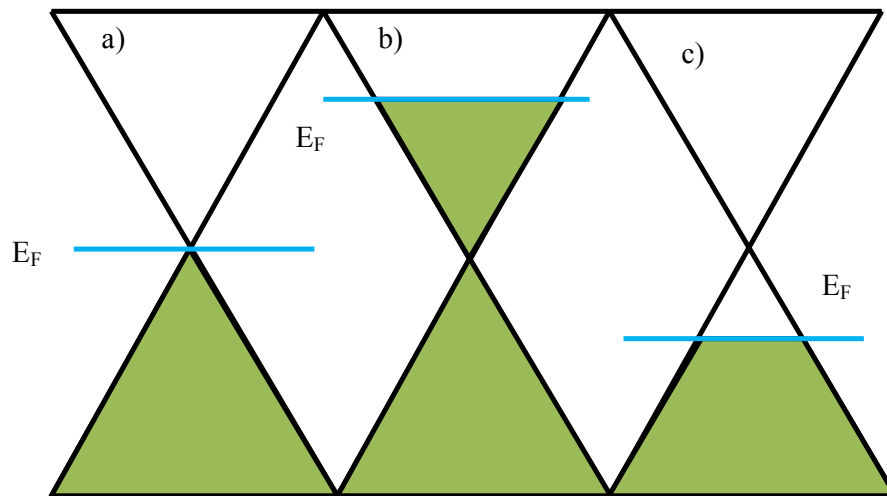


Figure 3.17: Illustration of the schematic band structures of a) pristine b) n-type and c) p-type graphene [116].

Hence, the adsorbate molecule pin the Fermi level of graphene into the molecular negatively charged state at the interface. The Fermi level of pristine graphene, n-type and p-type doped graphene are shown in Fig. 3.17.

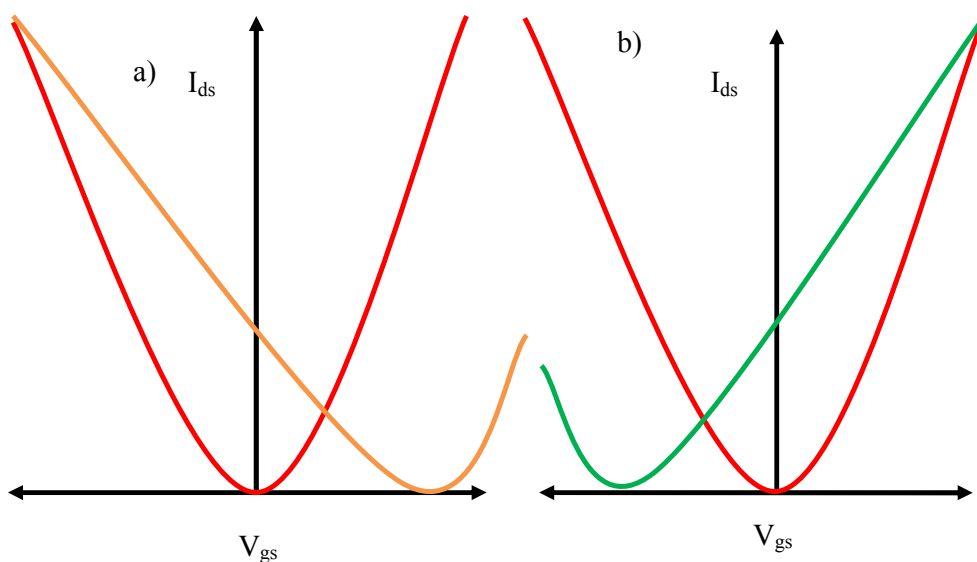


Figure 3.18: a) The effect of p-type doping on the conductivity minimum in GFETs. The charge neutrality point shifts towards positive gate voltages b) the effect of n-type doping in GFETs. The charge neutrality point shifts towards negative gate voltages.

Electrical conductivity of doped graphene can be measured by GFETs. The relationship between the conductivity and gate voltage of pristine graphene is a characteristic V-shaped curve as shown in Fig. 3.18 (red curve). The effect of p-type or n-type doping on the conductivity minimum of GFET is shown in Fig. 3.18. In case of p-type doping, graphene will transfer electrons into adsorbates and leaving holes in graphene, thus we need to apply a more positive gate voltages in order to get charge neutrality point as shown in Fig 3.18a) (orange curve). In case of n-type doping, additional electrons will be transferred to graphene, hence we need to apply more negative gate voltages in order to get the charge neutrality point as shown in Fig. 3.18b) (green curve) [115].

Molecules with electron withdrawing groups adsorbed on the surface will lead to p-type doping and molecules with donating groups lead to n-type doping. Aromatic [112] and nonaromatic molecules are a good choice for doping of graphene [118]. Tian *et al.* has theoretically showed that tetrafluoro-tetracyanoquinodimethane

(F4-TCNQ) molecule is a strong electron acceptor [119]. Coletti *et al.* demonstrated that F4-TCNQ is a p-type dopant and it can be used to tune the Fermi level of graphene by noncovalent functionalization and controlling the surface coverage [120]. Electrical measurements on GFETs suggest that the aromatic molecules with electron-donor groups (e.g. 9,10-dimethylantracene (An-CH₃), 1,5-naphthalenediamine (Na-NH₂)) cause n-doping, while those with hole acceptor groups impose p-doping (e.g., 9,10-dibromo-anthracene (An-Br), tetrasodium 1,3,6,8-pyrenetetrasulfonic acid (TPA) on graphene[112]. Tetracyanoethylene (TCNE) is a strong electron acceptor can also leads to p-type doping [116]. Ammonia and ethanol act as electron donors. N-type doping is also possible with NH₃ plasma and nitrogen ion irradiation [121,122].

3.3 P-type doping of rGO with 1-pyrene butyric acid

3.3.1 Introduction

Pyrene-based surfactants have been shown to be very effective in interacting with graphene and stabilizing it in solutions [136, 137]. 1-pyrene butyric acid (PBA) is used to exfoliate graphene, because it is able to adsorb on rGO surface, interacting with it by supramolecular interactions, while its charged hydrophilic groups increase the solubility of graphene. PBA or its derivatives have been successfully used to prepare macroscopic membranes of rGO paper [138], or even to functionalize rGO sheets for selective detection of cancer biomarkers [139].

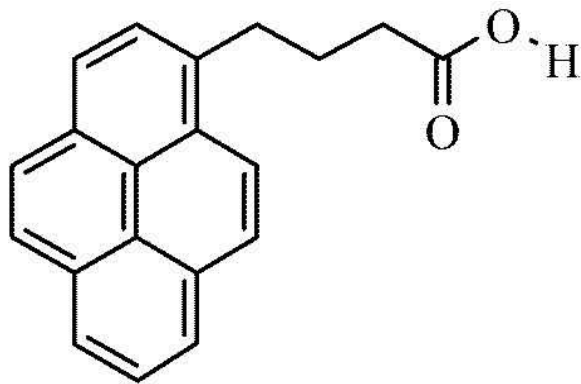


Figure 3.19: Molecular structure of 1-pyrene butyric acid.

3.3.2 Experimental

Charge carrier transport was examined by measuring transfer characteristics on FETs with PBA-covered rGO channels, and by TOF measurements of photoinduced charge carriers. Transfer characteristics were measured on the samples fabricated on substrates comprising 300 nm-thick SiO₂ on p-type Si(001) wafers. rGO sheets were synthesized using a modified Hummer's method from natural graphite flakes [148]. A 3 nm-thick GO layer was deposited on such surface and reduced to graphene, followed by a subsequent deposition of 10 nm-thick PBA layers by spin coating. Au electrodes are deposited on top of rGO surface. The length of the FET channel between Au electrodes was 50 μm. To this end, PBA was dissolved in methanol at a concentration of 2 μg/ml. The transfer characteristics were measured with Keithley Sourcemeter 2400 and Picoammeter 6487 in the nitrogen filled glove box at room temperature. The samples for TOF measurements comprised rGO layers deposited on fused silica. Co-planar Al contacts separated by 2500 μm were thermally evaporated on these samples. Three subsequent depositions were examined and the amount of PBA was estimated from the analysis of AFM images. The excitation source for TOF measurements was pulsed Nd:YAG laser of wavelength 210 nm with pulse duration of 3 ns. The bias voltages applied to the samples were varied from -200 V to 200 V with a step of 50 V. The displacement current of the charge carriers in the channel was recorded with a 2.5 GHz (LeCroy) oscilloscope. To detect very small currents corresponding to low electric fields, an amplifier was used (Miteq AM-1309).

3.3.3 Results and Discussion

In Fig. 3.20 we compare transfer characteristics of rGO-based FET without (topmost curve) and with PBA layer (bottommost curve). The arrows indicate the direction of changing the V_g that was swept in the range of ± 100 V. The curves exhibit relatively broad minimum that is an indication of presence of disorder in rGO [149]. We see that the V_{Dirac} occurs at positive V_g . The position of V_{Dirac} reflects the density of the charge carriers near the Fermi level, and its shift towards positive voltages is due to the electron-hole puddles at the SiO₂/rGO interface [125], and to unintentional p-type doping from due to exposure to air and ambient humidity [123, 115, 149, 150]. In addition, relatively strong hysteresis was observed upon sweeping

V_g from -100 V to 100 V and then back to -100 V, and is related to the charge transfer across the interface between the rGO layer and SiO_2 [123, 104]. By using $\Delta V_{\text{H}}=8$ V, for clean rGO and measured gate-oxide capacitance $C_{\text{ox}}= 6.25 \text{ nF/cm}^2$, we calculated the areal trap density using Eq. 3.1 to be $n_{\text{tr}}= 5.75 \times 10^{11} \text{ cm}^{-2}$.

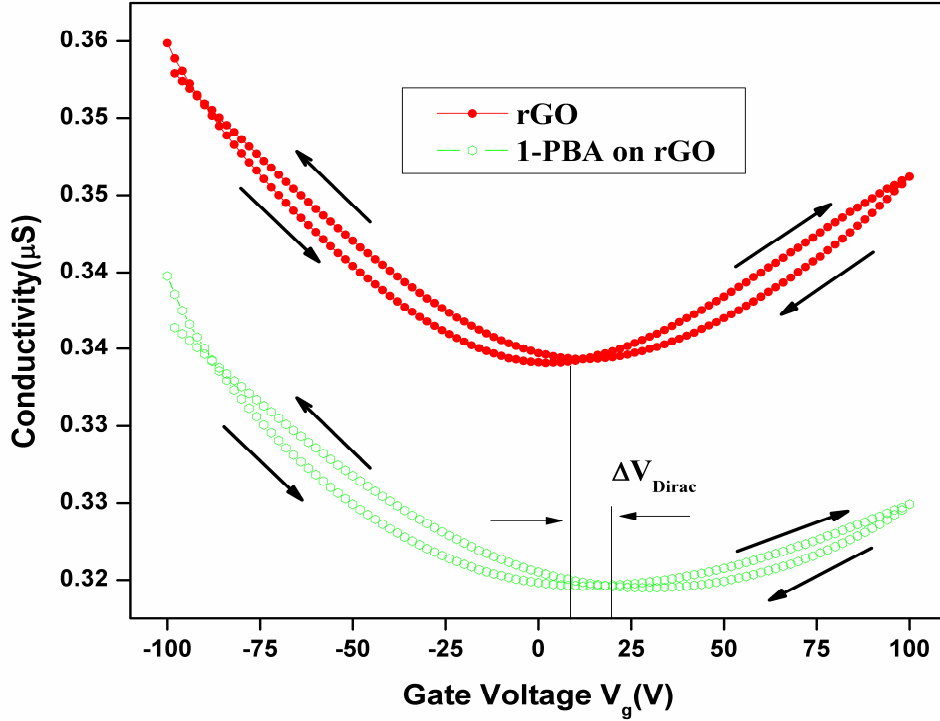


Figure 3.20: Normalized 2D conductivity as a function of gate voltage obtained in rGO-based FET without (topmost curve) and with (bottommost curve) 1-pyrene butyric acid. The arrows indicate the direction of the voltage sweep. ΔV_{Dirac} represents the change in the Dirac voltage upon deposition of PBA on reduced graphene oxide.

This value compares favorably to typically reported values of $3.5\text{-}5 \times 10^{11} \text{ cm}^{-2}$ for Si-based FETs [151]. Upon deposition of PBA layer, the transfer curve exhibits a substantial positive shift (bottommost curve, Fig. 3.20) indicating an increase in p-type doping of rGO. Moreover, we observe a strong increase in V_{Dirac} , which amounts to 18 V. Using this value we calculated the density of trapped charges to be $1.3 \times 10^{12} \text{ cm}^{-2}$. Assuming that the density of traps located at the Si/ SiO_2 interface, and in the bulk of SiO_2 layer, remains unchanged, the additional traps must result from the interaction of PBA molecules with rGO. This is further supported by the observed reduction in drain current for the PBA covered samples. The observed shift in V_{Dirac}

to positive values upon PBA layer deposition and an increase in ΔV_H is therefore a consequence of electron transfer from rGO to PBA. The remaining positive charges in rGO effectively screen V_g so that it is effectively reduced for negative values. We note, that the role of solvent in affecting the charge transport was ruled out by performing experiments comprising drop-casting pure methanol. No effect on transfer characteristics was observed in this case.

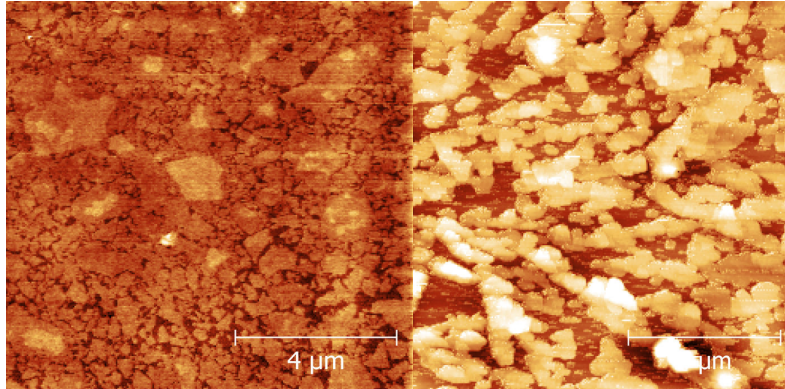


Figure 3.21: $10\mu\text{m}\times 10\mu\text{m}$ AFM image of rGO without (left) and with PBA (right). The scale is 0 to 3 nm for rGO without PBA and the scale is 0 to 60 nm for rGO with PBA on top.

The resulting thickness of PBA may vary over the sample by few nm. The variation of thickness is likely the result of increasing molecular sticking coefficient at the grain boundaries of rGO. Regardless, of surface roughness, the PBA layer was thick enough over all surface to ensure sufficient interface electron transfer to be detected by transport measurements. AFM images of rGO without and with PBA are shown in Fig. 3.21. The RMS roughness of the rGO layer changes from 1 nm to 10 nm without and with PBA. Somewhat lower charge transfer is indeed expected for thick organic layers, as a result of intermolecular interactions and depolarization effects. Despite relatively weak electron transfer between PBA and graphene we see that the effect of PBA on ΔV_{Dirac} is appreciable. This could argue for the role of disordered regions present in rGO that are more susceptible to interaction with PBA molecules.

The absorption in PBA peaks at 410 nm, and drops rapidly towards the ultraviolet region. Relatively low coverage of PBA in TOF experiments represents only a small supply of exciton-related charge that we detected in our $I(t)$ curves. In addition, the measurements were performed by illumination in the region near the

electrodes, blocking a good part of the laser beam reaching the PBA-covered surface. By varying the laser intensity we have further checked that no charge saturation effects are affecting the data.

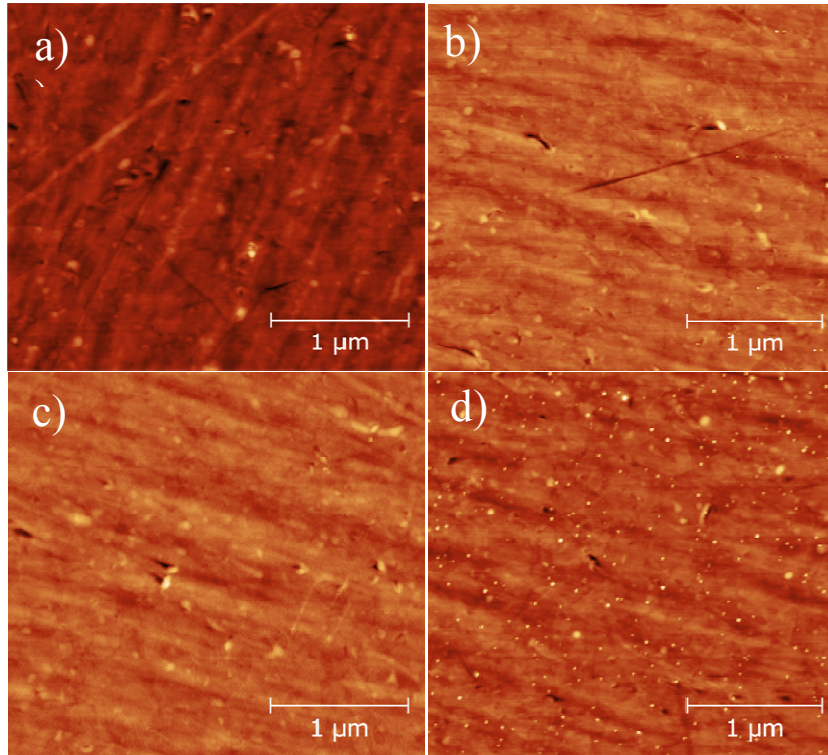


Figure 3.22: Atomic force microscopy topography scan of a) clean rGO surface, and b)-d) three subsequent coverages of PBA obtained by spin coating. The height range is 15 nm and is same for all the images.

To explore further the effect of PBA on charge transport we have reduced the amount of PBA on rGO to submonolayer coverages. The effect of PBA on electric charge transport on rGO at small coverages was examined using the TOF on three submonolayer coverages of PBA on rGO. Fig. 3.21 compares AFM topography scans of the clean rGO surface (Fig. 3.22 a), and three subsequent coverages of PBA (Figs. 3.22 b, c, and d). The bright dots are the islands of PBA that formed during spin coating. The average height of the islands is 1.7 ± 0.3 nm for all three coverages, but the lateral dimensions and the areal density of the islands increases with increasing coverage. From a series of AFM images we have used a threshold method to estimate the PBA coverage, and obtained the values of 0.08 %, 0.19 %, and 1.3 % of the surface for the first, the second and the third deposition of PBA, respectively. The fact that the average height of the islands does not change with increasing

coverage, argues for the strain related mechanisms that limit vertical growth of the islands. After each deposition we have performed time-dependent photocurrent measurements.

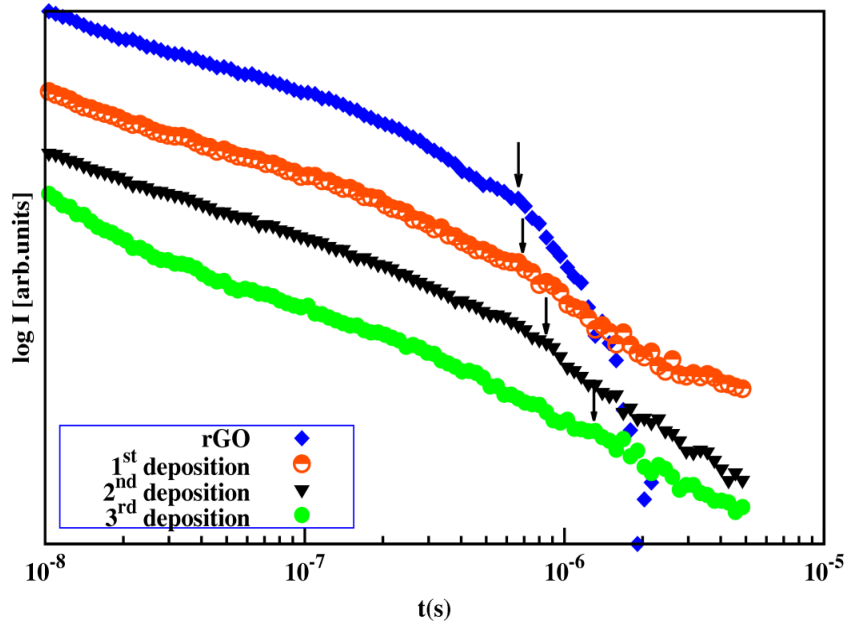


Figure 3.23: Double logarithmic plot of photocurrent vs time. The effect of PBA on the transient response of the rGO after each deposition for a bias voltage of -50 V at a wavelength of 210 nm. The arrow indicates the transit time. These curves are artificially shifted from one over another.

The representative results are shown in Fig. 3.23, where we compare time-dependence of the electron photocurrent (top to bottom) for pristine rGO and Focusing on the $I(t)$ curve for a clean rGO (topmost curve), we see a monotonous decrease of photocurrent until a small shoulder is observed, followed by a rapid decrease of photocurrent. Here we note that an $I(t)$ curve represents the current due to the photoinduced charge carriers drifting in the direction of the electric field from the biased electrode to the opposite (collecting) electrode. The drift of the charge carriers in the opposite direction, i.e. to the biased electrode is too fast to be discerned in the $I(t)$ curve. We note that the electric field in the interelectrode region is not constant, but is highly localized near the electrodes in the region on the order of few μm [145]. This non-uniformity of the electric field crucially determines the lineshape of $I(t)$ curve. The carriers that are photogenerated near the biased electrode are accelerated

in the high-field region near the electrode. As they enter the low-field region in the middle of the channel, the current decreases and exhibits a sharp rise as the carriers enter the high-field region near the collecting electrode. Such $I(t)$ lineshape is expected, if the energy distribution of the transporting states, responsible for hopping transport, is sufficiently narrow. For broader energy distributions the appearance of the peak signaling the arrival of the charge carriers to the collecting electrode is less obvious. The position of the cusp, or of the evident change in slope of $I(t)$ curve, is a signature of the arrival of the $\sim 10\%$ of the fastest charge carriers to the collecting electrode. The mean transit time of the photogenerated charge carrier ensemble corresponds to the time, after $I(t)$ drops to its half cusp value[147].

The lineshape of $I(t)$ in Fig. 3.23 (topmost curve) is typical for the transport in disordered media (hopping, percolation)[152,153] in which spatial distribution of charge carriers exhibits initially a strong localization in the region of high electric field near the illuminated electrode, followed by a spread of distribution throughout the channel. The average charge carriers exhibit position dependent velocity. A rapid decay of the photocurrent observed after the shoulder is an indication of relatively low concentration of traps that would immobilize the charge carriers for times that are substantially longer than the transit time of an average carrier. At the PBA coverage of 0.08 % we observe a significant change in $I(t)$ (filled circles) that exhibits a long, slowly decaying tail and a slight increase in transit time (marked with the arrow). The slowly decaying tail is an indication of the presence of the trap states that block the electrons for times that are longer than the average transit time. The increase of the transit time is an indication that the mobility of the carriers is reduced, most likely due to recombination with the localized holes in rGO that emerge from the electron transfer from rGO to PBA molecules. For increasing PBA coverage the contribution of slowly decaying tail becomes increasingly important, and at the coverage of 1.3% almost completely masks the shoulder in $I(t)$ that was observed on clean rGO. These measurements indicate a remarkable sensitivity of TOF measurements to detect the effect of doping on rGO. In Fig. 3.24, we compare time-dependence of the hole photocurrent (top to bottom) for pristine rGO and three subsequent depositions of PBA. No appreciable change of transit time (indicated by arrows) is observed.

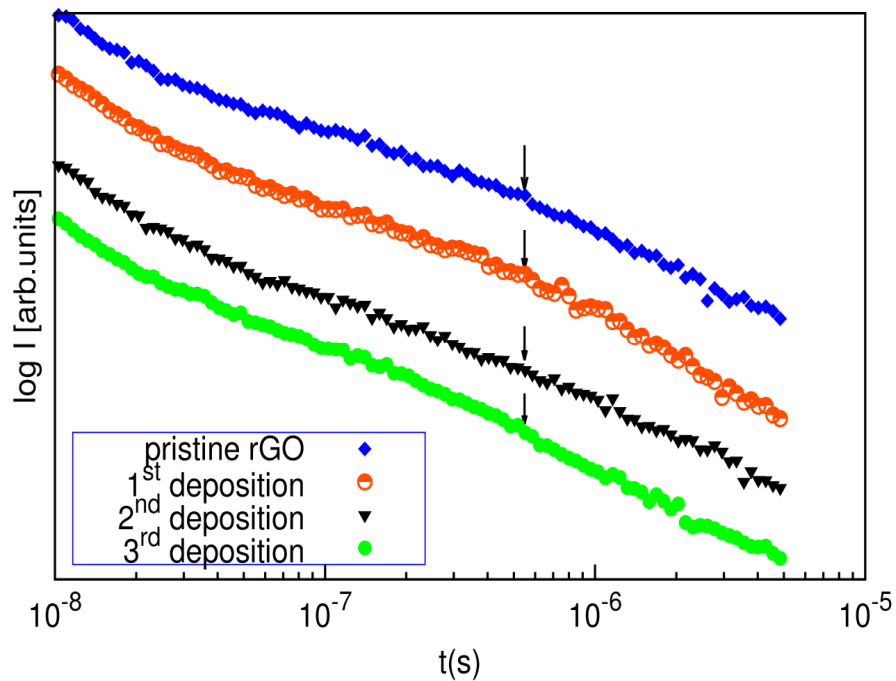


Figure 3.24: Double logarithmic plot of photocurrent vs time. The effect of PBA on the transient response of the rGO after each deposition for a bias voltage of +50 V at a wavelength of 210 nm. The arrow indicates the transit time. These curves are artificially shifted for clarity.

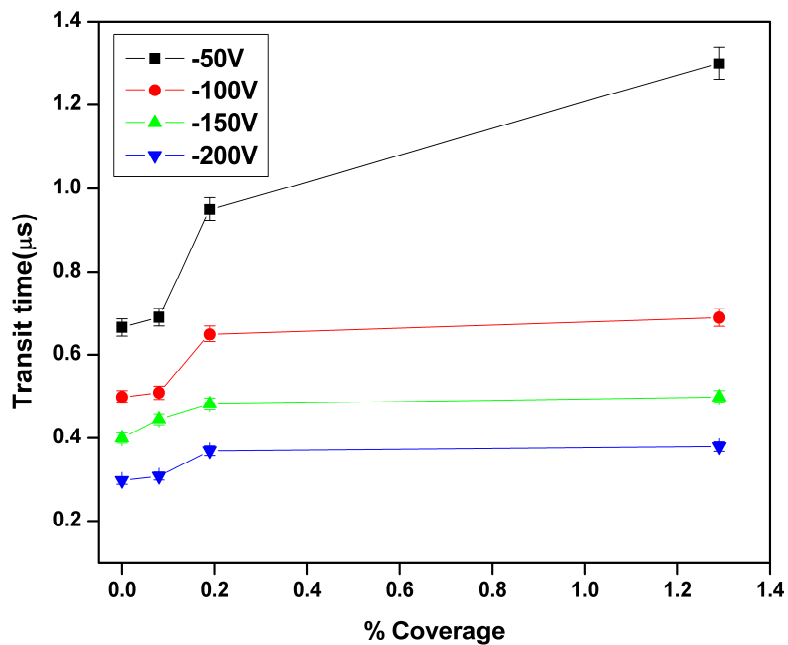


Figure 3.25: Variation of the transit time for different surface coverage of PBA for different bias voltages.

Extremely high sensitivity of charge transport in rGO to the presence of ultra-low coverages of organic dopants could be due to the non-uniform nature of rGO on a nanometric scale, with the presence of limited areas of conjugated carbon atoms, separated by holes and oxidized, insulating patches [130], which restricts charge transport, creating bottlenecks and hindering percolation. If an adsorbate has preferential affinity for the most aromatic areas of the rGO, it shall concentrate on the few conductive paths present in the material, thus maximizing its effect on charge transport even for very low quantities.

Fig. 3.25 summarizes the data for the transit time for all three coverages. The variation of the transit time is more pronounced at lower voltages than at higher voltages. This is because at lower voltages the velocity of the carriers is lower, and results in higher probability for these carriers to be captured into the trap states. As the bias voltage increases, the velocity of the carriers also increases; hence the probability for these carriers to be captured into the trap states and the recombination sites is reduced. From these measurements it is evident that increasing the velocity of the carriers at high bias voltage decreases the probability of capture of the carriers into the recombination sites and trap states.

3.4 N-type doping of graphene with tetrathiafulvalene

3.4.1 Introduction

Tetrathiafulvalene (TTF) is a strong electron donor (hole acceptor), which is widely studied both theoretically [116] and experimentally [159]. Several theoretical studies based on density functional theory of TTF on adsorbed on graphene have

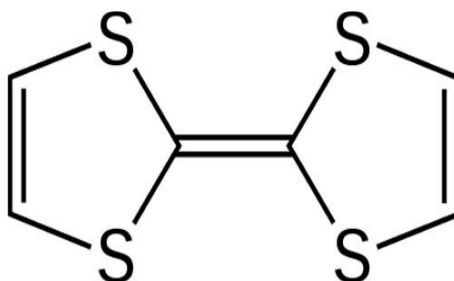


Figure 3.26: Molecular structure of tetrathiafulvalene.

been reported [116]. Charge carrier transport was examined by measuring transfer characteristics on FETs with TTF-covered rGO channels, and by TOF measurements of photoinduced charge carriers.

3.4.2 Experimental

Transfer characteristics were measured on the samples fabricated on substrates comprising 300 nm-thick SiO₂ on p-type Si(001) wafers with on which 3 nm GO layer was deposited and reduced to graphene. Gold electrodes are deposited using electron beam evaporation using a shadow mask. The length of the FET channel between Au electrodes was 50 μm and width is 0.5 cm. TTF was dissolved in chloroform at a concentration of 1 mg/ml and then spincoated at a speed of 1500 rpm. The transfer characteristics were measured with Keithley Sourcemeter 2400 and Keithley Picoammeter 6487 in the nitrogen-filled glove box at room temperature. The samples for TOF measurements comprised rGO layers deposited on fused silica and the separation between the coplanar Al electrodes was 800 μm. The bias voltage applied to the samples was varied from -100 V to 100 V with a step of 25 V. The molecular weight of TTF =204.36. We have made the solution of TTF in chloroform with a concentration of 1 μg/ml. In order to have the solution to contain 1.3×10^{-10} moles/cm², we have dropcoated the 26.5 μl in each deposition. We have performed TOF measurements after the deposition of TTF.

3.4.3 Results and Discussion

In Fig. 3.27 we compare transfer characteristics of graphene FETs without (blue filled squares), and with TTF layer (red filled circles). The arrows indicate the direction of changing V_g that was swept in the range of ±100 V at a rate of 4 V/s. We see that the V_{Dirac} occurs at positive V_g. From ΔV_H=3 V and C_{ox}= 6.25 nF/cm² using Eq. 3.1, we calculated the areal trap density to be n_{tr}= 1.15×10¹¹ cm⁻². Upon deposition of TTF layer, the transfer curve exhibits V_{Dirac}=-1 V (red filled circles, Fig. 3.27) indicating n-type doping of rGO and the resulting in ΔV_{Dirac} is -4 V. Using this value we calculated the density of trapped charges to be 1.56×10¹¹ cm⁻². Assuming that the density of traps located at the Si/SiO₂ interface, and in the bulk of SiO₂ layer, remains unchanged, the additional traps must result from the interaction

of TTF molecules with rGO that will trap the charge in rGO. The observed shift in V_{Dirac} to negative values upon TTF layer deposition and an increase in ΔV_{Dirac} is therefore a consequence of electron transfer from TTF to rGO.

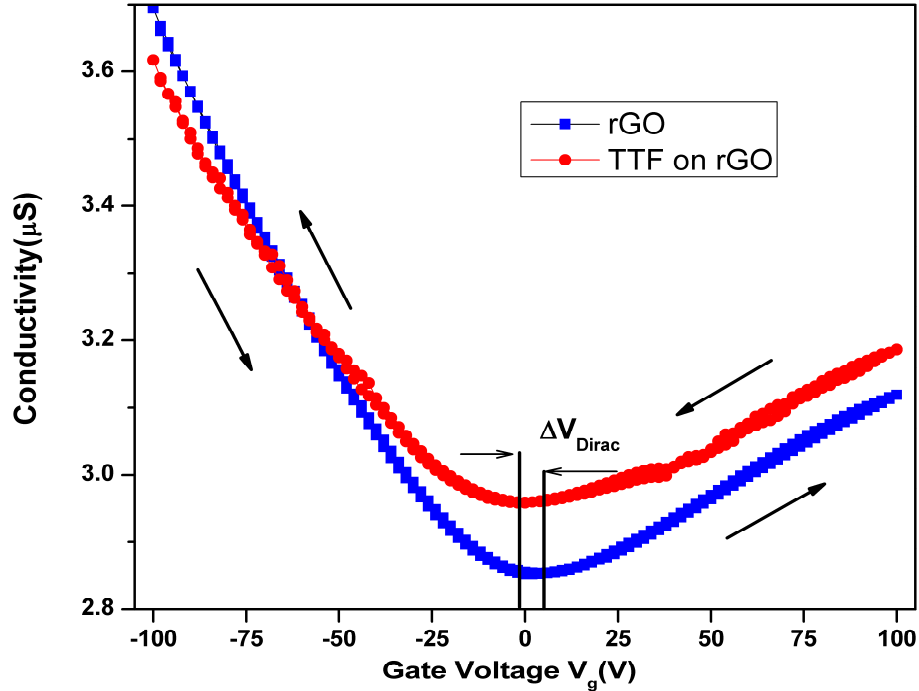


Figure 3.27: Normalized 2D conductivity as a function of gate voltage obtained in rGO-based FET without (blue filled squares) and with (red filled circles) tetrathiafulvalene. The arrows indicate the direction of the voltage sweep. ΔV_{Dirac} represents the change in the Dirac voltage upon deposition of TTF on reduced graphene oxide.

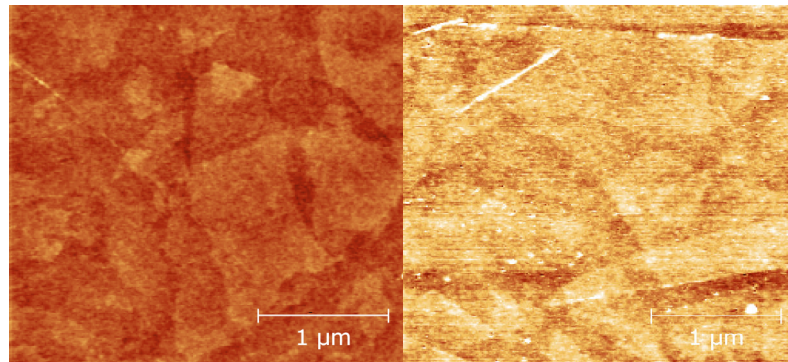


Figure 3.28: $3\mu\text{m}\times 3\mu\text{m}$ AFM image of rGO on Si/SiO₂ substrates without and with TTF. The scale is 0 to 3 nm and it is same for both images.

AFM image of topography of rGO on fused silica without and with TTF is shown in Fig. 3.28. The RMS roughness of the layer changes from 0.2 nm to 0.36 nm upon TTF deposition. The bright dots are the islands of TTF that formed during spin coating. The TTF molecules are deposited at the grain boundaries, which is likely the result of different molecular sticking coefficient and implies that the disordered regions are more susceptible to interact with TTF molecules.

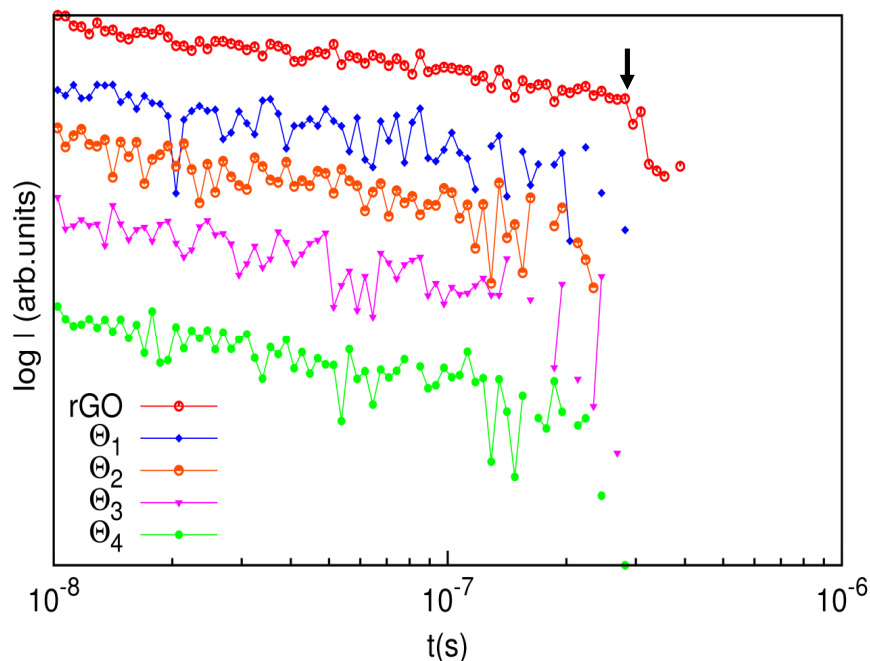


Figure 3.29: Double logarithmic plot of photocurrent vs time. The effect of TTF on rGO at a voltage of +25 V after each deposition at a wavelength of 210 nm. The curves are shifted vertically for clarity. Θ_1 , Θ_2 , Θ_3 , Θ_4 represent the 1st, 2nd, 3rd, 4th depositions.

The effect of TTF on TOF measurements of rGO for a voltage of +25 V for different depositions is shown in Fig. 3.29. Since TTF is an electron donor (hole acceptor) and its HOMO is higher than the work function of graphene, it will donate electrons to rGO. For pristine rGO, we see that the photocurrent decreases monotonically until a sharp drop of photocurrent which occurs at 2.8×10^{-7} s (topmost curve) indicated with an arrow. After the first deposition of TTF on rGO, the hole photocurrent is completely quenched and only noise is observed (blue curve). The amount of photocurrent generated is also decreased to half of its previous value,

since TTF has some absorption at 210 nm. TTF has maximum absorption at 300 nm wavelength and drops slowly towards ultraviolet region [211]. The amount of photocurrent generated slightly decreases with further depositions. Since TTF is an electron donor, we expect the electrons that are transferred from TTF into rGO to be recombined with the holes in rGO.

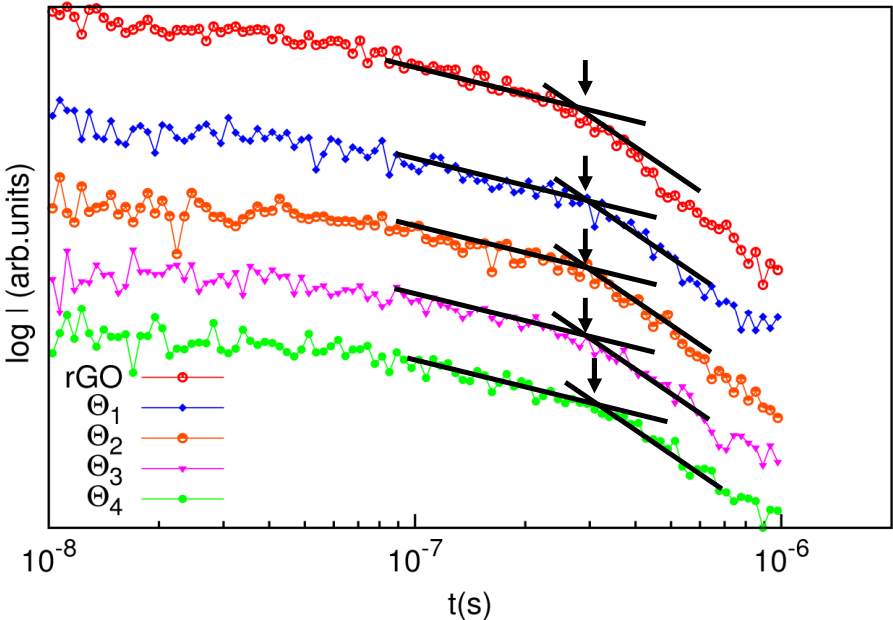


Figure 3.30: Double logarithmic plot of photocurrent vs time. The effect of TTF on rGO at a voltage of -25 V for different amounts on it at a wavelength of 210 nm. The curves are shifted vertically for clarity. Θ_1 , Θ_2 , Θ_3 , Θ_4 represent the 1st, 2nd, 3rd, 4th depositions.

Due to the absorption in TTF the number of photogenerated carriers decreases and some of the holes will recombine with the electrons that are transferred from TTF into rGO. Hence substantial amount of hole photocurrent decreases and only noise is observed. We see that the amount of electron photocurrent decreases in the same way due to the absorption in TTF, but it is not affecting the transit time, indicated by arrows as shown in Fig. 3.30 for the bias of -25 V. Since TTF is an electron donor, it doesn't affect the electron charge transport. The effect of TTF on TOF measurements on rGO at a voltage of +100 V after each deposition at a wavelength of 210 nm is shown in Fig. 3.31.

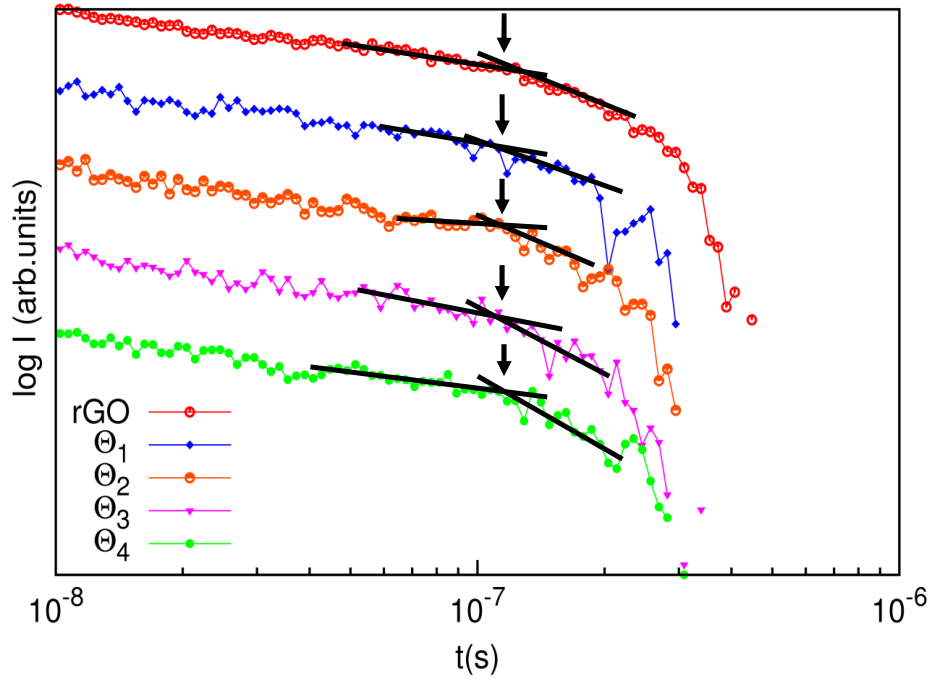


Figure 3.31: Double logarithmic plot of photocurrent vs time. The effect of TTF on rGO at a voltage of +100 V after each deposition at a wavelength of 210 nm. The curves are shifted vertically for clarity. Θ_1 , Θ_2 , Θ_3 , Θ_4 represent the 1st, 2nd, 3rd, 4th depositions.

From the TOF curve for clean rGO, we determine the transit time to be at 1.2×10^{-7} s as indicated by an arrow (topmost curve). After deposition of TTF, the amount of photocurrent decreases and signal to noise is decreases, due to absorption in TTF. As the voltage increases, the photocurrent also increases. But due to absorption in TTF, the amount of photocurrent decreases and some holes are recombined with the electrons that are transferred from TTF into rGO. The transit time is indicated by the arrows in Fig. 3.30. But at lower voltages (Fig. 3.28), since the photocurrent is low, the hole photocurrent is completely quenched.

3.5 Conclusions

We have characterized rGO on fused silica, sapphire and Si/SiO₂ substrates by TOF technique. rGO exhibits more than two orders of magnitude high conductivity on fused silica and sapphire substrates than on Si/SiO₂ substrates. We attribute the difference in conductivity to the morphological differences of rGO

layers grown on different substrates. The mobility estimated from TOF measurements is in good agreement the rGO-based FETs and on Si/SiO₂. P-type and n-type graphene was obtained using electron acceptor and electron donor via surface-transfer doping. We have observed significant positive shift of the conductivity minimum in transfer characteristics upon exposing rGO-based FETs to PBA. Our time-resolved photoconductivity measurements have demonstrated that PBA coverages as low as 0.08% significantly affect charge transport in rGO. On the other hand, rGO-based FETs show a negative shift of the conductivity minimum upon exposing to TTF, which is a strong electron donor. The TOF measurements on rGO after the deposition of TTF show that the amount of photocurrent generated decreases due to absorption of TTF at 210 nm wavelength.

Chapter 4: Comparison of effect of weak and strong electron acceptors on rGO

In this chapter we present a systematic study of the effect of p-type dopants on electric charge transport in rGO layers. We have examined the effects of thin layers of 1-pyrenesulfonic acid sodium (1-PSANa) salt and strong electron acceptors like F4-TCNQ and TCNE on transfer characteristics of GFETs and correlated with TOF measurements.

4.1 Materials

1-PSANa salt is used for the liquid phase exfoliation of graphene based on supra-molecular and non-covalent interactions between graphene and 1-PSANa to obtain a stable dispersion of graphene by using only water as solvent [157,158].

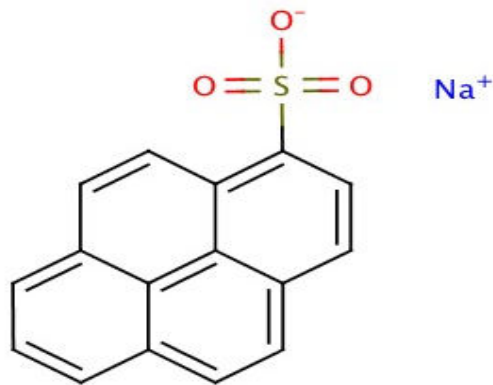


Figure 4.1: Molecular structure of 1-pyrenesulfonic acid sodium salt.

Y.H. Lu *et al.* has theoretically proved that TCNE is a strong electron acceptor and demonstrated that a p-type graphene can be obtained via charge transfer between TCNE and graphene at a controllable rate based on density functional theory calculations [162]. Tao Hu *et al.* has proved that for monolayer graphene with a molecular concentration of 1% of TCNE, 0.5 electrons will be transferred without changing the electronic structure [116].

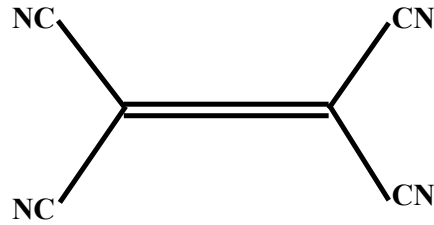


Figure 4.2: Molecular structure of TCNE molecule.

Tian *et al.* has proved theoretically with F4-TCNQ concentration of 1.3×10^{-10} moles/cm², the charge transfer between each F4-TCNQ molecule and graphene is $0.45 e$, and the built-in electric field (E_{bi}), between the graphene and F4-TCNQ could reach 0.070 V/\AA [119]. One of the main advantage of employing F4-TCNQ as a strong molecular acceptor to modify the graphene surface is that no defect or strong structural conformation (rotation of atoms in a molecule gives same structure) was created; hence, the graphene could retain its perfect two-dimensional honeycomb

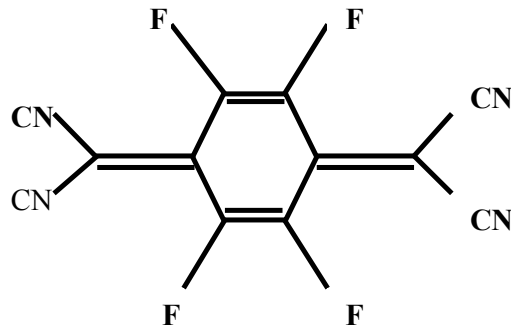


Figure 4.3: Molecular structure of F4-TCNQ molecule.

structure. The structural conformation was possible in molecules having cyano groups (CN), where all the atoms lie along the axis of a central single bond. But this is not possible in the molecules which are having complex structures. Another advantage is that no clustering of molecules is observed, due to the repulsion of charged F4-TCNQ anions between each other at high coverage. A F4-TCNQ-doped CNT FET has been fabricated experimentally, and it was found that the device performances such as transconductance, on-resistance, and I_{on}/I_{off} ratio were improved by F4-TCNQ [120,163-166].

4.2 Experimental

Charge carrier transport was examined by measuring transfer characteristics on rGO-based FETs without and with 1-PSANa, TCNE, F4-TCNQ and by TOF measurements of photoinduced charge carriers. Transfer characteristics were measured on the samples fabricated on substrates comprising 300 nm-thick SiO₂ on p-type Si (001) wafers. GO sheets were synthesized using a modified Hummer's method [148] from natural graphite flakes and a 3-nm thick layer of GO was deposited on these substrates and reduced to graphene in UHV at 700 °C. Gold electrodes were deposited onto rGO using a shadow mask. The length of the channel was 50 μm having width of 0.5 cm. 1-PSANa dissolved in methanol and deposited by spin coating onto rGO surface. The transfer characteristics were measured with Keithley Sourcemeter 2400 and Keithley Picoammeter 6487 in the nitrogen-filled glove box at room temperature. TCNE and F4-TCNQ was dissolved in chlorobenzene at a concentration of 1 mg/ml and spincoated onto rGO surface. The samples for TOF measurements comprised rGO layers deposited on fused silica. Coplanar Al contacts separated by 800 μm were thermally evaporated on these samples. The bias voltages applied to the samples were varied from -100 V to 100 V with a step of 25 V. The excitation source for TOF measurements was pulsed Nd:YAG laser of wavelength 210 nm with pulse duration of 3 ns. The displacement current of the charge carriers in the channel was recorded with a 2.5 GHz (LeCroy) oscilloscope. To detect very small currents corresponding to low electric fields, an amplifier was used (Miteq AM-1309). The molecular weight of 1-PSANa is 304.3. We have made the solution with 1 μg/ml. In order to have the solution to contain 1.3×10^{-10} moles/cm², we have dropcoated the 40 μl in each deposition. In the same way we have prepared the solutions of TCNE and F4-TCNQ and drop coated on to rGO surface. After each deposition, we have performed TOF measurements.

4.3 Results and Discussion

In Fig. 4.4, we compare transfer characteristics of rGO-based FETs without (black curve), and with 1-PSANa layer (red curve). The arrows indicate the direction of changing V_g that was swept in the range of ± 100 V. From the amount of hysteresis $\Delta V_H = 8$ V, for clean rGO and measured gate-oxide capacitance $C_{ox} = 6.25$ nF/cm², we

calculated from Eq. 3.1 the areal trap density $n_{tr} = 5.75 \times 10^{11} \text{ cm}^{-2}$. Upon deposition of 1-PSANA layer, V_{Dirac} shifted to 38 V. Using this value we calculated the density of trapped charges to be $2.7 \times 10^{12} \text{ cm}^{-2}$.

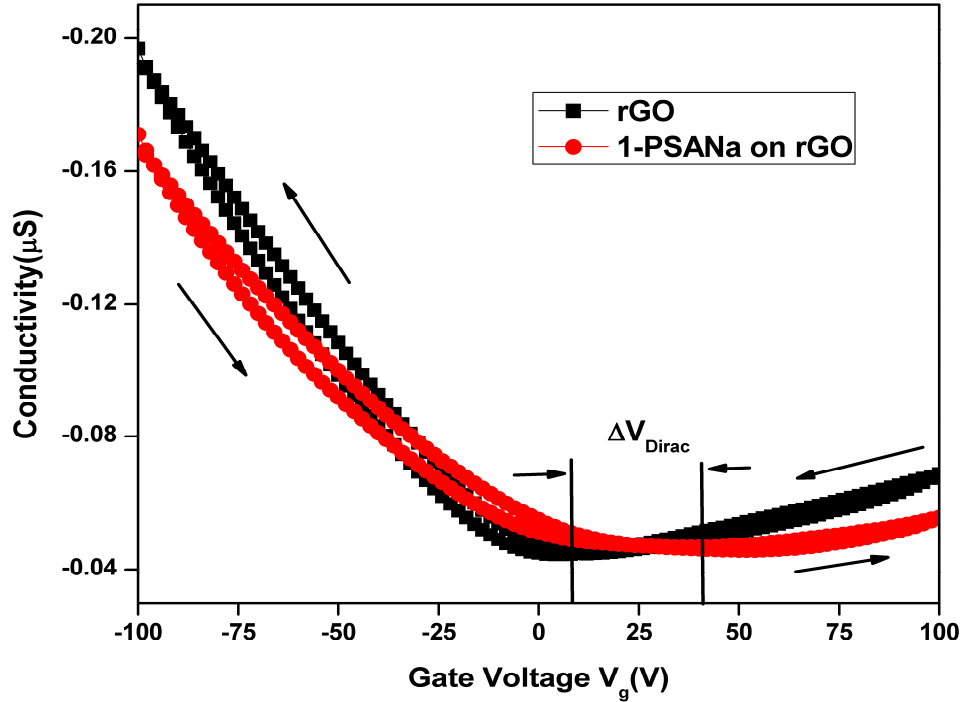


Figure 4.4: Normalized 2D conductivity as a function of gate voltage obtained in rGO-based FET without (black line) and with (red line) 1-pyrene sulfonic acid sodium salt. The arrows indicate the direction of the voltage sweep. ΔV_{Dirac} represent the change in the Dirac voltage upon deposition of 1-PSANa salt on rGO.

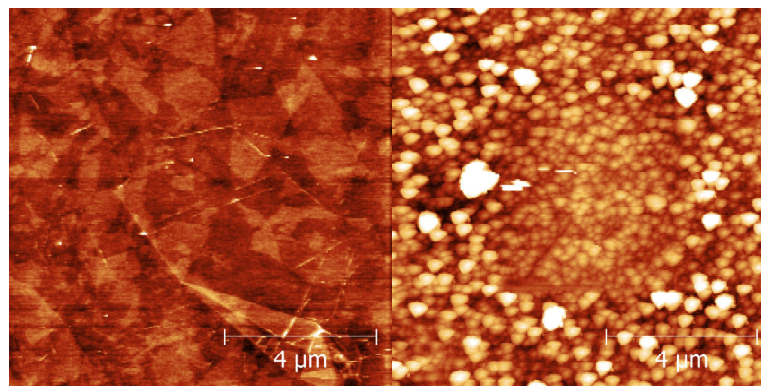


Figure 4.5: $10 \mu\text{m} \times 10 \mu\text{m}$ AFM image of rGO on Si/SiO₂ substrates without (left) and with 1-PSANa (right). The scale is 0 to 3 nm for rGO and with 1-PSANa is 0 to 100 nm.

AFM image of topography of rGO surface without and with 1-PSANa is shown in Fig. 4.5. The RMS roughness of the pristine rGO is 0.3 nm and with 1-PSANa it is increased to 20 nm. This is because 1-PSANa forms 3D islands with average size of $1\mu\text{m}^2$. The 1-PSANa layer was thick enough over all the surface and completely covered to ensure sufficient interface electron transfer to be detected by transport measurements. Somewhat lower charge transfer is expected for thick organic layers, as a result of intermolecular interactions.

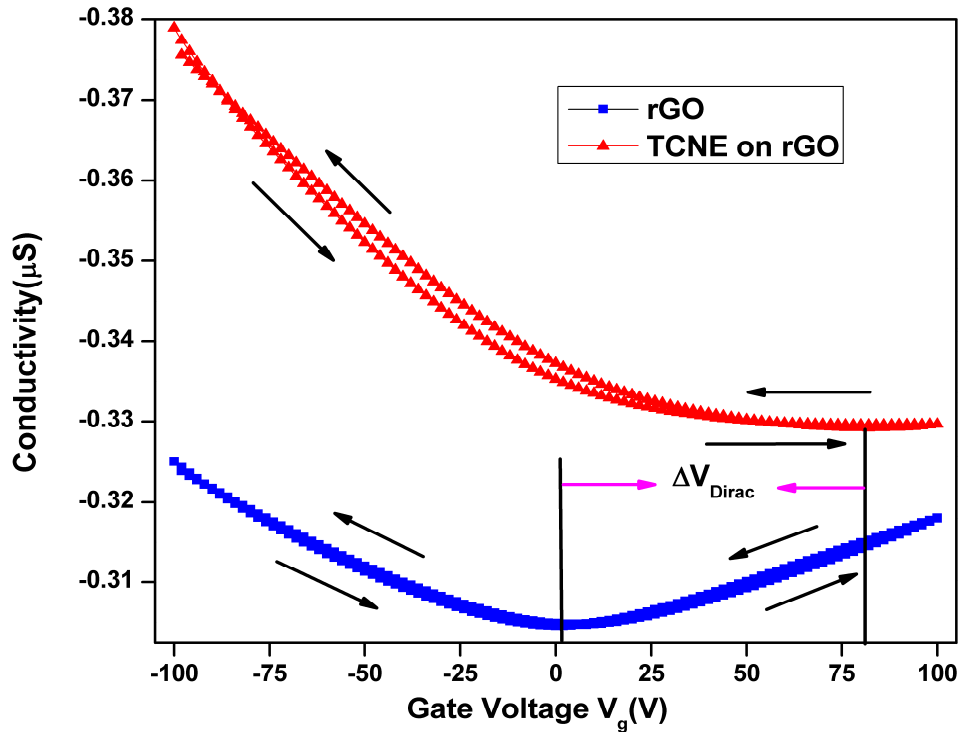


Figure 4.6: Normalized 2D conductivity as a function of gate voltage obtained in rGO-based FET without (blue curve) and with (red curve) TCNE. The arrows indicate the direction of the voltage sweep.

In Fig. 4.6 we compare the transfer characteristics of rGO-based FET without (blue curve) and with TCNE (red curve). For clean rGO $\Delta V_H=3\text{V}$, $n_{tr}=2.15\times 10^{11}\text{ cm}^{-2}$, and increases to 80 V, $5.94\times 10^{12}\text{ cm}^{-2}$ respectively upon the deposition of TCNE. In Fig. 4.7 we compare the transfer characteristics of rGO-based FET without (black curve) and with F4-TCNQ (red curve). For clean rGO $\Delta V_H=2\text{ V}$ and $n_{tr}=0.78\times 10^{11}\text{ cm}^{-2}$ increases to 93 V and $n_{tr}=3.6\times 10^{12}\text{ cm}^{-2}$

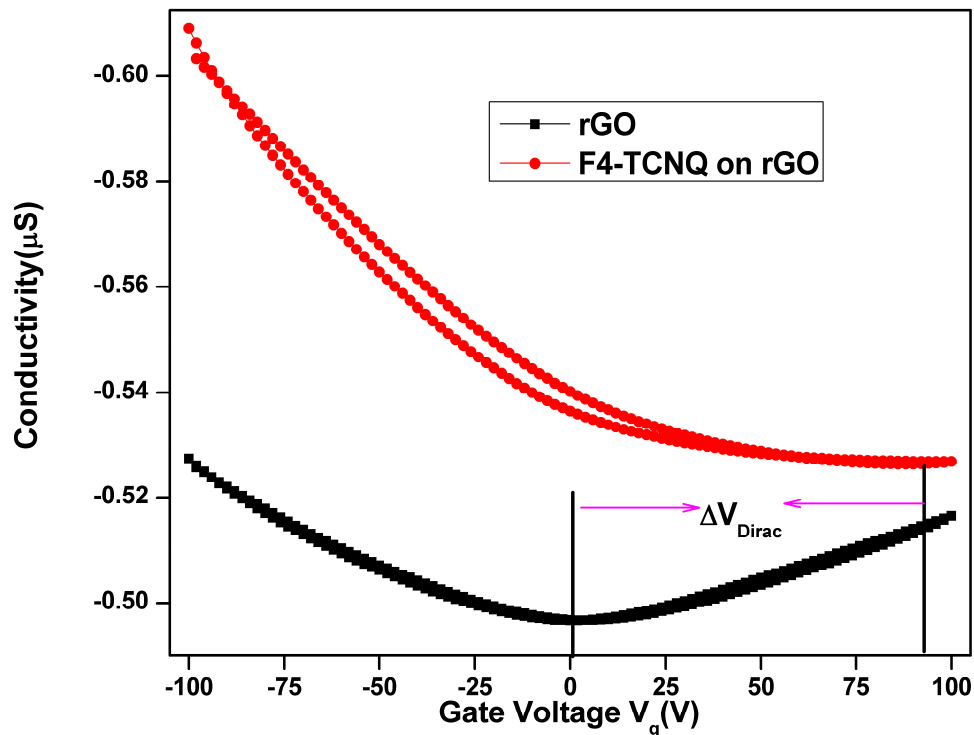


Figure 4.7: Normalized 2D conductivity as a function of gate voltage obtained in rGO-based FET without (red half filled squares) and with (blue filled squares) F4-TCNQ. The arrows indicate the direction of the voltage sweep.

respectively upon the deposition of F4-TCNQ. Comparing the transfer characteristics of rGO with 1-PSANa, F4-TCNQ, TCNE, all these three materials shows the efficient p-type doping, and the electron mobility of is not completely suppressed with 1-PSANa on rGO relative to TCNE and F4-TCNQ. But in case of F4-TCNQ and TCNE, there is a large shift in the V_{Dirac} compared to 1-PSANa, and the electron mobility is completely quenched, since both of them are strong electron acceptors. The cyano-groups (CN) present in TCNE and F4-TCNQ which are acting as electron with-drawing groups are responsible for efficient p-type doping.

The effect of these three electron acceptors on TOF photocurrent measurements on rGO at a concentration of 1.3×10^{-10} moles/cm² for four depositions is presented in the following. In Fig. 4.8, we have presented the TOF photocurrent measurements on rGO with 1-PSANa on top of it for the applied bias of -25 V. For clean rGO (filled circles), we see a monotonous decrease of photocurrent, followed by a rapid decrease of the photocurrent. Transit time is determined from the intersection of the asymptotes drawn to the constant current plateau and the long tail.

After the first deposition of 1-PSANa, the transit time increases (half filled circles). For subsequent deposition of 1-PSANa the transit time increases upto first three depositions and then it starts to decrease. The electron charge transfer from rGO to 1-PSANa, leaves holes in rGO. The increase of the transit time is an indication that the mobility of the carriers is reduced, most likely due to recombination with the localized holes in rGO that emerge from the electron transfer from rGO to 1-PSANa molecules. Due to charge transfer of electrons from rGO, 1-PSANa molecules are

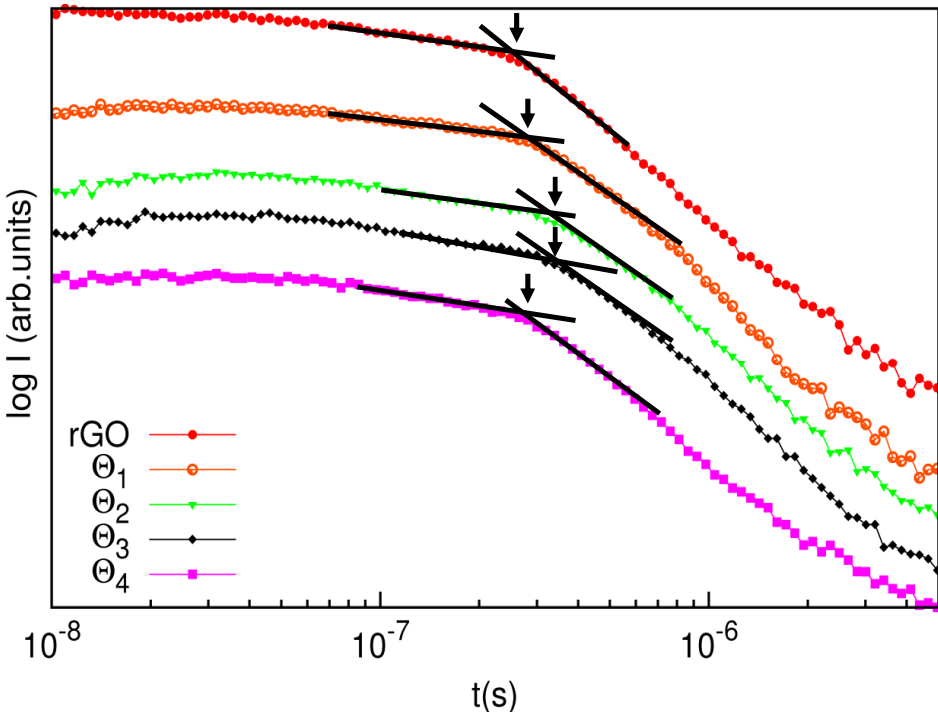


Figure 4.8: Double logarithmic plot of photocurrent vs time. The effect of 1-PSANa on the transient response of rGO after each deposition for a bias voltage of -25 V at a wavelength of 210 nm. The arrow indicates the transit time. These curves are artificially shifted from one over another. Θ_1 , Θ_2 , Θ_3 , Θ_4 represent the 1st, 2nd, 3rd, 4th depositions.

negatively charged. As we increase the surface coverage, the intermolecular interaction between these negatively charged ions becomes strong. Hence the transfer of electrons from rGO to 1-PSANa also decreases with increasing the coverage. However, due to more 1-PSANa molecules per unit surface area, the overall charge transfer from graphene to the 1-PSANa molecules is efficient compared to the dilute case. With further increasing the coverage, the interaction between the negatively

charged molecules becomes too strong and the charge transfer is poor compared to the less coverage hence the overall charge transfer from rGO to 1-PSANa is less efficient. This is in good agreement with the theoretical calculations [162]. There is no appreciable effect on the hole transport as shown in Fig. 4.9.

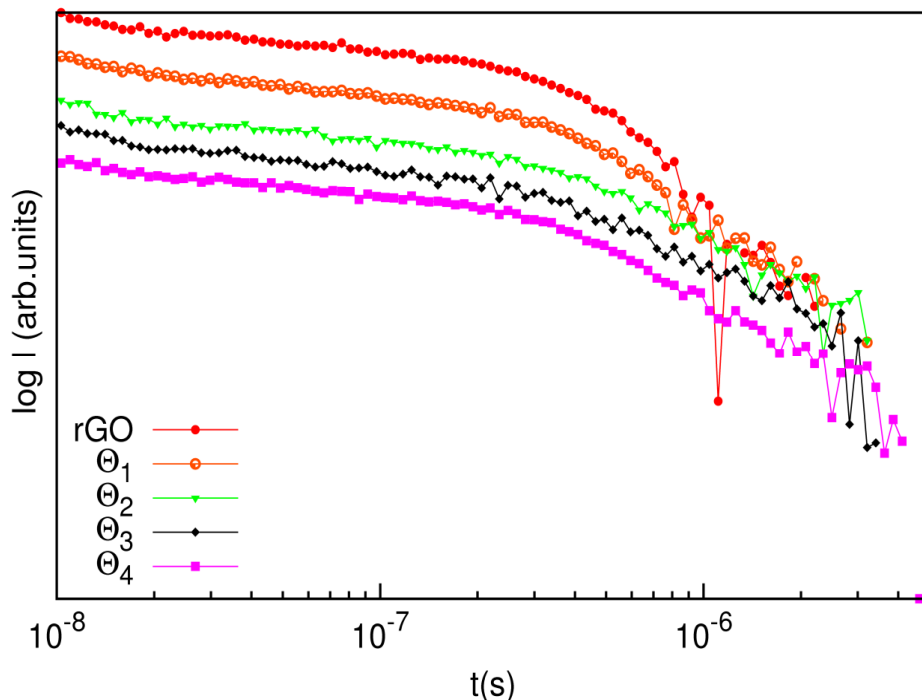


Figure 4.9: Double logarithmic plot of photocurrent vs time. The effect of 1-PSANa on the transient response of rGO after each deposition for a bias voltage of +25 V at a wavelength of 210 nm. These curves are artificially shifted from one over another. Θ_1 , Θ_2 , Θ_3 , Θ_4 represent the 1st, 2nd, 3rd, 4th depositions.

Fig. 4.10 summarizes the data for the transit time for all coverages for different voltages. The amount of increase in the transit time is more pronounced at lower voltages than at higher voltages. This is because at lower voltages the velocity of the carriers is lower, and results in higher probability for these carriers to be captured into the trap states that emerge from electron transfer from rGO to 1-PSANa. As the bias voltage increases, the velocity of the carriers also increases; hence the probability for these carriers to be captured into the trap states and the recombination sites is reduced. At higher coverages the transit time starts to drop again for all voltages.

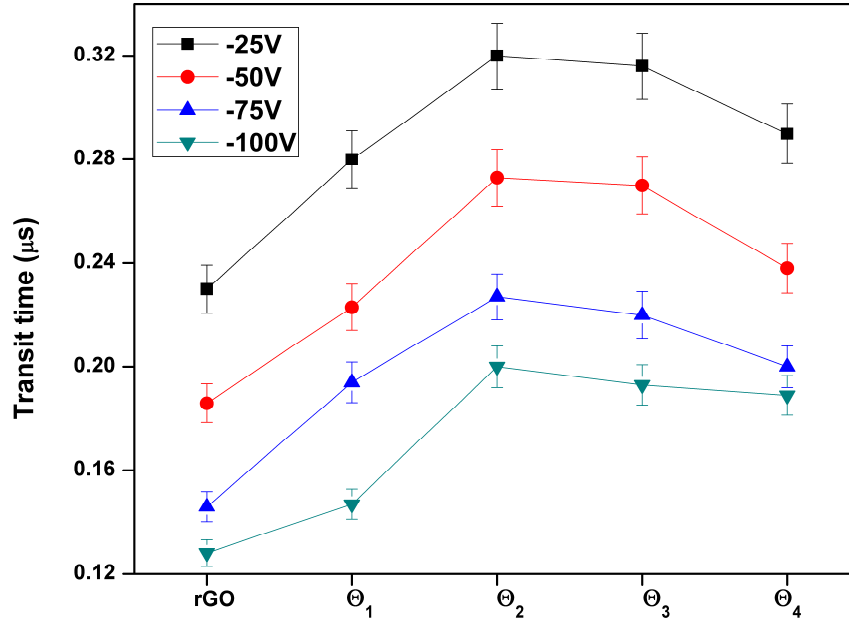


Figure 4.10: Variation of transit time for each deposition of 1-PSANa for different voltages.

The TOF measurements on rGO with four subsequent depositions of TCNE are presented in Fig. 4.11 for an applied bias voltage of -25 V. Transit time was determined from the intersection of the asymptotes drawn to the plateau and tail. For pristine rGO, the photocurrent is monotonically decreasing and a sharp drop of the photocurrent was observed (filled circles) exhibiting a transit time at 2.8×10^{-7} s. A fast decay of the photocurrent observed after the transit time is an indication of relatively low concentration of traps that would immobilize the charge carriers for times that are substantially longer than the transit time of an average carrier. After the first deposition of TCNE (half filled circles) the transit time is shifted from 2.8×10^{-7} s to 6×10^{-7} s, which implies that the electron mobility has decreased to more than half of the previous value using the constant field approximation. In addition to the shift of the transit time to longer times, the change in the shape of the TOF curve is observed. The decay in the photocurrent is due to the recombination of the electrons with the localized holes that emerge from charge transfer from rGO into TCNE. The rGO sheets consists of nanometer-size perfectly reduced graphene, with some residues of GO, and carboxyl groups, which results in hopping conduction as the possible charge-transport mechanism [199]. When the adsorbate is present on the surface of rGO, it will affect the conductive path of the some of the charge carriers. The surface coverage of TCNE after the first deposition is 1% of graphene [162].

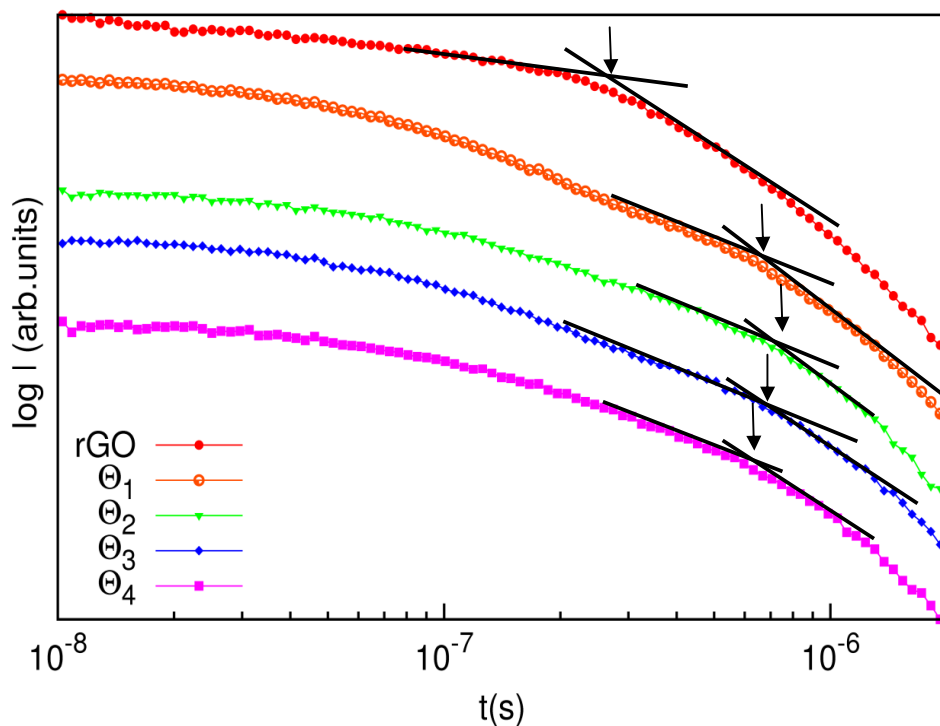


Figure 4.11: Double logarithmic plot of photocurrent vs time. The effect of TCNE on the transient response of rGO after each deposition for a bias voltage of -25 V at a wavelength of 210 nm. The arrow indicates the transit time. These curves are artificially shifted from one over another. Θ_1 , Θ_2 , Θ_3 , Θ_4 represent the 1st, 2nd, 3rd, 4th depositions.

The TCNE molecules on the surface of rGO affect the hopping of charge carriers between the localized sites. Hence the transit time increases and the determination of the transit time is unreliable and shifted to longer times. With further increasing the coverage, kink completely disappears and the determination of the transit time is more unreliable. In case of 1-PSANa on rGO, the transit time increases, since it is a weak electron acceptor. But with TCNE on rGO, which is a strong electron acceptor; monotonous decay of photocurrent is also observed and determination of the transit times is less obvious in this case. After the second deposition the transit time again increased to 7.5×10^{-7} s and then decreased after third and fourth deposition. The behavior can be understood from the theoretical calculations of Y.H. Lu *et al.* [162]. At very low coverages (dilute case) the charge transfer between graphene and TCNE is strong and the amount of transfer is estimated as 0.44 e per each TCNE molecule. As TCNE molecules acquire electrons from graphene, they are negatively charged

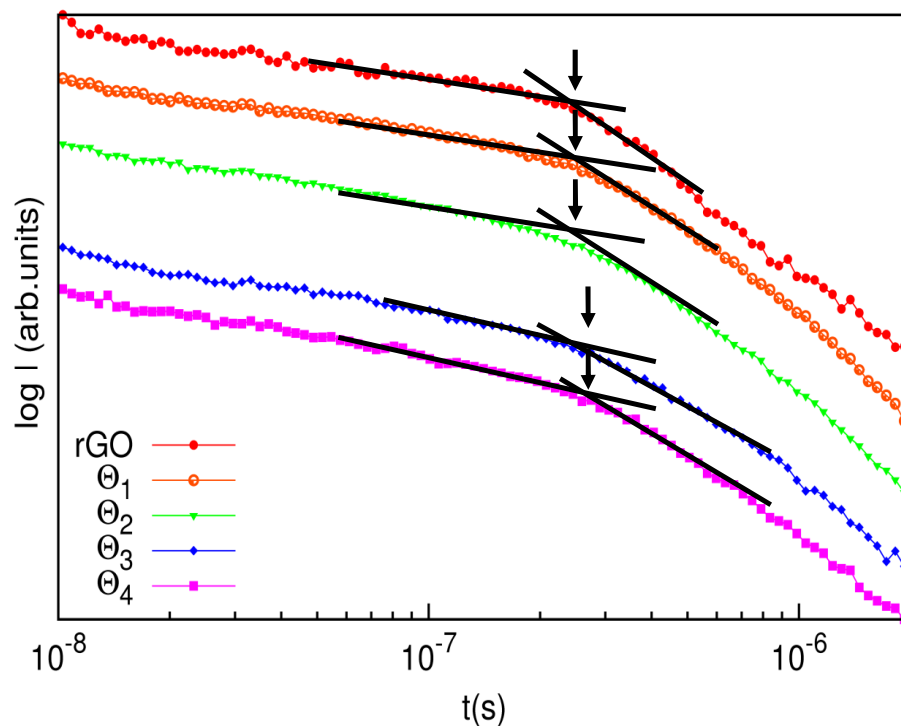


Figure 4.12: Double logarithmic plot of photocurrent vs time. The effect of TCNE on the transient response of rGO after each deposition for a bias voltage of +25 V at a wavelength of 210 nm. These curves are artificially shifted from one over another and Θ_1 , Θ_2 , Θ_3 , Θ_4 represent the 1st, 2nd, 3rd, 4th depositions.

and start to interact with each other as the coverage is increased. As the interaction between them increases, the charge transfer between the graphene to TCNE is also reduces to 0.2e per each TCNE molecule. However, as the number of TCNE molecules per unit surface area increases, the overall charge transfers from graphene to the TCNE molecules increases. If the interaction between molecules is too strong, the amount of charge transfer may be insufficient to produce efficient p-doping [162]. Since as the surface coverage increases, the interaction between the negatively charged ions increases and the interaction between TCNE and rGO decreases, as well as the charge transfer. We see that there is no effect of TCNE on hole transport as shown in Fig. 4.12, since it is an electron acceptor and due to charge transfer between TCNE and rGO leaves holes in rGO, which will act as traps for electrons but not for holes.

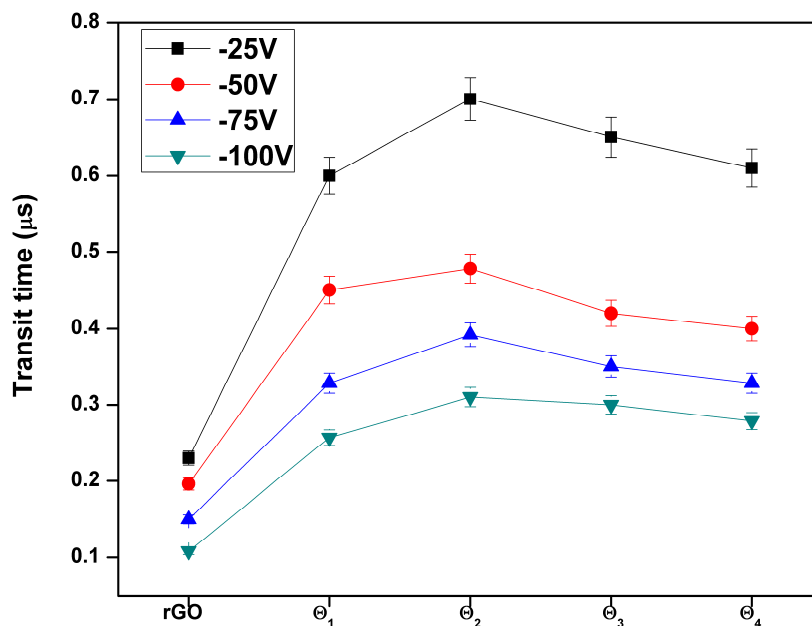


Figure 4.13: Variation of transit time for each deposition of TCNE for different voltages.

Fig. 4.13 summarizes the data for the transit time for all coverages of TCNE. The variation of the transit time is more pronounced at lower coverages than at higher coverages. At higher coverages the transit time starts to drop again for all voltages. The trend of variation of the transit time is similar to the 1-PSANa on rGO surface. From these measurements it is evident that the capture probability for the charge carriers into trapping sites and recombination sites at higher voltages is low, since at high voltages the velocity of the carriers is high. At lower voltages, the probability for these carriers to capture into these sites is high, since the carrier velocity is low. But the amount of increase of transit time in this case is relatively high compared to 1-PSANa on rGO.

The TOF measurements on rGO for -25 V for different coverages of F4-TCNQ are shown in Fig. 4.14. Focusing on the $I(t)$ curve for a clean rGO (filled circles), we see a monotonous decrease of photocurrent followed by a rapid decrease of photocurrent. After the first deposition of F4-TCNQ, we see that the monotonic decay of the photocurrent is observed (half filled circles) and also exhibits a long, slowly decaying tail and a slight increase in transit time. The initial surge of the photocurrent corresponds to the holes that move towards the biased electrode in the high field region. The initial surge of photocurrent doesn't change for all depositions

and the amount of photocurrent generated for all the depositions is same. After the electron-hole pairs are separated with the applied electric field, the electrons starts to move towards the opposite electrode. But during the electron charge transport

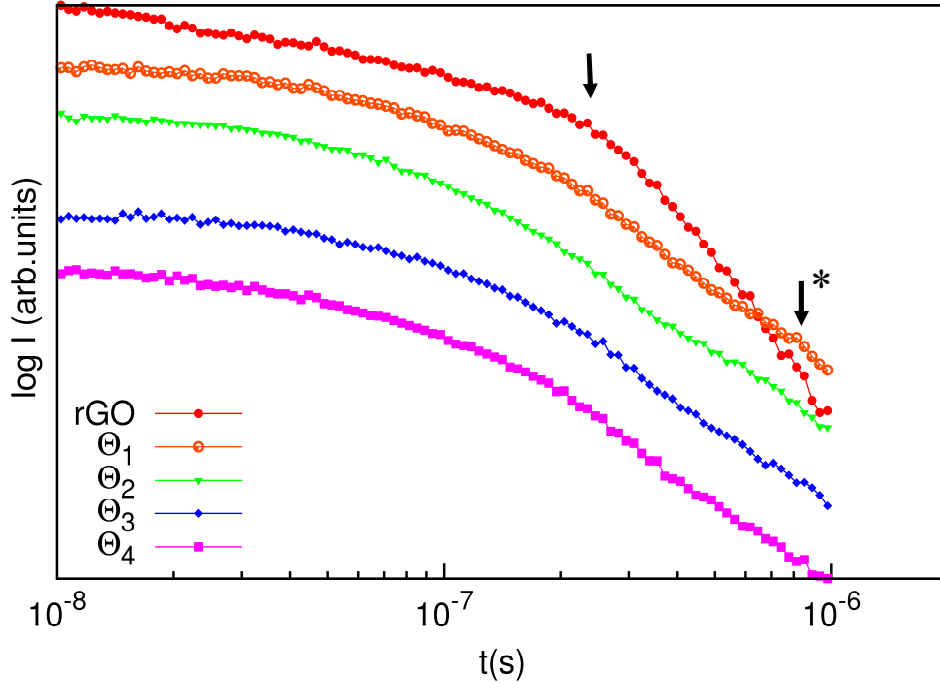


Figure 4.14: Double logarithmic plot of photocurrent vs time. The effect of F4-TCNQ on the transient response of rGO for the applied bias of -25 V at a wavelength of 210 nm. These curves are artificially shifted from one over another. Θ_1 , Θ_2 , Θ_3 , Θ_4 represent the 1st, 2nd, 3rd, 4th depositions.

towards the opposite electrode under the influence of the applied bias, the electrons are recombined with the localized holes, which result from the charge transfer between rGO and F4-TCNQ. Hence the decay in the photocurrent is observed. Since F4-TCNQ is a strong electron acceptor, it leaves a hole in rGO after the charge transfer. The F4-TCNQ molecules on the surface of rGO affect the hopping of charge carriers between the localized sites. After the first deposition the kink signaling the arrival of the fastest carriers is barely visible on the $I(t)$ curve, as indicated by the asterisk. For higher coverages, the electron-hole recombination rate increases, masking thereby the appearance of the kink in $I(t)$ curves. We see that there is no clear signature for the electrons to reach the opposite electrode. This is further evidenced by the presence of long tail, which indicates the presence of trap states that

immobilize the charge carriers for longer times. This behavior remains the same for all depositions. This is due to strong interaction between rGO and F4-TCNQ. The TOF measurements on rGO for +25 V for different coverages of F4-TCNQ are shown in Fig. 4.15. We can clearly observe that there is no effect on the hole transport irrespective of the surface coverage, as there is no change in the transit time which is indicated by the arrows.

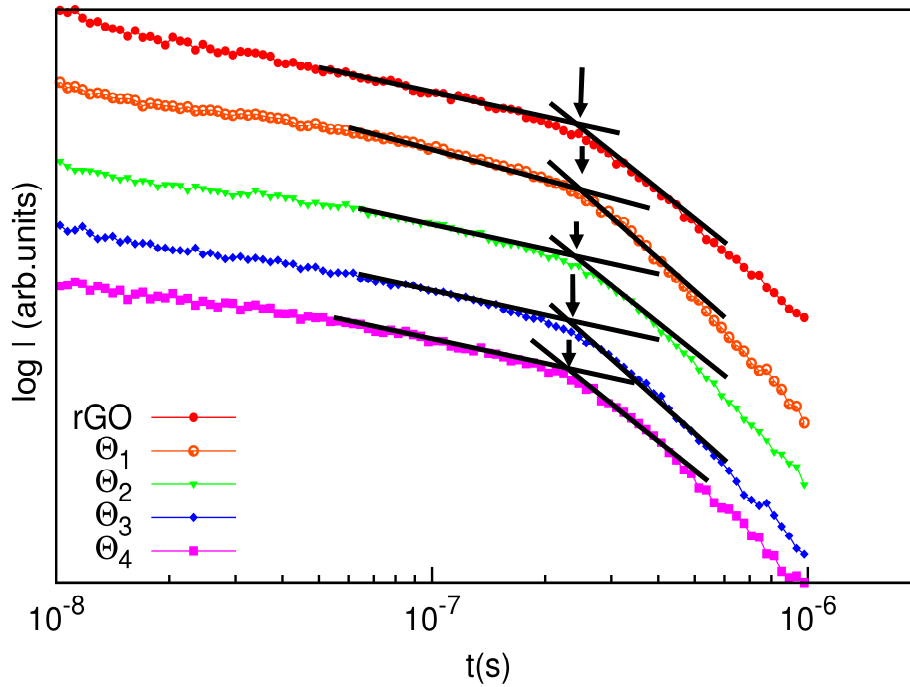


Figure 4.15: Double logarithmic plot of photocurrent vs time. The effect of F4-TCNQ on the transient response of rGO for the applied bias of +25 V at a wavelength of 210 nm. These curves are artificially shifted from one over another. Θ_1 , Θ_2 , Θ_3 , Θ_4 represent the 1st, 2nd, 3rd, 4th depositions.

In summary among 1-PSANa, TCNE, F4-TCNQ materials, F4-TCNQ and TCNE exhibited pronounced effect on electron charge transport in rGO compared to 1-PSANa as revealed by the transfer characteristics and TOF measurements. 1-PSANa on rGO increases the transit time, but the shape of the $I(t)$ curves doesn't change, but with TCNE on rGO, the transit time increases, and the photocurrent starts to drop, thus effecting the shape of the TOF signal. With F4-TCNQ on top of rGO the amount photocurrent decreases, and the determination of the transit time is completely unreliable. The summary of the effect of adsorbates are presented in

Table 5.1.

Adsorbate	Effect on Dirac voltage	Electron mobility	Hole mobility	TOF mobility
1-pyrene butyric acid (PBA)	Shifted to +V	Decreases	Decreases	Electron mobility decreases
1-pyrene sulfonic acid sodium salt (1-PSANa)	Shifted to +V	Decreases	Remains unchanged	Electron mobility decreases
Tetrathiafulvalene (TTF)	Shifted to -V voltages	Slightly increases	Decreases	Hole mobility decreases
Tetracyanoethylene (TCNE)	Shifted to +V	Diminishes	Slightly increases	Electron mobility decreases
Tetrafluoro-tetracyanoquinodimethane (F4-TCNQ)	Shifted to +V	Diminishes	Slightly increases	Electron mobility decreases

Table 5.1: Summary of the effect of adsorbates on rGO surface.

4.4 Conclusions

In summary, we have studied the effect of three electron acceptors 1-PSANa, which is a weak electron acceptor and TCNE, F4-TCNQ, which are strong electron acceptors by rGO based FETs and by the TOF technique. In rGO FETs conductivity minimum shifts to positive gate voltages for all materials and the electron mobility is completely suppressed with F4-TCNQ and TCNE. We have performed TOF measurements by adding 1.3×10^{-10} moles/cm² of these molecules in each deposition. The effect of 1-PSANa on rGO shows dependence on the surface

coverage and the applied electric field. With increasing the concentration of 1-PSANa, the electron mobility drops and then recovered at higher coverages. The effect of TCNE is significant, in changing the transit time to longer times and changing the shape of the TOF signal. The electron mobility drops with increasing the coverage due to the charge transfer and then recovers due to intermolecular interaction of negatively charged TCNE molecules. The change in the electron mobility is due to recombination of the electrons with the localized holes that leaves in rGO due to the charge transfer from rGO to the adsorbates. The electron photocurrent decreases monotonically with adlayers of F4-TCNQ, but the effect is not depending on the increasing coverage and the determination of the transit time is completely unreliable, due to strong interaction between the adsorbates and rGO.

Chapter 5: Electric charge transport in blends between graphene nanoflakes and organic semiconductors

High field-effect mobility, stability, and solution processability of organic materials raises interest in using them as active materials in FETs. But their mobility is limited by the rate of hopping in the disordered regions of such films. Here we have used graphene nanoflakes (GNs) instead of CNTs to enhance the mobility of OSs, which has large conduction channel compared to CNTs and it can be soluble in organic solvents [173].

In this chapter we present the study of electric charge transport properties of graphene and OSs blend mixtures of both p-type and n-type materials. The aim of the study is to explore the possibility of improving charge carrier mobility in OSs by mixing with GNs. We have used TOF and FET-based measurements to assess their transport properties. We have explored P3HT and PDIF-CN2 as two representatives of p-type and n-type OSs respectively.

5.1 Graphene/P3HT blends

Solution processed OFETs suffer from low mobility, but they have high I_{on}/I_{off} ratio. GFETs have high mobility, but suffer from low I_{on}/I_{off} ratio. With the aim of improving the mobility in OSs we have examined transport of the blends of OSs and GNs. There have been few attempts to improve the mobility of organic semiconductors based on carbon nanotubes (CNTs) by inserting into or beneath the organic semiconducting layer [168-172]. These studies suggest that the CNTs will act as conducting bridges between the polycrystalline regions of the organic layer. But as the mobility increases, I_{on}/I_{off} ratio starts to decrease. This could be because at higher concentrations the charge carriers start to percolate through the CNTs, thus limiting the maximum mobility achievable, before reaching the percolation threshold. In FET's channel using graphene, which is 2D material would improve charge carrier mobility relative to CNT, which is 1D material. Schematic representation of the side

view of organic semiconductor/graphene hybrid FET is as shown in Fig. 5.1. GNs were introduced into the OS matrix.

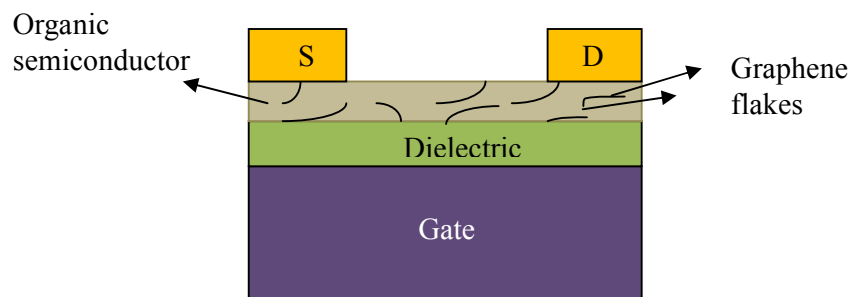


Figure 5.1: Schematic representation of side view of organic semiconductor/graphene hybrid FET [173].

5.1.1 Experimental

Orthodichlorobenzene (ODCB) is a good solvent for both GNs and most of the OSs. Graphite was added into ODCB at a concentration of 6 mg/ml. The mixture was sonicated with an ultrasonicator at 100 Watt power for 15 min. After sonication the thick graphite flakes were allowed to settle at the bottom of the vessel for 24 h. Then the remaining solution was transferred to another bottle and centrifuged at 1500 rpm for 1 h. The top portion of the supernatant contains single- and few-layer graphene flakes. 4 mg of P3HT was added to this solution. The mixture was then ultrasonicated and heated to 80 °C and then slowly cooled down to room temperature. A heavily-doped silicon wafer with 300 nm thermally grown SiO₂ was used as a substrate material. The substrates were cleaned by sonication in acetone, isopropanol and deionized (DI) water, followed by N₂ drying. The blend of P3HT/GNs (GN:P3HT) was spin-coated onto the substrates at a speed of 1000 rpm for 1 minute. The gold source and drain electrodes were deposited by thermal evaporation through a shadow mask resulting in a channel length of 100 μm and a width of 0.5 cm. The resulting transistors were annealed at 90 °C for 15 min. All the solutions were prepared and tested under the nitrogen-filled glove box at room temperature.

Optical methods were used for the estimation of the concentration of the GNs in the solution. From the absorbance of GNs of known concentration, the concentration of the GNs of unknown concentration can be estimated. Here we have

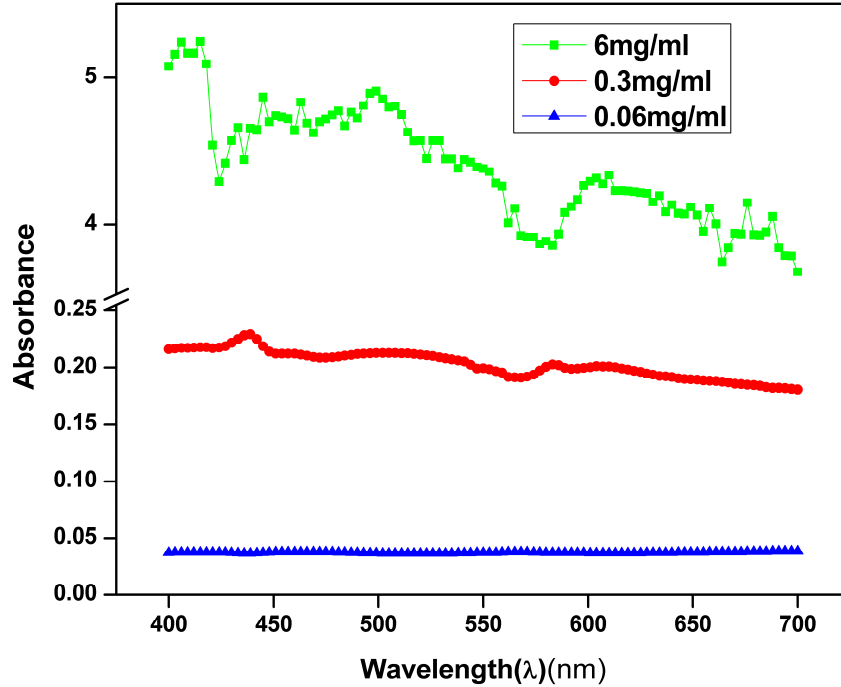


Figure 5.2: Absorption spectra of graphene dispersions.

used 660 nm as the reference wavelength [46]. The absorbance spectra of GNs dispersion in ODCB having different concentrations are shown in Fig. 5.2. The absorbance spectrum of GNs with concentration of 6 mg/ml is measured and the absorbance was noted down at 660 nm wavelength from the topmost curve. Then the solution of an unknown concentration of GNs is measured and from the absorbance at 660 nm, the concentration was deducted (red curve). In order to study the dependence of the concentration of GNs, solutions were made in the same way as explained above and then removed some of the ODCB by heating in the nitrogen ambient above boiling point of the solvent (200 °C). These GNs solutions were mixed with P3HT in the same way as explained before. We have observed that at higher concentrations, GNs will start to aggregate and start to separate from ODCB and tend to precipitate at the bottom of the container. This can be partially avoided by ultrasonication.

5.1.2 Results and Discussion

In Fig. 5.3 we compare the transfer characteristics of FETs of P3HT (bottom curve) and GN:P3HT (top curve) in the saturation regime at $V_{ds}=-80$ V on a semilogarithmic scale at GNs concentration of 0.06 mg/ml. The I_{on} and I_{off} currents

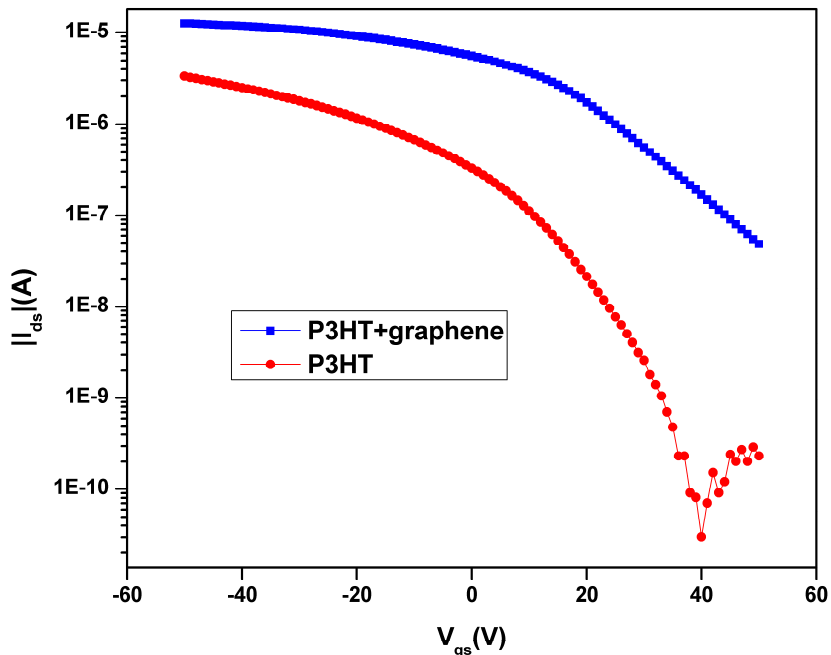


Figure 5.3: Comparison of the transfer characteristics of FETs of P3HT and GN:P3HT at constant $V_{ds} = -80$ V on a semilogarithmic scale at GNs concentration of 0.06 mg/ml.

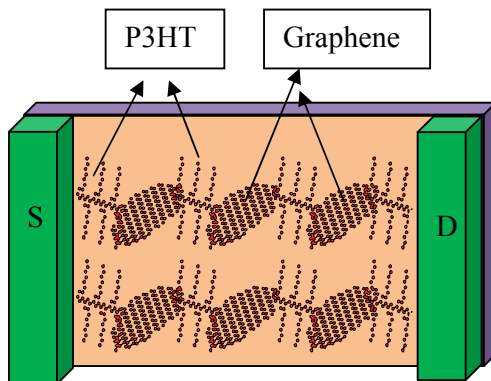


Figure 5.4 Schematic representation of top view of organic semiconductor/graphene hybrid FET.

are measured at $V_{gs} = -50$ V and $+50$ V in order to estimate the I_{on}/I_{off} ratio. I_{on} shows a factor of 7 increase compared to pristine P3HT-based FETs and I_{off} shows an improvement by almost two orders of magnitude. Hence the I_{on}/I_{off} ratio decreased by an order of magnitude. The mobility increased from 0.003 cm^2/Vs to 0.02 cm^2/Vs . The improvement in the mobility is due to incorporation of GNs into OS film. GNs form a high-mobility network within the P3HT matrix. As the charge carriers

encounter these regions their transport becomes band-like, which effectively increases their overall mobility. Schematic representation of top view of organic semiconductor/graphene hybrid FET is shown in Fig. 5.4. The charge carriers flowing from source to drain electrode take advantage of flowing partially through GNs and partially through P3HT. Thus, travelling only a fraction of distance within GN:P3HT-based FET compared to pristine P3HT-based FET, leads to an effective channel length reduction.

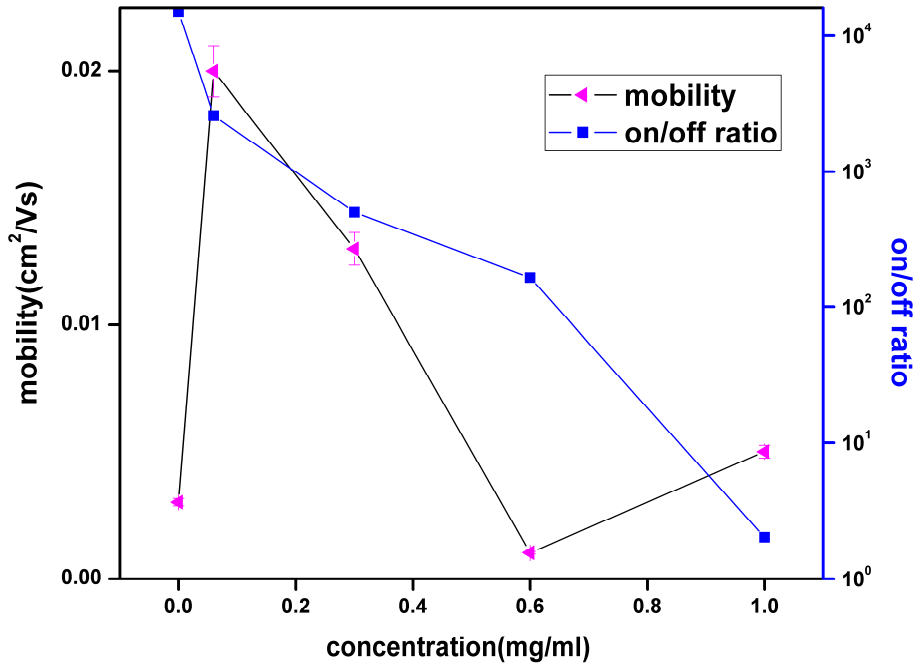


Figure 5.5: Comparison of the mobility and I_{on}/I_{off} ratio of GN:P3HT-based FETs as a function of GNs concentration.

Fig. 5.5 represents the summary of the maximum mobilities and I_{on}/I_{off} ratios of all GN:P3HT-based FETs with increasing concentration of GNs. A maximum mobility of $0.02 \text{ cm}^2/\text{Vs}$ is observed at a concentration of 0.06 mg/ml of GNs, below this concentration no improvement in the mobility is observed. One of the reasons for a decrease in the mobility can be understood from the energy level alignment of P3HT and graphene. Schematic energy level diagram of GN:P3HT is shown in Fig. 5.6. Graphene has a workfunction of 4.56 eV [189] and P3HT has HOMO of -5.1 eV [175], hence there is a potential barrier of 0.54 eV for injection of holes from P3HT into GNs, and the contact resistance exists due to the misalignment of the energy levels. As the number of interconnecting junctions increase, the contact

resistance dominates the channel resistance which results in reduction of the mobility [207,208]. The I_{on}/I_{off} ratio decreases with increasing the concentration of GNs and it drops to 2 at a concentration of 1 mg/ml reaching the graphene I_{on}/I_{off} ratio as shown in Fig. 5.5.

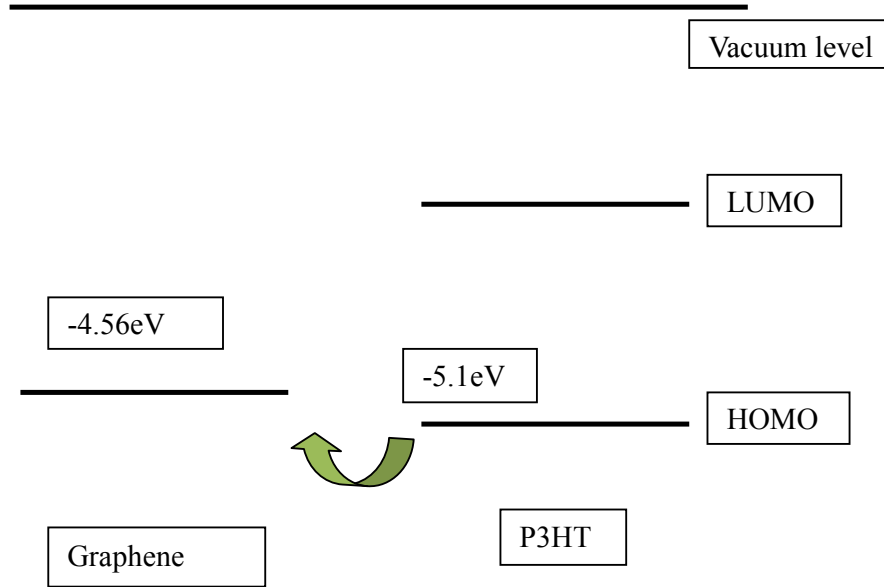


Figure 5.6: Schematic energy level diagram of GN:P3HT.

These GNs can form percolation and non-percolation networks. When the separation between the GNs is sufficiently small, the charge carriers can percolate from one flake to another. If the separation between the GNs is large enough, the charge carriers upon leaving a GN into one of the localized states in P3HT where less efficient transport, hopping takes place. The percolation networks increases the I_{off} , since graphene is zero gap semiconductor we can't switch off the current. On the other hand the non-percolation networks contribute to the I_{on} . The onset of I_{off} current represents that the formation of few percolation networks. The charge on the non-percolating networks that fall on the dielectric surface can be tuned via the gate, forming a thin channel for the charge carriers that connect P3HT grains. Carriers move largely within the highly conducting semimetallic graphene networks. Only occasionally, and for distances short compared to the source-to-drain (s-d) separation they can travel through the P3HT channel. This represents an effective shortening of the s-d distance, giving rise to an equivalent increase in the transconductance. As the concentration of GNs increases the separation between them decreases, which raises the I_{off} current, consequently the I_{on}/I_{off} ratio drops [171].

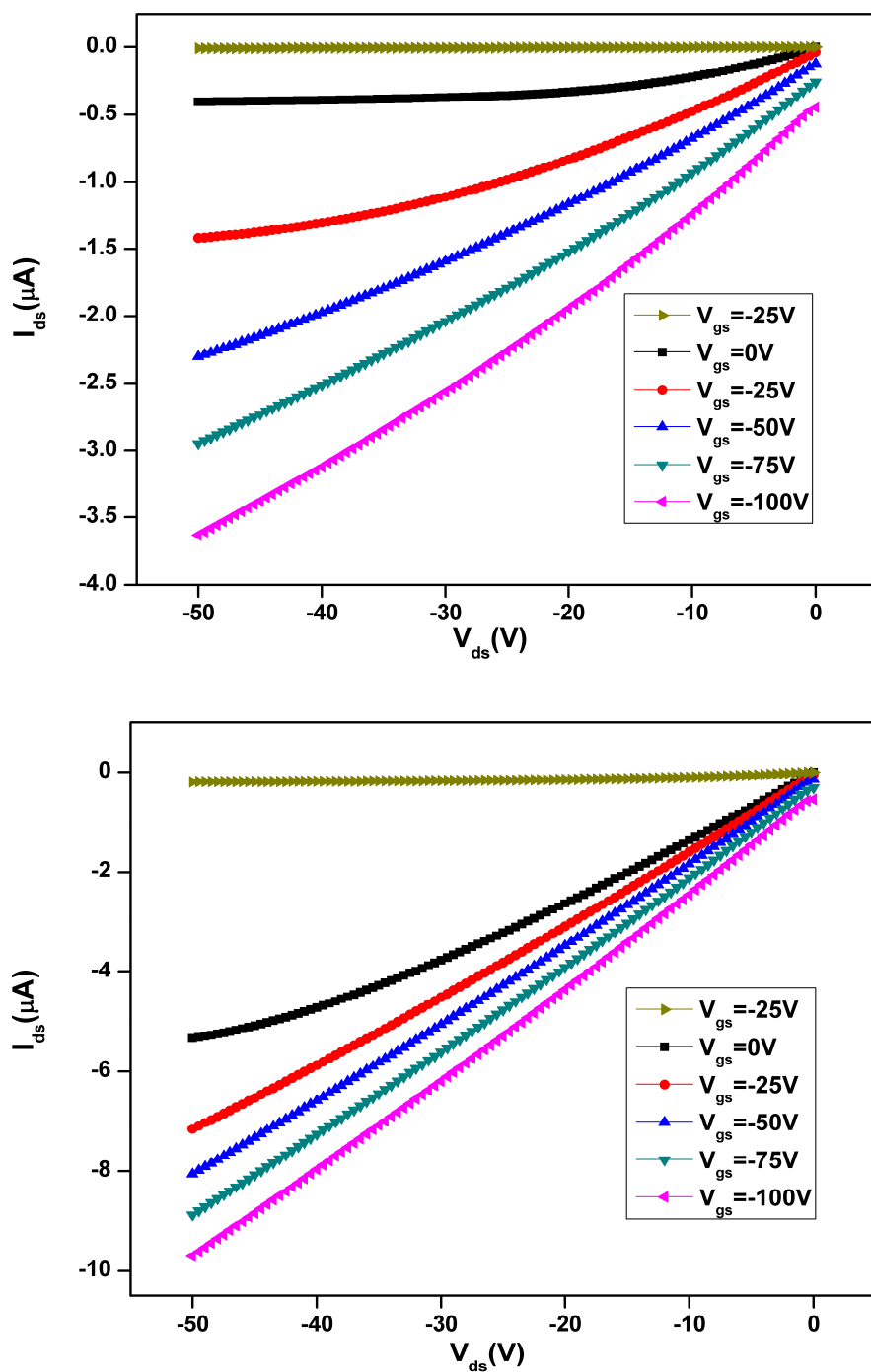


Figure 5.7: Output characteristics of P3HT-based FETs (top) and GN:P3HT-based FETs (bottom) at different gate voltages.

The output characteristics of P3HT-based FETs (top) and GN:P3HT-based FETs (bottom) are presented in Fig. 5.7. In pristine P3HT the current increases

linearly with increasing gate voltage, whereas in GN:P3HT the gate modulation shows graphene-like behavior with poor gate modulation when the FET is on state, which is a good evidence for the transport on the network of GNs.

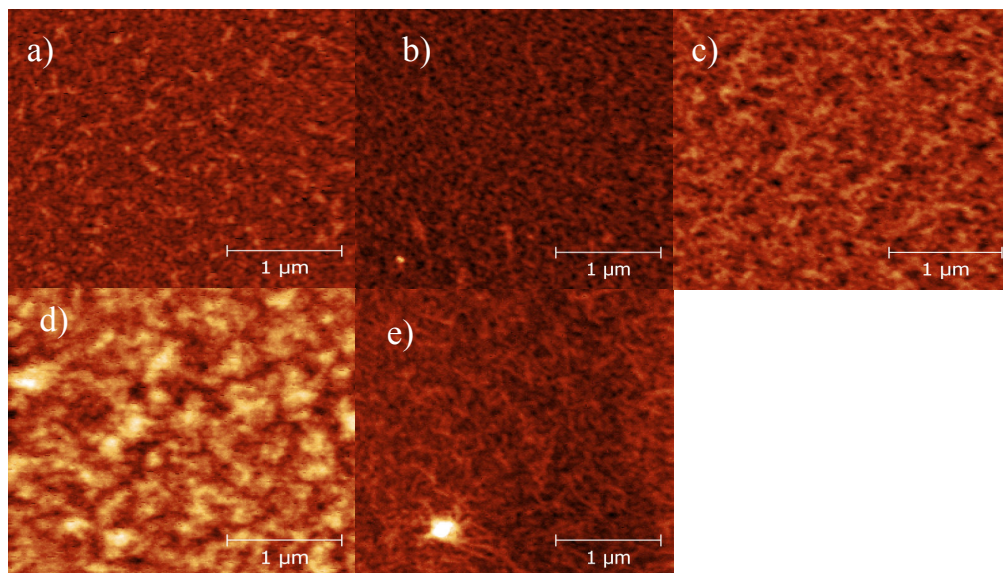


Figure 5.8: $3\mu\text{m}\times 3\mu\text{m}$ AFM images of GN:P3HT blends for concentrations of 0, 0.06, 0.3, 0.6, 1 mg/ml of GNs respectively. The height scale is same for all the images and it is 0 to 20 nm.

The morphology of GN:P3HT layers is shown in Fig. 5.8 for different concentrations of GNs. We see that the mobility and $I_{\text{on}}/I_{\text{off}}$ ratio decreased suddenly at 0.6 mg/ml concentration of GNs. We can observe at the GNs concentration of 0.6 mg/ml, the morphology is different as shown in Fig. 5.8(d). The morphology shows the presence of some pits and formation of non-uniform grains. This is due to GNs disrupts the molecular ordering of P3HT molecules. At 1 mg/ml concentration the GNs they are started to agglomerate in some regions as shown in Fig. 5.8(e).

5.2 Graphene/PDIF-CN2 blends

Functionalized perylenes have recently attracted considerable attention, since they combine high n-type mobility, coupled to ambient stability and solution processability. Solution processing of these materials in organic media makes them suitable for blending with graphene flakes, aiming at exploiting the exceptional

charge transport characteristics of this novel 2D material. Such a bi-component material may be a good candidate for high speed organic electronics as well as for light-harvesting applications. PDIF-CN2 [176] has gained increased interest mostly because reported band-like electron transport in PDIF-CN2 single crystals, exhibiting electron mobilities as high as $6 \text{ cm}^2/\text{Vs}$. Also, relatively high electron mobility and high $I_{\text{on}}/I_{\text{off}}$ ratios were reported in PDIF-CN2 thin-film-based FETs [176,177].

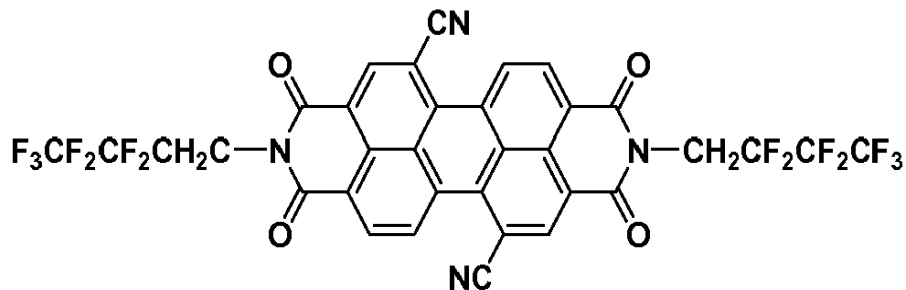


Figure 5.9: Molecular structure of N,N'-bis(perfluorobutyl)-2,6-dicyanoperylene-3,9-dicarboxylic diimide (PDIF-CN2).

FETs fabricated from solution processed perylenediimides suffer from disorder-induced trap states that effectively reduce charge carrier mobility [176]. One approach to overcome the adverse effects of disorder includes the introduction of a highly ordered and electrically performing material into the matrix of the OS in order to decrease the number and size of the defects by generating percolation pathways for charge transport in the disordered regions. Liquid phase device processing requires that both components are soluble or dispersible in compatible solvents, resulting in homogeneous blends that prospectively allow for upscalable deposition methods such as spin coating and printing. To ensure device performance, both materials must also exhibit favorable alignment of electronic energy levels. Such alignment is a prerequisite for lossless transport between the OS and the metallic contacts. Considering PDIF-CN2, GNs represent a favorable choice due to similar solubility in solvents that are typically used for processing of perylenediimides such as chloroform. Also both materials share favorable relative positions of LUMO. The work function of graphene is 4.56 eV [189] and HOMO and LUMO of PDIF-CN2 [190] are -6.8 eV and -4.5 eV respectively, hence there is no mismatching of the energy level, as a result there is no bottleneck for the flow of charge into graphene. We have investigated the role of GNs on the charge carrier mobility in graphene and

PDIF-CN2 blends (GN:PDIF-CN2) fabricated from solutions.

5.2.1 Experimental

GNs were prepared with liquid phase exfoliation of 3 mg/ml graphite flakes in chloroform or 0.1 mg/ml PDIF-CN2 solutions in chloroform respectively. The mixtures were sonicated in a bath sonicator for 4.5 hours and then centrifuged at 2200 rpm for 30 min to remove larger, graphitic particles. To measure I-V characteristics measurements we have fabricated bottom-gate bottom-contact transistors on heavily doped n-type silicon wafers serving as gate electrode with 230 nm thick thermally grown SiO₂ as the dielectric layer ($C_i=15 \text{ nF/cm}^2$) and pre-patterned interdigitated Au source-drain electrodes with channel length of 2.5 μm and channel width of 10 μm . SiO₂ dielectric interface was treated with hexamethyldisilazane (HMDS), followed by thermal annealing at 80 °C for 30 min. Au electrodes were rendered hydrophobic by chemisorption of a self-assembled monolayer (SAM) of decanethiol, obtained by immersion of the electrodes in a 3 mM solution in ethanol overnight. PDIF-CN2 dissolved in chloroform at a concentration of 0.1 mg/ml with and without graphene flakes was spin coated at a speed of 1500 rpm. In order to check the role of graphene on the photoconductivity the PDIF-CN2 and blended layers were deposited on glass substrate by spin-coating of the same solutions at 500 rpm. Samples for transient photocurrent measurements comprised coplanar Al electrodes deposited by vacuum evaporation (evaporation rate =1 nm/s) using a shadow mask onto GN:PDIF-CN2 covered glass, which were previously treated by HMDS. The resulting effective inter-electrode separation (d) was 100 μm for samples comprising PDIF-CN2, and 150 μm for samples comprising GN:PDIF-CN2. Sample fabrication for TOF and all electrical measurements were performed in a nitrogen-filled glove box, at room temperature. A DC voltage ranging from $\pm 300 \text{ V}$ to $\pm 500 \text{ V}$ was applied between the electrodes. Biased samples were illuminated near the biased electrode by pulsed, variable-wavelength laser with pulse duration of 3 ns and the pulse repetition rate of 3 Hz. The opposite electrode was grounded via a 100 k Ω resistor, and the resulting I(t) was measured as a voltage drop across the resistor by a 2.5 GHz oscilloscope.

5.2.2 Results and Discussion

In Fig. 5.10 we have presented the transfer characteristics of FETs with a PDIF-CN2 channel and in Fig. 5.11 we have presented transfer characteristics of GN:PDIF-CN2. Typical saturation electron mobilities obtained on PDIF-CN2-channel transistors were $1.3 \times 10^{-4} \text{ cm}^2/\text{Vs}$. Transistors comprising GN:PDIF-CN2

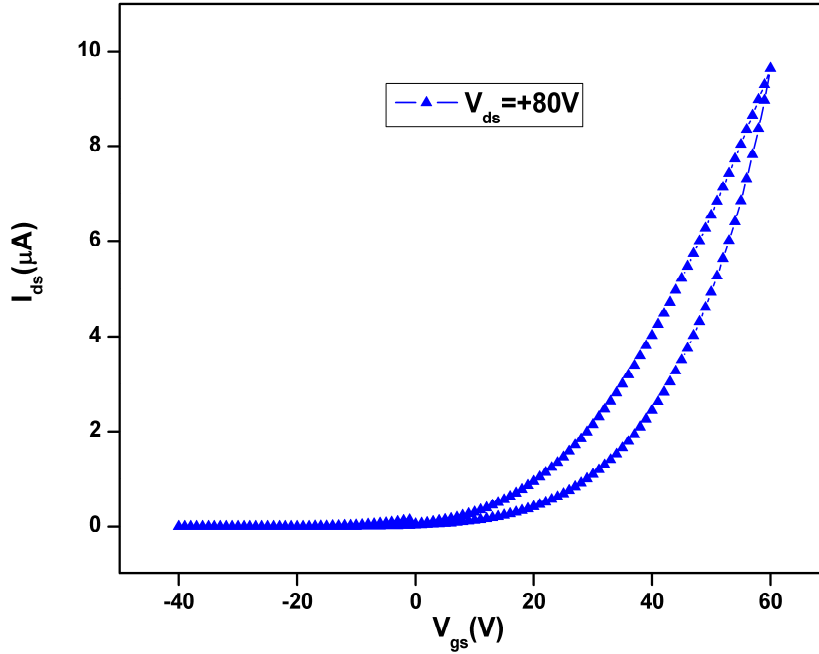


Figure 5.10: Transfer characteristics of PDIF-CN2 based FET at $V_{ds}=80 \text{ V}$ having a channel length $L=2.5 \text{ μm}$ and width $W=1 \text{ cm}$.

channel, instead exhibited clear current modulation that we associate with the transport across the manifold of GNs. In addition, the electron mobility in these devices reached values as high as $0.2 \text{ cm}^2/\text{Vs}$. The transfer characteristic of GN:PDIF-CN2-based FETs exhibits a double slope with rapidly increasing current for gate voltages above about 70 V. This phenomenon is likely to be a consequence of gradual space charge accumulation on PDIF-CN2 domains. Gate-accumulated charge in FETs can be divided in two groups – trapped and mobile. As the accumulation increases, low-lying energy levels in PDIF-CN2 are filled with electrons. With increasing gate potential, the accumulation occurs on higher energy levels, which are aligned with graphene levels. This alignment with graphene levels favors mobility of the accumulated charges, which contribute significantly to the current. This is observed as an important increase in slope of the transfer

characteristics, and the resulting relatively high field-effect mobility.

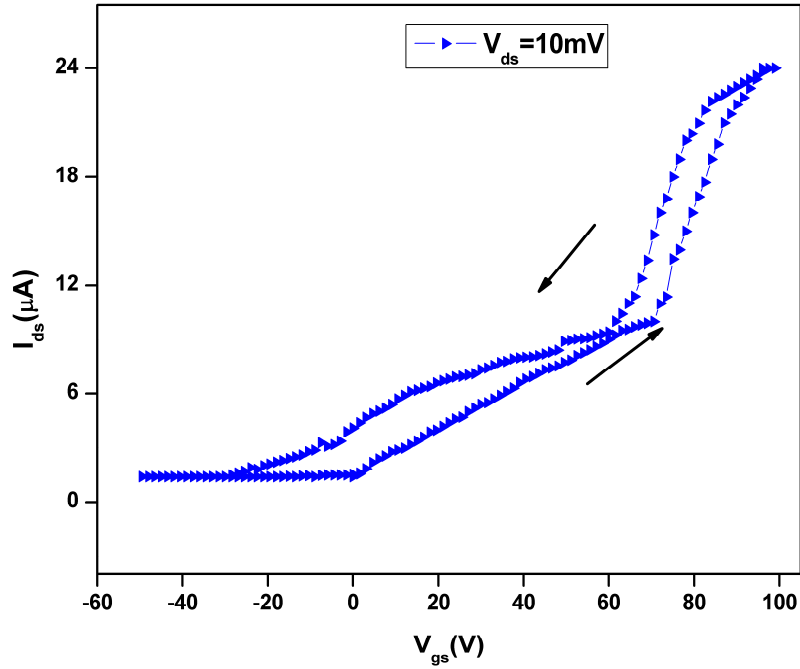


Figure 5.11: Transfer characteristics of GN:PDIF-CN2 based FET at $V_{ds}=10$ mV having a channel length $L=2.5$ μm and width $W=1$ cm.

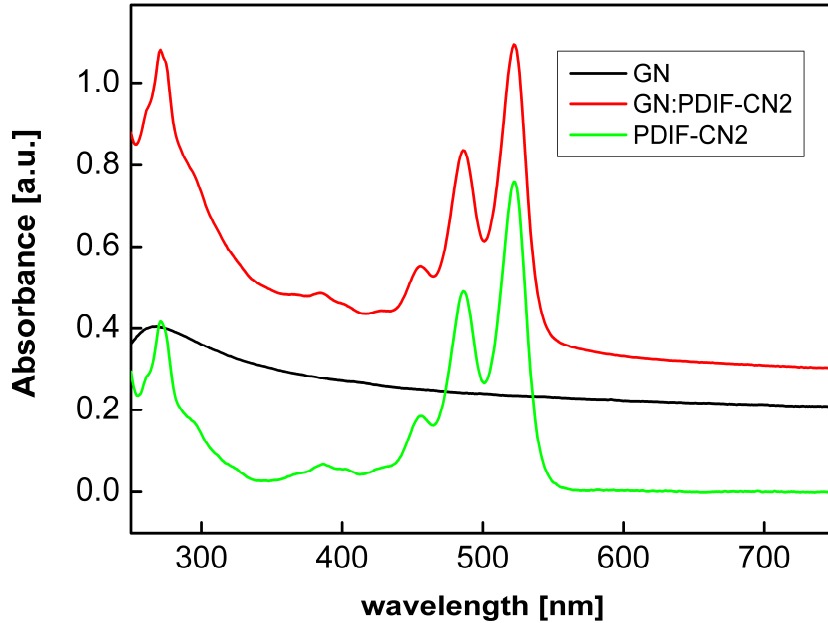


Figure 5.12: Absorption spectra of PDIF-CN2, GN and GN:PDIF-CN2.

Further insight into the charge transport mechanism in these devices was obtained from TOF photocurrent measurements that were performed by using two different wavelengths. The wavelength of $\lambda=530$ nm corresponds to the absorption

maximum in PDIF-CN2. At $\lambda=210$ nm absorption in PDIF-CN2 is relatively weak, while absorption in graphene is still significant. This is exemplified in Fig. 5.12, where we show the solid-state absorption spectrum of PDIF-CN2, GNs and GN:PDIF-CN2.

The enhancement of charge transport properties observed in FETs by blending GNs with PDIF-CN2 was also observed in TOF photocurrent measurements. Figures 5.13 display the $I(t)$ characteristics measured on PDIF-CN2 layers. $I(t)$ curves were obtained by illuminating the samples with the light of wavelength of 530 nm. Briefly, $I(t)$ curve reflects a photogenerated electric charge current that stems from charge carriers drifting in the interelectrode electric field. From the polarity of the bias we discern the polarity of the charge carries. For positive bias $I(t)$ reflects the hole current (squares and circles), for negative bias $I(t)$ reflects electron current (triangles). The carriers that are generated near the biased electrode by a laser pulse become charge-separated by the applied electric field. For positively (negatively) charged electrode the electrons (holes) drift to the illuminated electrode and contribute only a fraction of current in the $I(t)$ curve. The opposite charged carriers instead drift away from the biased electrode and their $I(t)$ is being recorded. The interelectrode electric field is strongly position-dependent, and is enhanced in the region of few μm from the metal/channel interface. The carriers that are generated near the biased electrode initially sense a high acceleration that gives rise to an initial surge in $I(t)$. As the carriers enter the low-field region deeper in the channel, their effective drift velocity starts decreasing. Consequently, $I(t)$ exhibits a relatively monotonic decrease. Upon arrival of the fastest carriers to the collecting electrode, a region of high electric field is again experienced. This may be manifested in the $I(t)$ curve as a plateau or in the case of highly ordered materials by a cusp, followed by a rapid decrease in current due to the migration of the carriers into the electrode.

Figure 5.14 display the $I(t)$ characteristics measured on GN:PDIF-CN2 layers. In Fig. 5.14 we see that the electron $I(t)$ s (diamonds) exhibit the features described above. We see a monotonic decrease and a clear change of slope (indicated by the arrow) followed by a noise signal. From these curves we determine the transit time of the fastest carriers. We see that t_{tr} is consistently shifted to lower values as the accelerating voltage is increased, as expected for drift transport of the electric charge

carriers. An estimate on the effective mobility can be obtained by assuming a position independent interelectrode electric field in the formula 2.1 for mobility $\mu = \frac{d^2}{Vt_{tr}}$. On samples comprising pristine PDIF-CN2 (Fig. 5.12) we have determined the electron mobility to be $10^{-4} \text{ cm}^2/\text{Vs}$, while on samples comprising GN:PDIF-CN2 we have obtained the values of $1.6 \times 10^{-3} \text{ cm}^2/\text{Vs}$. Such an order of magnitude increase in electron mobility coupled to the observed changes in transfer curves (Figs. 5.10 and 5.11) upon blending GNs to PDIF-CN2, argues that GNs act as regions of high-mobility within the OS matrix. These values are not favorably with the values obtained on FETs.

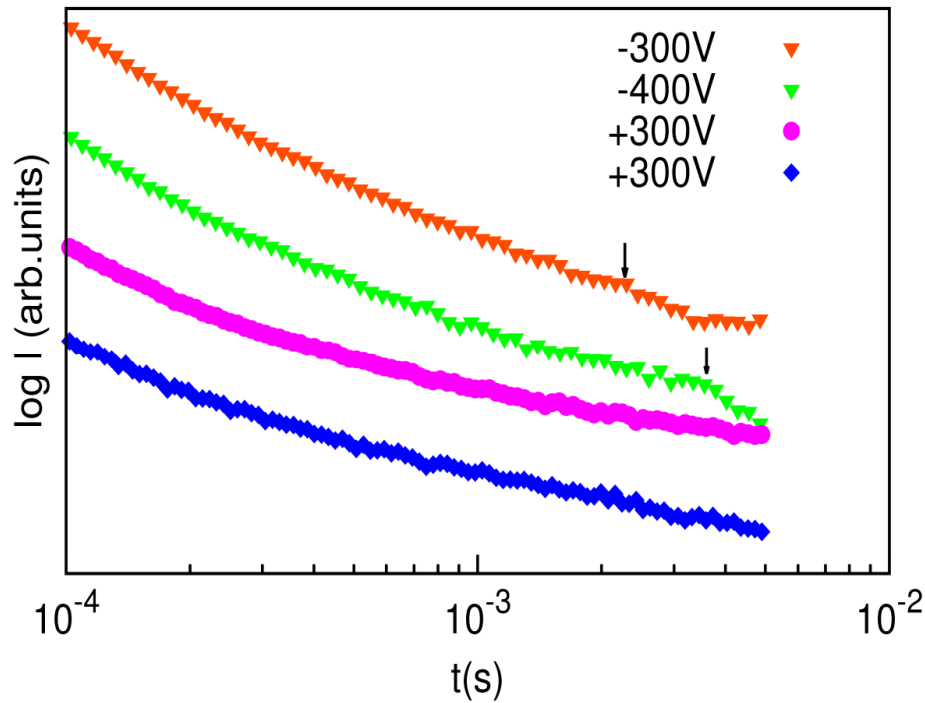


Figure 5.13: Double logarithmic plot of photocurrent vs time in PDIF-CN2 at a wavelength of 530 nm for both polarities. The curves are shifted vertically for clarity.

We note however that there are differences in between the two experiments, which may affect the absolute values of the mobility. Firstly, in TOF experiments we have used Al contacts in order to reduce the amount of field-injected charge carriers. TOF measurements are based on the current due to predominantly photogenerated charge carriers. I-V characteristics measurements instead, are based on charge injection from the Au contacts. The charge carrier density in this case is substantially

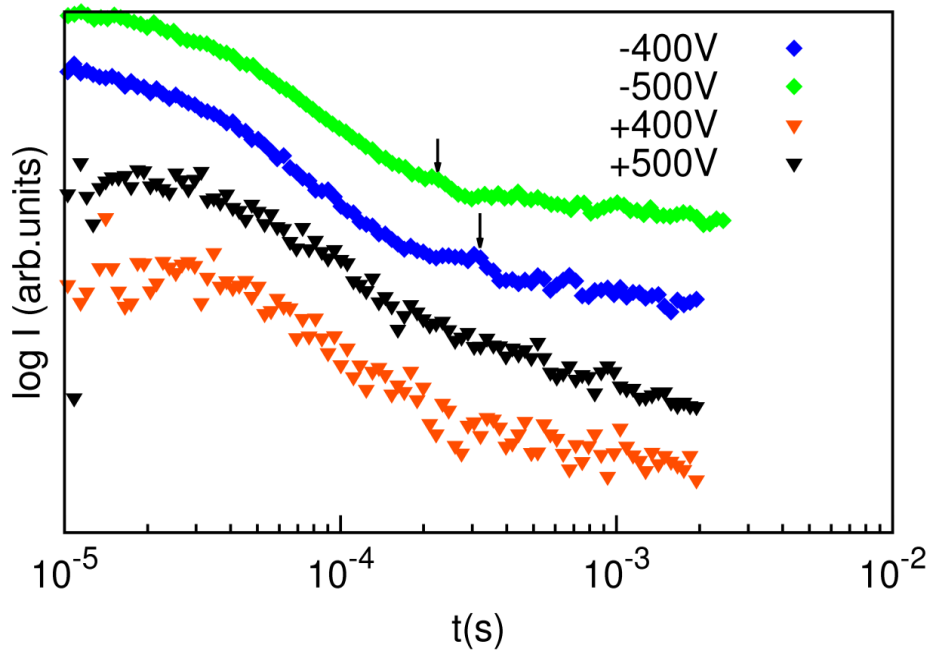


Figure 5.14: Double logarithmic plot of photocurrent vs time in GN:PDIF-CN2 blends at a wavelength of 530 nm for positive bias.

higher than in the case of the photogenerated charge carriers, affecting thereby the charge carrier transport throughout the intercarrier interactions. Secondly, the assumption of uniform electric field (Eq. 2.1) in the channel is far from reality. Numerical calculations of Laplace equation [147] for two coplanar electrodes demonstrate that the electric field intensity drops rapidly with the distance from the electrode. This results in relatively low electric field intensity inside the channel. Our Monte Carlo simulations of $I(t)$ in P3HT channels indicate that the use of Eq. 2.1 to estimate the charge carrier mobility may result in values that are almost one order of magnitude lower than the values obtained by assuming a position-dependent electric field. Regardless of the absolute value of charge carrier mobility we conclude that blending GNs with PDIF-CN2 considerably increases the mobility of charge carriers.

Focusing on the $I(t)$ curves obtained using positive bias (Fig. 5.14, triangles), which reflect transport of holes across the channel, we see that the initial surge of current in these curves is also present and is associated to initial fast acceleration of holes in the high-field region near the biased electrode. However, since PDIF-CN2 is an n-type semiconductor, hole transport is subjected to an increased concentration of

traps, resulting in a monotonic decrease in current. The resulting $I(t)$ lineshape therefore exhibits a monotonic decrease that is substantially faster relative to the electronic $I(t)$ once the holes exit the high-field region. This is a signature of rapidly decreasing current due to hole trapping before they reach the collecting electrode. The behavior of hole transport in PDIF-CN2 layer, as observed in TOF measurements, is therefore consistent with its n-type. Interestingly similar behavior of holes is repeated also in the case of GN:PDIF-CN2 (Fig. 5.14, triangles), indicating that the addition of GNs into the OS matrix does not induce ambipolar character to the blend.

In Fig. 5.15 we compare electron $I(t)$ obtained on GN:PDIF-CN2 on glass using a bias of -400 V, and photon wavelength of 530 nm and 210 nm, shown as blue triangles and green circles, respectively. In Fig 5.16, we compare electron $I(t)$ obtained GN:PDIF-CN2 on glass for different applied bias voltages at a wavelength of 210 nm. The transit time is indicated by the arrow and it is moving towards shorter times, with the applied voltage, as expected. As the applied bias is increasing, the carriers drift towards the opposite electrode faster, hence the transit time is lower. We see that $I(t)$ obtained by high-energy photons decreases rapidly, but exhibits a distinct plateau before vanishing into the noise level. The $I(t)$ lineshape warrants that the electrons have traveled across the channel and reached the collecting electrode. The transit time of the fastest carriers is $t_{tr} = 6 \times 10^{-6}$ s, resulting in mobility of $\mu = 0.1 \text{ cm}^2/\text{Vs}$. This is one order of magnitude higher than the mobility of electrons obtained with low-energy photons and compares to the mobility obtained with FETs.

In order to explain this behavior we consider the alignment of relevant electronic energy levels in GN:PDIF-CN2 and their relations relative to the energy of the incoming photons. Graphene work function is 4.56 eV [189], while the position for HOMO and LUMO in GN:PDIF-CN2 are, -6.8 eV and -4.5 eV, respectively [190]. When low-energy photons (2.34 eV) are used for charge excitation, the primary absorption occurs in PDIF-CN2, where excitons are created. Absorption of these photons in graphene is almost three times smaller than the peak absorption in PDIF-CN2. After the excitonic decay, the electrons experience favorable alignment of LUMO in PDIF-CN2 and the Dirac point in graphene for their transport from PDIF-CN2 to graphene, and further to Al electrode. Based on the Anderson model, Al/PDIF-CN2 and Al/GN:PDIF-CN2 interfaces exhibit energy level offset of 0.2 eV

and 0.3 eV, respectively.

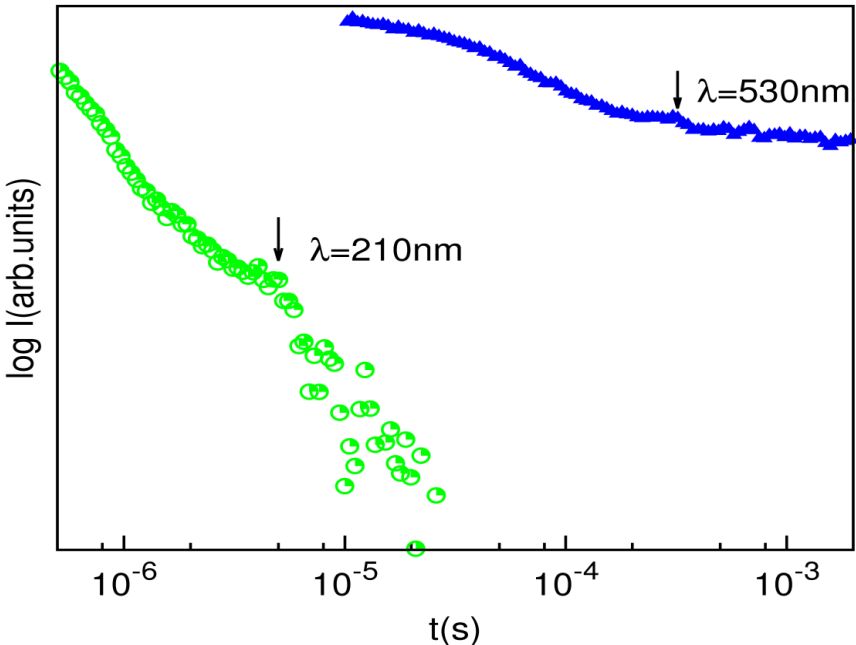


Figure 5.15: Comparison of electron $I(t)$ obtained on GN:PDIF-CN2 on glass using a bias of -400 V, and photon wavelength of 530 nm and 210 nm.

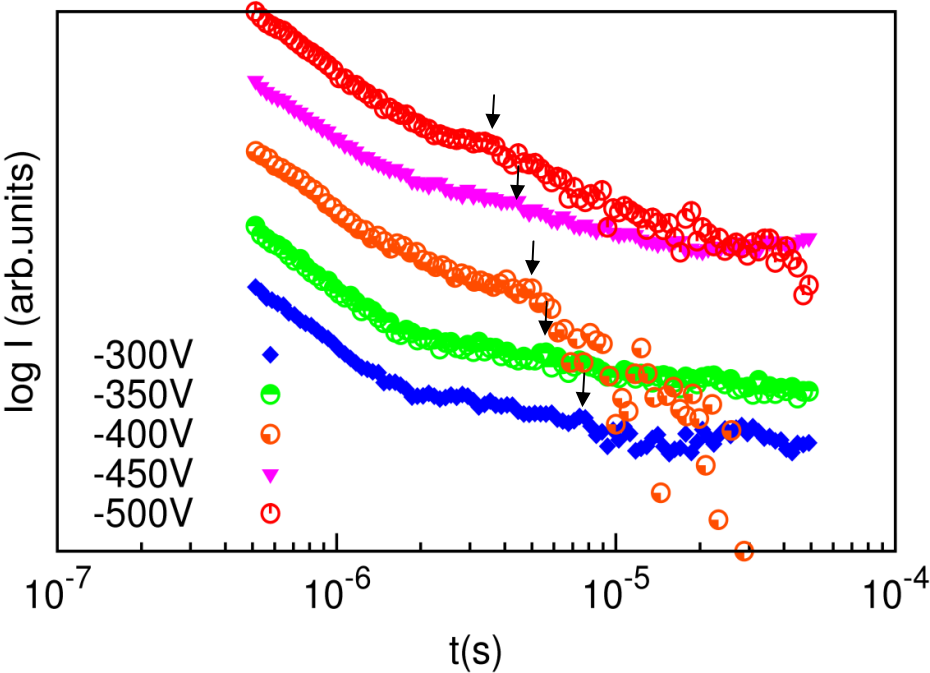


Figure 5.16: Double logarithmic plot of photocurrent vs time in GN:PDIF-CN2 blends at a wavelength of 210 nm for negative bias. The curves are shifted vertically for clarity.

On the other hand, photons with energy of 5.9 eV ($\lambda=210$ nm) are primarily absorbed in graphene by interband direct excitation of electrons from occupied into the unoccupied states near the saddle-point singularity at the M point of the Brillouin zone [192]. It has been shown that the correct treatment of optical response of graphene at these energies must include excitonic effect [193,194]. Theoretical modeling of the band transitions indicate excitonic lifetimes of only 0.5 fs [194], so that we may consider the carriers excited by ultraviolet light essentially as free on the timescale of our experiment. Comparison of the two I(t)s shows that electrons created by high energy photons exhibit almost two orders of magnitude shorter transit time ($t_{tr}=6\times 10^{-6}$ s) than the electrons created by 530 nm-photons.

We argue that the observed dependence of t_{tr} on the excitation wavelength reflects different electron transporting channels within the blend. Considering first electrons originating from decay of the excitons, which are the product of the interaction of photons with molecules, we note that in the high electric-field region near the biased (and illuminated) electrode, electrons drift towards the collecting electrode through the GN:PDIF-CN2 network, by sequentially occupying relaxed states (negative ions) on PDIF-CN2 molecules or quasi extended states residing on GNs. Their energy in the relaxed state is determined by the lattice deformation potential, and by vibronic and electronic polarizations. This implies that the residence time in the relaxed state is determined by the ratio between the electron kinetic energy and the sum of the three polarizations [212]. By increasing kinetic energy of the electron is increased the vibronic and lattice polarization times become too long to be effective, and with further increase of kinetic energy the electronic polarization is also lost. These hot electrons start behaving almost as free electrons whose transport is limited by elastic inelastic scattering events within the layer.

In our material system creation of hot electrons is possible by excitation of GNs using photons with $\lambda=210$ nm (energy= 5.90 eV). As has been shown by Tielrooij *et al.* [213] the interaction of these hot electrons with the electrons on the Fermi surface, increases their residence time in the conduction band of graphene. Consequently due to applied electric field these hot electrons move through the GN:PDIF-CN2 layer, essentially absent of lattice, vibronic and electronic polarization. Their only significant recombination events are likely to occur at the GN/PDIF-CN2 interfaces. Therefore the contribution of these relatively few albeit

extremely fast electrons dominates the observed $I(t)$ lineshape, which exhibits a marked cusp signaling their arrival at the collecting electrode. From the markedly reduced t_{tr} of these electrons we conclude that the interruptions of the high-energy transporting manifold are relatively short, and do not influence appreciably the transport properties of the blend. This again argues for GNs forming a percolating network within the blend.

5.3 Improvement of mobility of organic semiconductors with mechanically exfoliated graphene flakes

Solution processed OFETs are suffering from low mobility. In order to improve the mobility of these OFETs, we have reduced channel length by incorporating graphite flakes in the channel, which is equivalent to increasing the effective mobility of OSs. The charge carriers flowing from source to drain electrode will take advantage of flowing partially through OS and partially through graphene. Thus, traveling only a fraction of the distance within the semiconductor leads to an effective channel length reduction [168-173].

5.3.1 Experimental

The heavily doped silicon substrates covered with thermally grown silicon oxide of 300 nm thickness was employed as the gate dielectric as well as the substrate. The graphite flakes are made by the Scotch tape method [3, 7, 8]. The flakes contain single, bilayer and multilayer graphene flakes, as determined from the optical contrast. The electrodes were deposited by using electron beam gun using a shadow mask and the channel length and width are 100 μm and 1000 μm . The graphene flakes within the channel are confirmed by the optical microscope as shown in Fig. 5.17. P3HT is dissolved in chloroform at a concentration of 1 mg/ml and then spincoated at a speed of 1000 rpm. The same P3HT solution was spincoated onto FETs without graphite flakes and the results were compared.

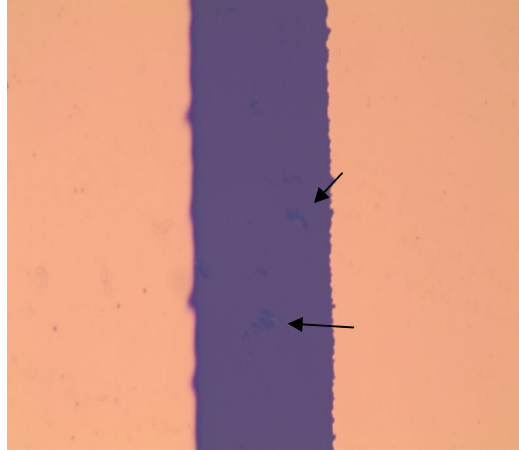


Figure 5.17: Optical microscopic image of the graphene flakes in the channel between the gold electrodes on 300 nm Si/SiO₂ substrates.

5.3.2 Results and Discussion

In Fig. 5.18 we compare the transfer characteristics of a P3HT-based FETs with and without graphene flakes. Figs. 5.18a) and b) show transfer characteristics in the linear and saturation regime respectively for the FETs without graphene flakes in the channel. Figs. 5.18c) and d) show transfer characteristics in the linear regime and b) in the saturation regime respectively for the FETs with graphene flakes in the channel. The linear and saturation mobilities for holes are estimated from the linear part of the curves. The saturation mobility of P3HT-based FETs with graphene flakes in the channel is 0.01 cm²/Vs and without flakes are 10⁻⁴ cm²/Vs. The linear mobility with graphene flakes in the channel is 7.1×10⁻³ cm²/Vs and without flakes are 2×10⁻⁴ cm²/Vs. The mobility of pristine P3HT is relatively low; since the thickness of the film is 5-10 nm, and the smaller grains at the Au/OS interface leads to poor injection. The performance of FET with bottom-contact (BC) configuration is inferior to that of the top-contact (TC) configuration FET with the same active material. The reduction of FET performance on BC configuration results from poor growth of OS layer on and close to metal contact electrodes due to large surface energy difference between the electrodes and gate dielectrics. The poor growth of OS layer at the Au/dielectric interface results in lowering of charge carrier mobility and also causes large electric contact resistance between FET-channel and contact electrodes [202-205]. The two orders of magnitude increase in the mobility is due to the insertion of the graphene flakes in the channel. The remarkable increase in the mobility compared GN:P3HT

blend is due to reduction of interconnected junctions and the highly conductive graphene flakes. Since the size of the flakes is several μm , the number of

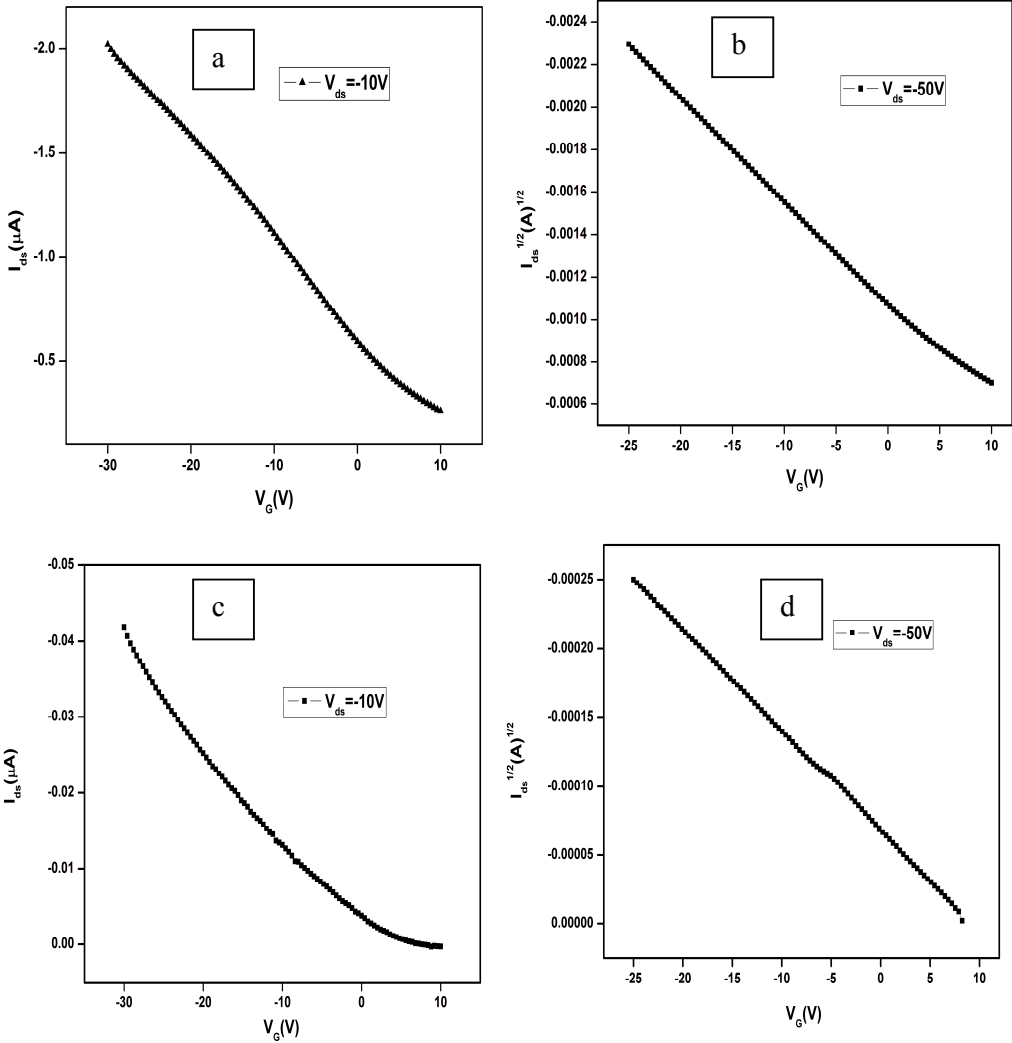


Figure 5.18: a) Transfer characteristics of a P3HT-based FETs in the linear regime and b) in the saturation regime with mechanically exfoliated graphene flakes in the channel and c) and d) without flakes in the linear and saturation regime respectively.

interconnecting junctions are low, but in blends, the size of the flake is from several nanometers to few μm . Thus the number of interconnecting junctions is more in order to reduce the same amount of channel length. Due to the misalignment of the energy levels between graphene (-4.56 eV) [175] and HOMO of P3HT (-5.1 eV) [189] the contact resistance at their interface leads to poor injection for holes. As the

number of interconnecting junctions increase, the contact resistance dominates the channel resistance, which leads to poor mobility. This indicates that improvement depends upon the quality of the flakes inserted and its mobility and the number of interconnecting junctions. But the main difficulty in this method is low throughput and control over the flakes within the channel. We cannot use top contact configuration, because after the deposition of the material, it is difficult to find the location of the flakes.

5.4 Conclusions

In conclusion the performance of the P3HT-based FETs can be improved with the addition of graphene flakes. At the GNs concentration of 0.06 mg/ml, the mobility improved by 7 times but the $I_{\text{on}}/I_{\text{off}}$ ratio decreases more than one order of magnitude. With further increasing the concentration of GNs, the mobility starts to drop because of the contact resistance at the P3HT/GN interface due to mismatching of the energy levels. With further increasing the concentration of GNs, the number of interconnecting junctions also increases, and the contact resistance dominates the channel resistance and leads to poor mobility. With increasing the concentration of GNs, I_{off} current starts to increase due to percolating networks. At higher concentration of GNs leads to morphological changes and disrupts molecular ordering of the P3HT molecules and agglomeration of the graphene flakes leads to poor performance of the device.

We have made the blend of GNs and PDIF-CN2 and we have increased the electron mobility as determined both by measuring the FETs transfer curve and by transient photoconductivity of thin films in coplanar electrode arrangement. The electron mobility increases from 10^{-4} cm²/Vs in pristine PDIF-CN2 thin films to 0.2 cm²/Vs in thin films of GN:PDIF-CN2 is associated to the formation of the percolating network of GNs within the organic semiconductor matrix. By exciting the carriers into the transporting states that reside higher in energy we have also demonstrated the existence of a high-electron-mobility channel comprising quasi-extended states within the blend, resulting in further increase in electron mobility.

We demonstrated that the effective mobility of the P3HT can be enhanced as high as 100 times without reduction of the $I_{\text{on}}/I_{\text{off}}$ upon incorporation of graphene

flakes in the channel of the device. The remarkable increase in hole mobility of P3HT with mechanically exfoliated flakes over that of pristine P3HT is due to the incorporation of graphene flakes between the source and drain electrodes which are acting as conducting bridges and reduce the effective channel length of the device.

Chapter 6: Performance enhancement of OFETs using graphene flakes and characterization of graphene nanoribbons

In this chapter we demonstrate an alternative approach for the improvement of mobility of OFETs by incorporating the electrochemically exfoliated graphene (ECG) flakes between the gate dielectric and the OS layer. In the next section we have presented the charge transport properties of GNRs as a function of channel length in FETs and by the TOF technique.

6.1 Performance enhancement of P3HT-based FETs with electrochemically exfoliated graphene flakes

With the aim of enhancing the field-effect mobility of P3HT-based FETs, we have demonstrated an alternative approach for achieving high transconductance by assembling SLG networks produced by electrochemically exfoliation on the dielectric surface. We show here that the by introducing SLG networks, the effective channel length of FET can be reduced thus enabling the increase of the device transconductance without the reduction of I_{on}/I_{off} ratio. The transconductance of the transistor is proportional to the mobility and it is inversely proportional to the channel length providing a parameter to be tuned for optimum device performance. Transconductance of a FET in the saturation regime is given by

$$g_m = \mu C_{ox} \frac{W}{L} (V_{gs} - V_T), \quad (6.1)$$

where g_m is the transconductance of a FET, μ is the mobility, W is the channel width, L is the channel length and V_T is the threshold voltage.

The schematic view of FET incorporated with graphene flakes is as shown in Fig. 6.1. The graphene flakes are placed at dielectric/OS interface in the conducting channel. The OS layer is deposited on top of the flakes. Electrodes can be deposited prior to the deposition of the OS layer (bottom contact geometry) or they can be

deposited after the deposition of the OS layer (top contact geometry). The charge carrier current flows from the source electrode through the OS, through the graphene flakes, and again moved into OS and finally reached into the drain electrode. The carriers flowing from the source to drain pass through the highly conducting regions

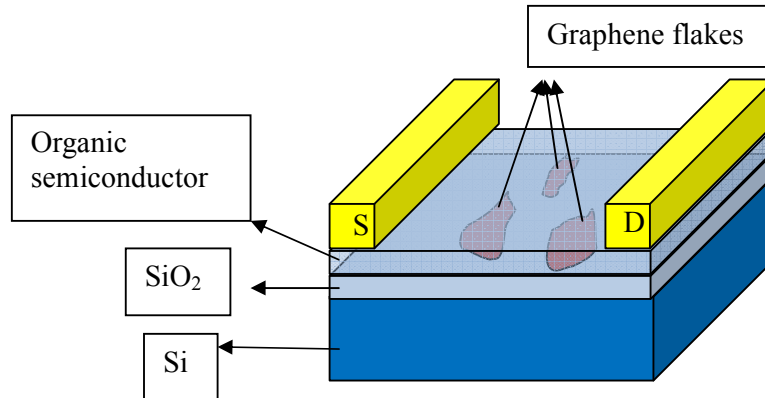


Figure 6.1: Schematic representation of FET with electrochemically exfoliated graphene flakes in the channel.

of graphene within the semiconductor matrix. Traveling only a fraction of the distance within the semiconductor leads to an effective channel length reduction, thus enhancing the transconductance [171].

In addition to this, there are several advantages of incorporating the graphene flakes at the dielectric and OS layer. This method appears to be more advantageous than making the blends of OS and GNs or CNTs [168-173]. The GN/OS blends are limited to materials that can be solution-processed only. But in this approach, the OS layer can be evaporated or spin coated. In blends, flake sizes are few nm to few microns; hence there is lot of interconnecting junctions and the contact resistance of the graphene/OS interface will degrade the performance of P3HT-based FETs at higher concentrations. In addition, at higher concentration of GNs they form a percolation networks. It leads to rapid increase in I_{off} current, thus lowering the I_{on}/I_{off} ratio. But the flake size of the ECG flake varies from several μm to $30 \mu\text{m}$, thus we can reduce the number of interconnecting junctions substantially. Since most of the charge flow through first monolayers [196,197,206] and graphene is a 2D material and due to high conductivity, hence the transconductance of the OS can be improved.

In addition, the coverage of the ECG flakes can be easily controlled by dip-coating method, which can avoid the controllability problem with mechanically exfoliated graphene flakes as explained in the previous chapter. In this section we investigate the electrical properties of P3HT with partially covered single-layer ECG flakes in the conduction channel of FET.

6.1.1 Experimental

The experimental setup for the production of electrochemically exfoliated single layer graphene flakes is the same as explained in section 1.2.4. Natural graphite flakes, and platinum wires are used as electrodes and 0.1 M H₂SO₄ acts as electrolyte respectively. When a positive voltage (i.e., +10 V) was applied to a graphite electrode, the graphite flakes begin to expand, quickly dissociate, and spread into the solution upon sweeping between +10 V and -10 V. The bias voltage was kept constant at +10 V for 2 min to complete the exfoliation process. Afterward, the exfoliated graphitic material was collected by vacuum filtration and washed repeatedly with water to remove the residual acid. Finally, the obtained powder was dispersed in dimethylformamide, resulting in ECG flakes. These ECG flakes were uniformly deposited on SiO₂ by vertically dip coating the substrate, followed by thermal annealing at 200 °C to remove the residual solvent [46]. P3HT was dissolved in chloroform at a concentration of 3 mg/ml and then spin coated at 1000 rpm for a minute on Si/SiO₂ surfaces containing ECG flakes and without ECG flakes. 25 nm-thick gold electrodes were deposited by thermal evaporation using a shadow mask and the resulting channel length is 150 μm and width is 300 μm. We have further tested the effect of ECG flakes on the BC FETs as well. The ECG flakes were deposited onto the Si/SiO₂ in the same way as before. The gold electrodes were deposited onto these substrates using a shadow mask. The resulting channel length is 100 μm and width is 5000 μm. P3HT is dissolved in chloroform at a concentration of 3 mg/ml and then spin coated at a speed of 1000 rpm for a minute. Then these devices were annealed at 90 °C for 20 min and then tested inside the nitrogen-encapsulated glove box at room temperature.

6.1.2 Results and Discussion

AFM image of P3HT layer on SiO₂ and on SiO₂ with ECG flakes are shown in Fig. 6.2. The morphology shows the polymer structure forms a random network of spherical grains with the diameter of 30 nm. The RMS roughness of the layer on SiO₂ is 0.41 nm and on SiO₂ with ECG flakes is 0.456 nm. The slight rise in roughness of the polymer film could be due to the presence of chemical residues of the solvent, which is used to deposit ECG layers.

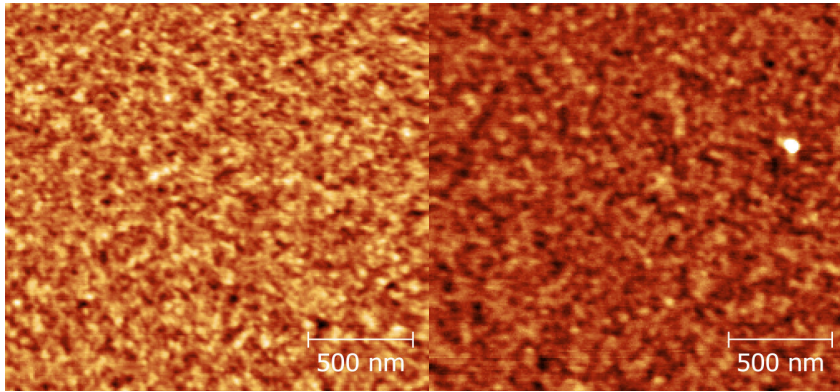


Figure 6.2: 3 μm ×3 μm AFM image of the P3HT layer on SiO₂ (left) and on SiO₂ with ECG flakes (right).

In Fig. 6.3 we compare the transfer characteristics of P3HT-based FET without (green curve) and with ECG flakes (red curve) in the linear regime. The linear mobility was extracted from the slope of the transfer curves with and without ECG flakes is 0.2 cm²/Vs and 0.005 cm²/Vs respectively. The 40-fold improvement in the mobility over that of pristine P3HT layer is due to the high conductivity of the ECG flakes, which are acting as conducting bridges connecting the grains of P3HT layer. In addition to that, the I_{on}/I_{off} ratio increased by 20 times with ECG flakes than without flakes. The I_{off} current doesn't increase, which implies that there are no appreciable percolating networks of graphene. This is further supported by the increase in the I_{on} current. ECG flakes are p-type graphene, due to the chemical residues present on it, thus the injection barrier for hole transport from ECG flakes to P3HT is also lowered. When the charge carriers start to flow from source to drain electrodes, partially flow through highly conducting graphene and partially through P3HT. Travelling only a fraction of distance within P3HT leads to an effective channel length reduction and improvement in the mobility. In Figs. 6.4 and 6.5 we present the output characteristics of P3HT-based FETs with ECG flakes and without

ECG flakes in the channel for different gate voltages with a step of 25 V, respectively. V_{ds} is varied from 0 to -50 V and I_{ds} increases with increasing the gate voltage.

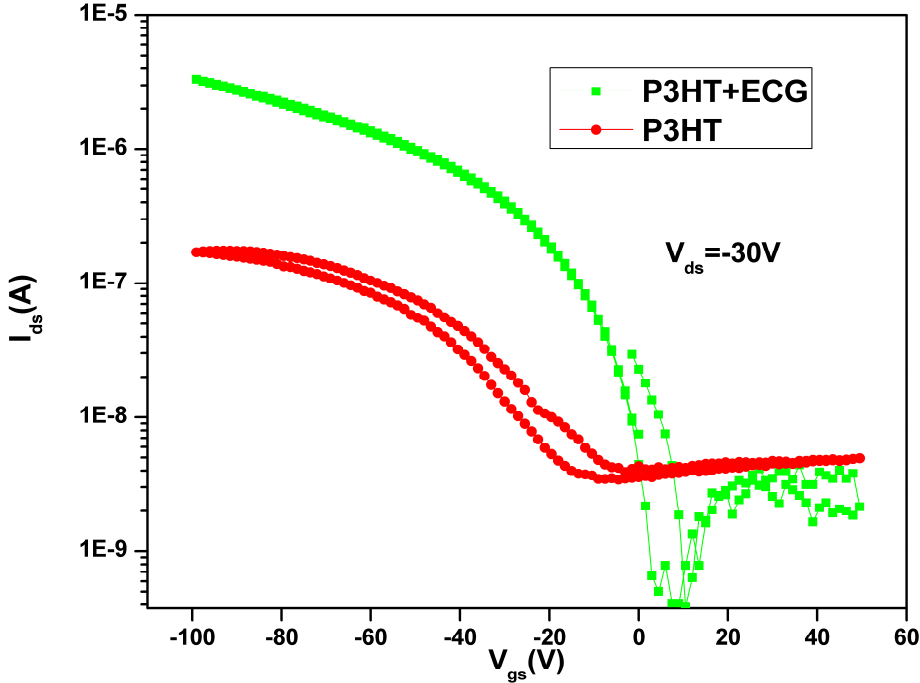


Figure 6.3: Comparison of the transfer characteristics of P3HT-based FETs with and without ECG flakes in the channel at constant $V_{ds}=-30$ V.

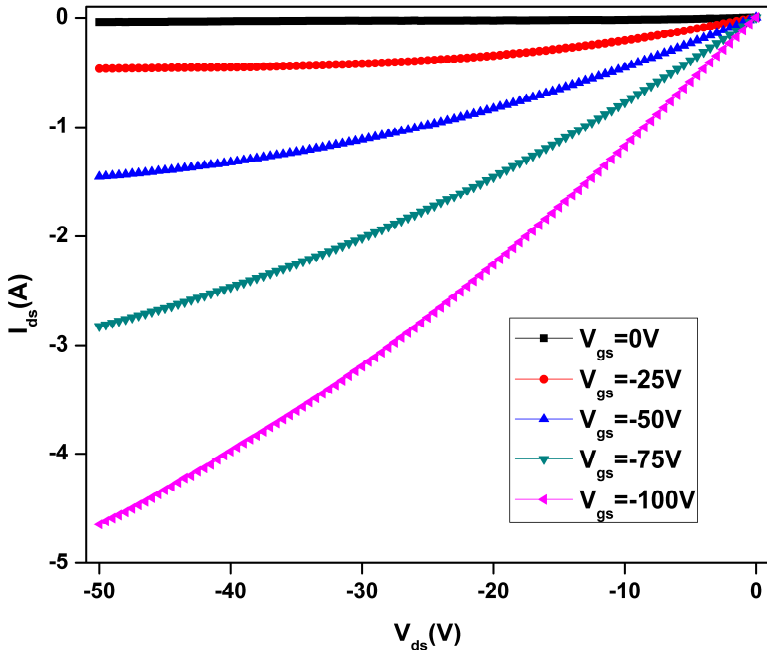


Figure 6.4: Output characteristics of a P3HT-based FET ($L=150 \mu\text{m}$ and $W=300 \mu\text{m}$) with ECG flakes in the channel for different V_{gs} . V_{ds} is varied from 0 to -50V.

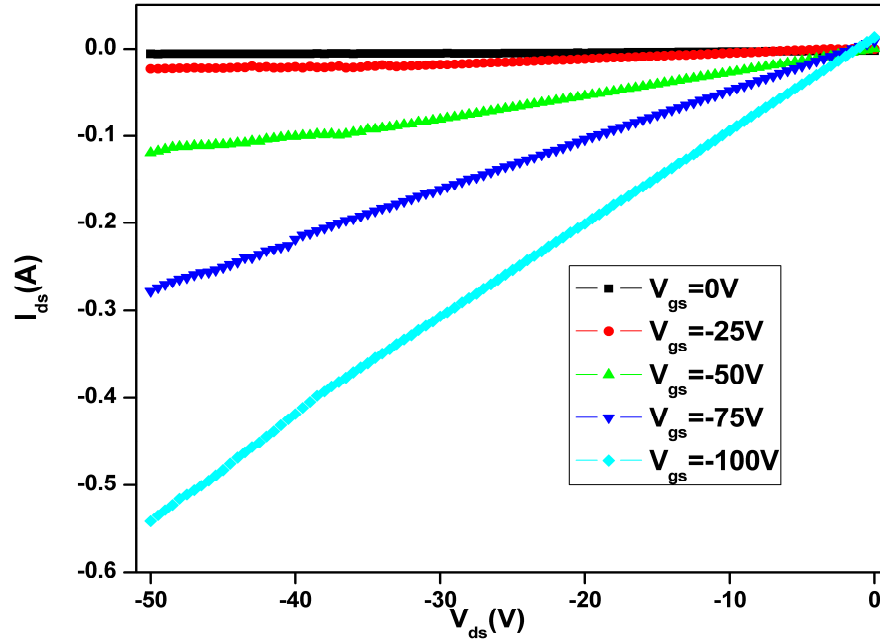


Figure 6.5: Output characteristics of a P3HT-based FET ($L=150 \mu\text{m}$ and $W=300 \mu\text{m}$) without ECG flakes in the channel for different V_{gs} . V_{ds} is varied from 0 to -50V .

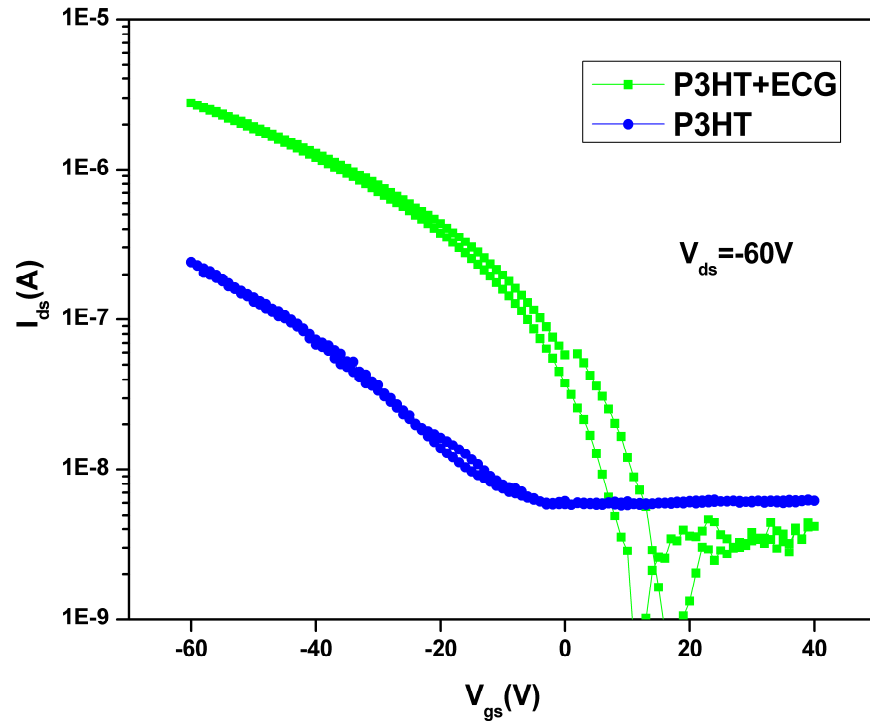


Figure 6.6: Comparison of the transfer characteristics in the saturation regime of a P3HT-based FETs ($L=150 \mu\text{m}$ and $W=300 \mu\text{m}$) on a semilogarithmic plot with and without ECG flakes in the channel at constant $V_{ds}=-60 \text{V}$.

In Fig. 6.6 we compare the transfer characteristics of P3HT-based FETs

without (green curve) and with ECG flakes (blue curve) in the saturation regime. The saturation mobility has increased from $0.004 \text{ cm}^2/\text{Vs}$ to $0.1 \text{ cm}^2/\text{Vs}$ with the incorporation of ECG flakes in the conducting channel. The increase in the mobility is due to the presence of ECG flakes in channel, which are acting as conducting lanes for charge transport. These flakes that are on the dielectric surface and the charge carrier accumulation residing on them can be tuned via the gate voltage. This implies that a sheet of charge can be formed at the interface with the dielectric and forms a thin channel for charge carriers that connect P3HT regions.

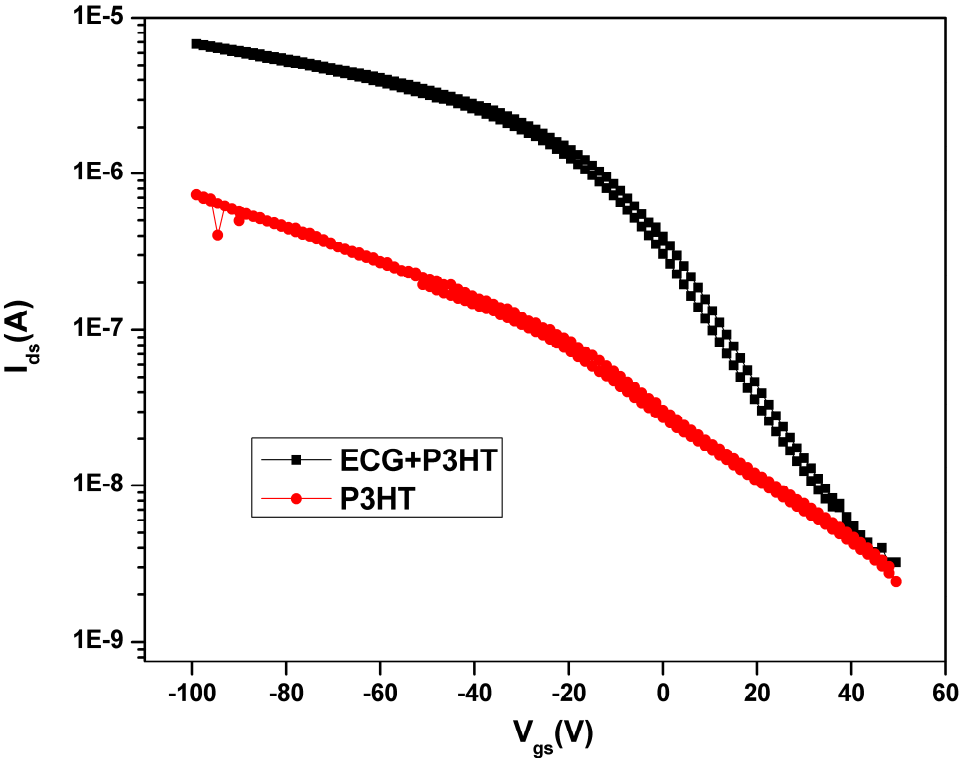


Figure 6.7: Comparison of the transfer characteristics in the linear regime of P3HT-based FETs ($100 \mu\text{m}$ and $5000 \mu\text{m}$) on a semilogarithmic plot with and without ECG flakes in the channel in the bottom-contact configuration. V_{gs} was varied from $+50$ to -100 V at constant $V_{\text{ds}}=-30 \text{ V}$.

In Fig. 6.7 we compare the transfer characteristics in the linear regime of a P3HT-based FETs ($100 \mu\text{m}$ and $5000 \mu\text{m}$) on a semilogarithmic plot with (black curve) and without ECG flakes (red curve) in the channel in the bottom-contact configuration. The linear mobility has increased from $2.2 \times 10^{-3} \text{ cm}^2/\text{Vs}$ to $0.033 \text{ cm}^2/\text{Vs}$. An order of magnitude increase in the mobility is due to presence of the ECG flakes in the channel. But these values are low relative to the top contact

geometry. It is well known fact that the performance of FETs with BC configuration is inferior to the performance of FETs with TC configuration. The metallic electrodes are hydrophilic and the SiO_2 is hydrophobic in nature. Due to the low surface energy of the gold electrodes, very small grains of OS are formed. Due to large surface energy difference between the electrode and gate dielectric, results in poor growth of OS layer on and close to metal/dielectric interface. The poor growth causes contact resistance and also results in lowering charge carrier mobility [202-205].

6.2 Graphene nanoribbons

In this section we present the transport properties of graphene nanoribbons (GNRs) on the microscopic level produced by cyclodehydrogenation of polyphenylene precursors. In this method, first a novel type of polyphenylene precursor with extremely high molecular weight was employed Diels-Alder polymerization. Then these precursors were graphitized into GNR by intramolecular oxidative cyclodehydrogenation. The average length of the resulting GNR is 60 nm and the width is 1.1 nm.

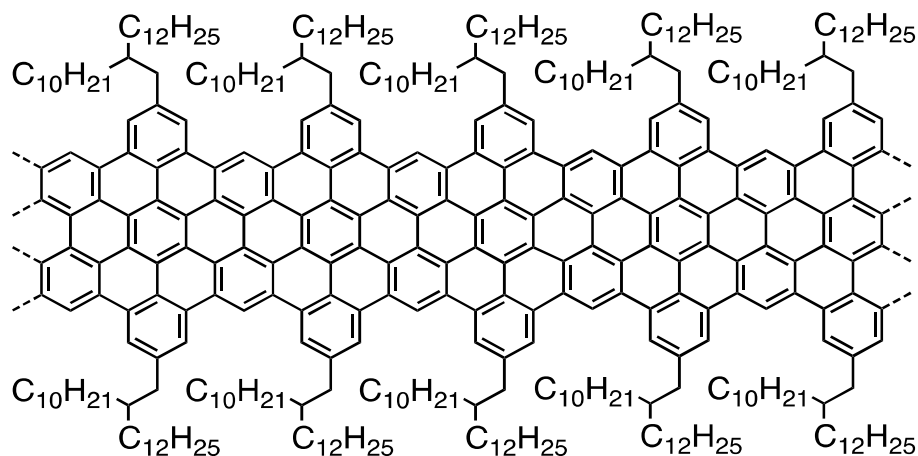


Figure 1.8: Molecular structure of graphene nanoribbon.

Molecular structure of graphene nanoribbon is shown in Fig. 1.8. The middle part of GNR is graphene and it is functionalized with alkyl chains at the edges in order to confine the charge carriers and create the energy band gap. The solubility of graphite is very poor, functionalization of graphene helps to improve its solubility.

6.2.1 Experimental

GNR powder was dissolved in ODCB at a concentration of 2 mg/ml and sonicated at 80 °C for 2 hours. The solution was then drop coated onto Si substrates covered with a SiO₂ layer of 230 nm thickness and having the interdigitated gold electrodes having a channel length 2.5 μm, 5 μm, 10 μm, 20 μm and width 1 cm. The resulting devices are tested and the results are presented in Figs. 6.9 and 6.10. For TOF measurements, the same GNR solution was drop coated onto fused silica substrates having coplanar gold electrodes of 25-nm thickness having a separation of 100 μm. The applied voltage is varied from +300 V to +500 V with a step of 100 V. The laser pulse width is 3 ns with a termination of 100 kΩ connected to the 2.5 GHz oscilloscope. The incident wavelength 530 nm is chosen corresponding to maximum absorption of GNRs (from Fig. 6.12) dissolved in ODCB and the TOF results are presented in Fig. 6.13.

6.2.2 Results and Discussion

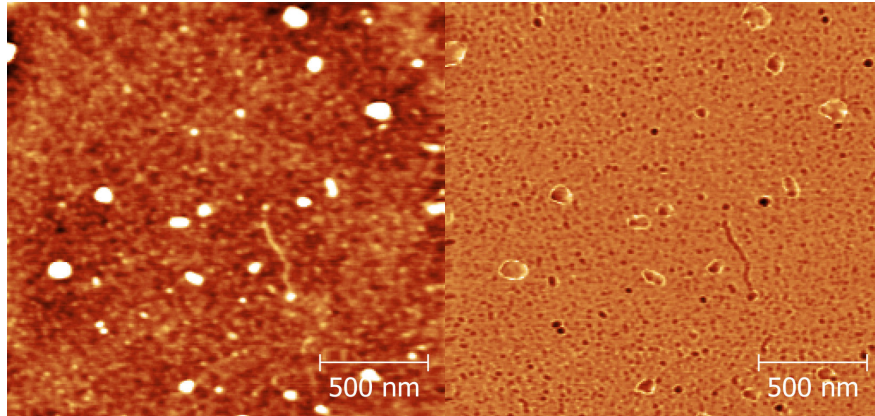


Figure 6.8: 2μm×2μm AFM image (left) and its phase image (right) of an isolated GNR on SiO₂ surface. The height scale is 0 to 4 nm.

In Fig. 6.8, we have presented the AFM image and phase image of an isolated GNR on SiO₂ surface. The length of the GNR is around 100 nm and the height is 1 nm. Due to poor solubility and poor sticking coefficient to SiO₂, these GNRs doesn't form continuous layer by spin coating method. Hence we drop coated the GNRs solution. In Fig. 6.9, we have presented output characteristics of GNRs dissolved in ODCB drop coated on Si/SiO₂ substrates for different V_{gs} having

channel length of 2.5 μm and 1 cm width at room temperature. V_{ds} is varied from 0 to -30 V for different gate voltages. V_{gs} increase at a step of 25 V. I_{ds} increases linearly with increasing V_{ds} and then saturates. The saturation voltage of V_{ds} increases with increasing V_{gs} . The output characteristics exhibits pronounced non-linearity at low V_{ds} from 0 to -5V. This non-linearity is due to severe contact resistance from the Au/GNR interface. At low V_{ds} , the voltage drop at the Au/GNR interface, as well as across the active layer is significant, causing thereby a significant reduction in current. As V_{ds} increases, contribution of the voltage drop at the Au/GNR interface becomes less important relative to the voltage drop across the active layer increases which results in an increase in I_{ds} .

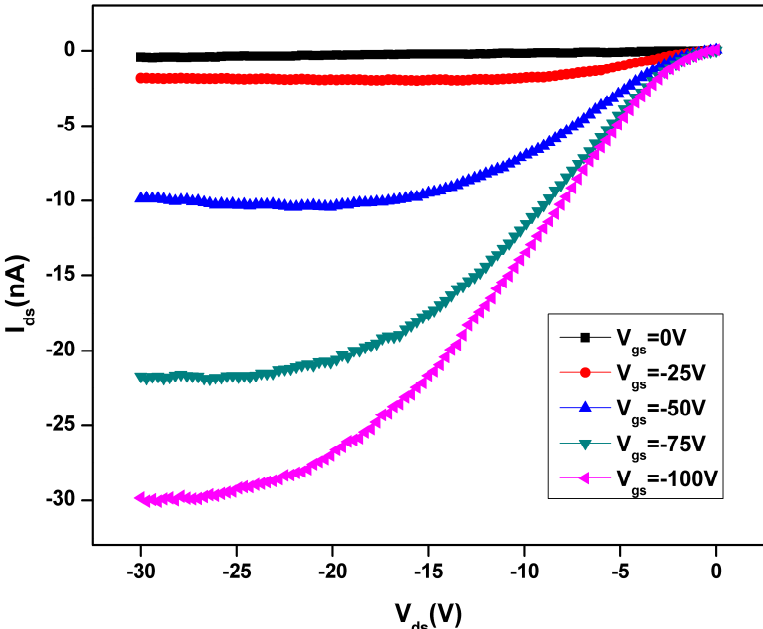


Figure 6.9: Output characteristics of GNRs dissolved in ODCB drop coated on Si/SiO₂ substrates for different V_{gs} of channel length 2.5 μm and 1cm width.

In Fig. 6.10, we have presented the transfer characteristics of GNRs at $V_{\text{ds}} = -30\text{ V}$ (linear regime). V_{gs} sweep starts from 0 to -100 V and then to +100 V and back to 0 V. Transfer characteristics show p-type behavior of GNRs, and strong hysteresis upon sweeping V_{gs} . This indicates the presence of trap sites and disorder within the layer. The threshold voltage in the forward direction is -15 V and in the backward direction is -80 V. The hysteresis is caused by the presence of traps on the OS/dielectric interface and due to alkyl chains on GNRs. When V_{gs} starts to increase from 0 V to -100V, holes start to fill the traps, and become immobilized, so that they

don't contribute to the current. When V_{gs} is switched back from -100 V to 100 V, I_{ds} decreases with decreasing V_{gs} , since the number of holes available for conduction are lower as they get trapped compared to forward sweep.

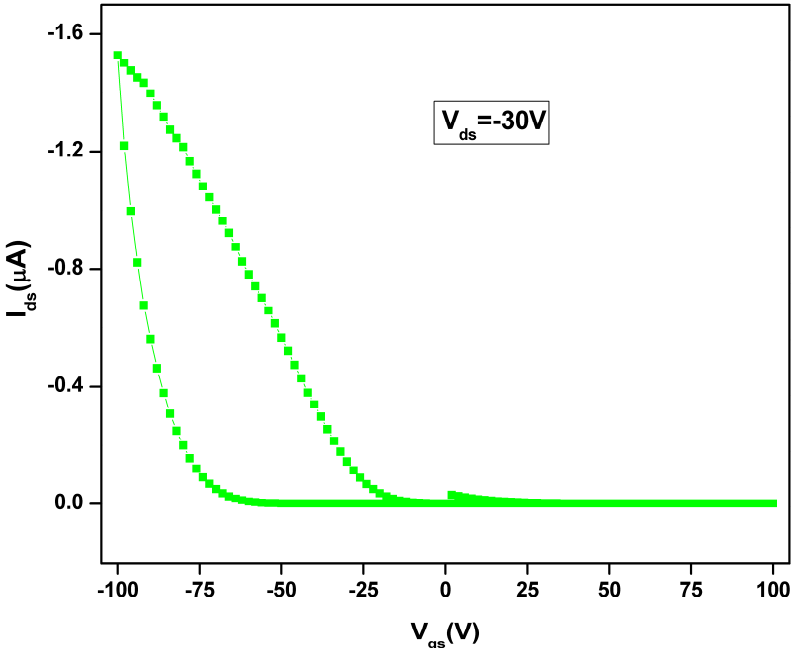


Figure 6.10: Transfer characteristics of GNRs at $V_{ds} = -30\text{ V}$. V_{gs} sweep starts from 0 to -100 V and then to +100 V and back to 0 V.

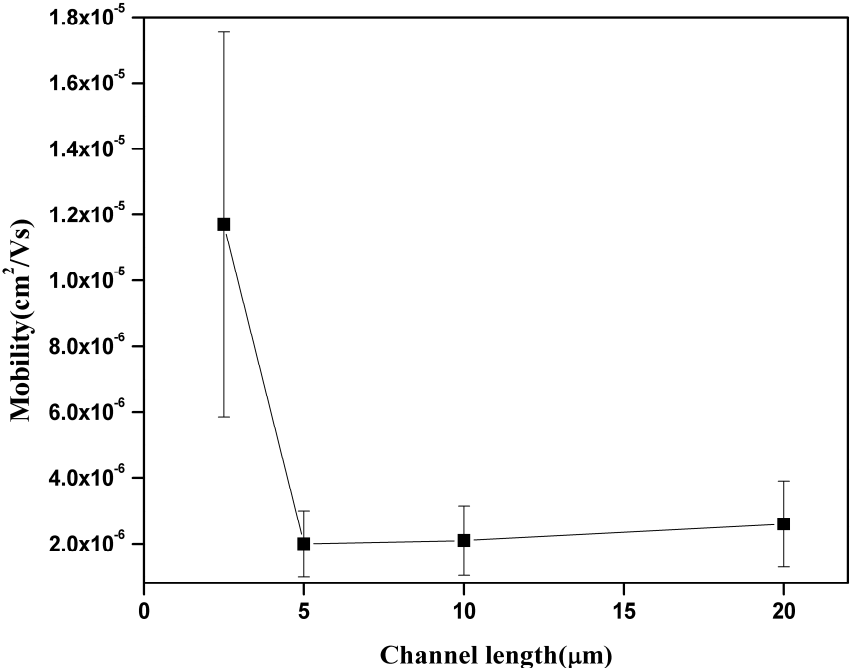


Figure 6.11: Variation of linear mobility as a function of channel length of GNRs.

Variation of the linear mobility as a function of channel length is shown in Fig. 6.11. We are aware that the mobility extracted from the hysteresis curves, leads to an error. However, in order to get an idea about the variation of the mobility at different channel lengths, we have estimated the mobility from these curves. We can observe that with increasing the channel length from 2.5 μm to 5 μm , the mobility is reduced. Non-contact time-resolved terahertz conductivity measurements reveal excellent charge-carrier mobility within individual GNRs [52]. But the mobility of these GNRs is relatively low on long channels. The GNRs are functionalized with alkyl chains at the edges, and these will acts as traps. This will prevent the charge carriers to flow from one GNR to another. As we increase the channel length, the number of GNRs increases as well as the number of traps also increases, which will reduce the mobility. At channel length 20 μm , the mobility is slightly raises again because of the low contact resistance. When channel length (L) is very large in the orders of several micrometers, the current limiting factor is only the channel resistance. Since, for longer channel FETs the contact resistance is low. For very small channel length FETs there exists the influence of the contact resistance on the device's total resistance, which is observed as the comparatively lower charge carrier mobility.

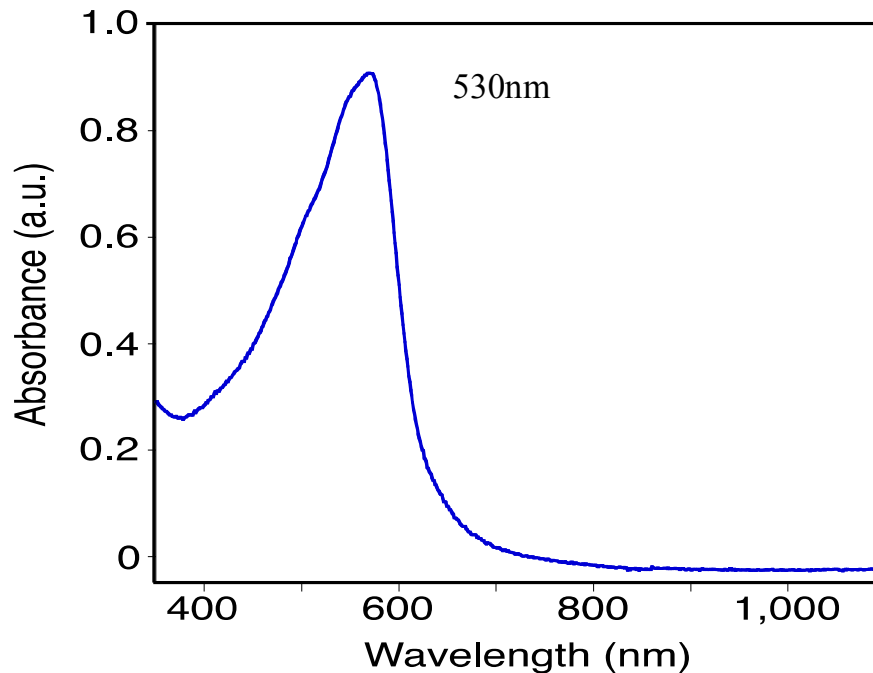


Figure 6.12: Absorption spectrum of GNRs dissolved in ODCB.

The absorption spectrum of GNRs dissolved in ODCB is shown in Fig. 6.12 and the maximum absorption peak is around 530 nm and an optical band gap of 2.34 eV. The TOF photocurrent results on GNRs are presented in Fig. 6.13 and reflect transport of holes across the channel.

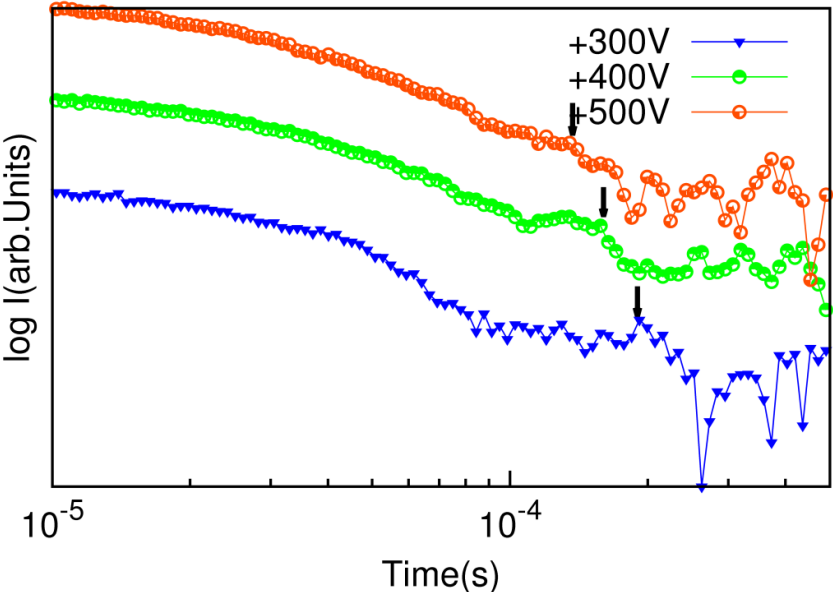


Figure 6.13: TOF measurements on GNRs on a double logarithmic scale. These curves are shifted vertically for clarity.

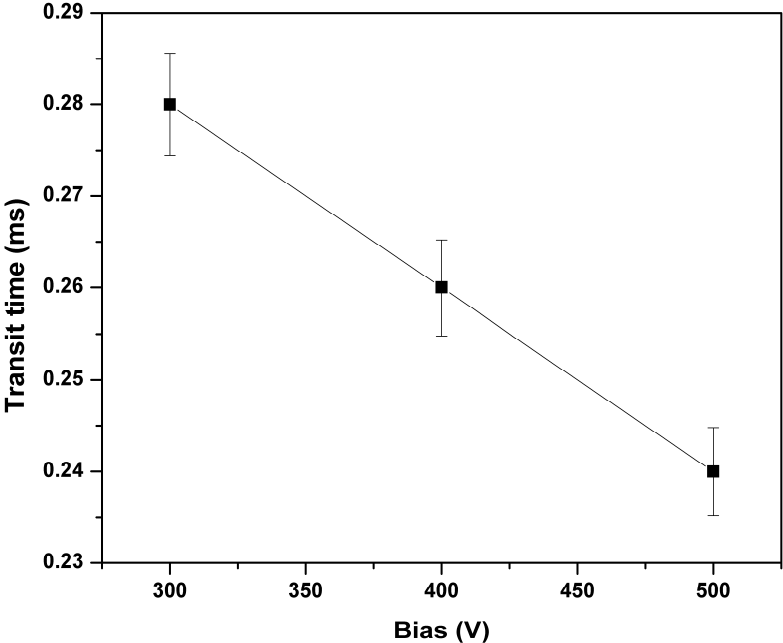


Figure 6.14. Variation of transit time as a function of applied bias. The extracted mobility is $2 \times 10^{-3} \text{ cm}^2/\text{Vs}$.

The initial surge of current in these curves is associated with initial fast acceleration of electrons in the high-field region near the bias electrode. $I(t)$ exhibits a small plateau with some noise followed by a sharp drop or cusp. The transit time is determined from the sharp drop of photocurrent and it is indicated by the arrows. The transit time shifted to shorter times with increasing the voltage, as expected. The variation of the transit time with the applied bias is shown in Fig. 6.14. The amount of photocurrent is low, since the absorption in GNRs is low. The mobility estimated from the constant field approximation is $2 \times 10^{-3} \text{ cm}^2/\text{Vs}$. This is nearly two orders of magnitude higher compared to FET mobility of GNRs. Since the charge carriers flow through the bulk of the film, thus avoids the effects of traps at the GNR/dielectric interface, which results in relatively high mobility compared to FETs.

6.3 Conclusions

The mobility of P3HT-based FETs has increased from $0.005 \text{ cm}^2/\text{Vs}$ to $0.2 \text{ cm}^2/\text{Vs}$ due to the incorporation of ECG flakes between the gate dielectric/OS interface. The remarkable increase in mobility over that of pristine P3HT is due to high conductivity of graphene, which are acting as conducting bridges, which will reduce the channel length.

The mobility of the GNRs decreases with increasing the channel length due to the alkyl chains presented at the ends, which acts as traps, prevents the charge transport from one GNR to another.

Chapter 7: Summary of the thesis

In recent years graphene has attracted a lot of attention due to its extraordinary properties. One of the alternative and scalable methods of its synthesis is based on the chemical exfoliation and reduction of graphite oxide. In this thesis, we have explored the electrical properties and charge transport properties of rGO by FETs and TOF technique.

In the first part of the thesis, the electrical properties of rGO and its modulation with different adsorbates are evaluated by FET characterization and by the TOF technique. rGO exhibits ambipolar transfer characteristics similar to mechanically exfoliated graphene. It exhibits room-temperature 2D conductivity of $0.5 \mu\text{S}$ and hole mobilities up to $1 \text{ cm}^2/\text{Vs}$ on Si/SiO₂ substrate. The mobilities estimated from the transfer characteristics and from I(t) curves obtained by TOF technique of rGO on Si/SiO₂ are in good agreement. The charge carrier transport is limited by the regions containing oxygen functionalities, defects and carbonyls. rGO shows two orders of magnitude higher conductivity ($32 \mu\text{S}$) on fused silica and sapphire substrates than on Si/SiO₂ substrates. The morphology of these rGO films characterized with AFM, and the difference in the conductivity is attributed to the morphological difference on these substrates. Various electron acceptor and electron donor molecules were studied on rGO surface both by the three terminal FET characterization and two terminal TOF techniques. P-type and n-type graphene was obtained using electron acceptor (PBA) and electron donor (TTF) via charge transfer doping. We have observed significant positive shift of the conductivity minimum in transfer characteristics upon exposing rGO-based FETs to PBA and 1-PSANa and the electron mobility decreases. The electron mobility is completely quenched when rGO-based FETs exposed to strong electron acceptors F4-TCNQ and TCNE. On the other hand, rGO-based FETs shows negative shift of the conductivity minimum upon exposing to TTF, which is a strong electron donor. In a similar way, I(t) curves shows shift in the transit time for electrons, when exposed to electron acceptor PBA. Conversely, upon exposure to electron donor i.e. TTF, shows effect on I(t) curves for holes. Our time-resolved photoconductivity measurements enable us to understand the charge transfer mechanism between rGO and adsorbates. From the I(t) curves we have observed changes in the mobility even at submonolayer coverages of dopant

molecules. Our time-resolved photoconductivity measurements have demonstrated that PBA coverages as low as 0.08% significantly affect charge transport in rGO. The effect of adsorbates on rGO shows strong dependence on the surface coverage and the applied electric field. We further compare the effect of weakly interacting Pyrene compound (1-PSANa) with the strongly interacting cyano group molecules compounds (TCNE and F4-TCNQ) with the same number of molecules on rGO surface in each deposition. 1-PSANa shows a small shift in the electron transit time. But the cyano group molecules are strongly interacting with rGO and cause a large shift in the electron transit time and also the changes the shape of the $I(t)$ curves. The shift in the transit time depends on the number of molecules present on the surface. The electron mobility increases for the first three depositions and slightly decreases at higher coverage. The behavior of the variation of the transit time explained from the theoretical calculations. At lower coverages, the charge transfer from graphene to the adsorbates is high. With increasing the coverage the charge transfer decreases from due to the negatively charged intermolecular interaction. Hence, the electron mobility decreases in the first three depositions and slightly recovers at higher coverages. The decrease in the electron mobility is due to the recombination of the electrons with the localized holes that result from the charge transfer from rGO to adsorbates. Therefore, charge transfer from graphene to adsorbate is of decisive significance in reducing the electron mobility. Among these molecules, F4-TCNQ shows effective p-type doping, as it shows large shift towards the positive gate voltages compared to 1-PSANa and TCNE and makes the determination of the transit time completely unreliable in the $I(t)$ curves. Since it contains strongly interacting cyano groups and also having additional four fluorine atoms compared to TCNE, which can accept additional electrons from graphene.

In the second part of the thesis, we have explored the possibility of using graphene flakes produced by different methods to improve the performance of OSs. In the first attempt, we have made blends of P3HT and graphene to enhance the mobility of P3HT-based FETs. The mobility of P3HT-based FETs increases from $0.003 \text{ cm}^2/\text{Vs}$ to $0.02 \text{ cm}^2/\text{Vs}$ at GNs concentration of 0.06 mg/ml , but the $I_{\text{on}}/I_{\text{off}}$ ratio decreases more than one order of magnitude. The increase in the mobility of P3HT is due to incorporation of GNs in the P3HT matrix. When the charge carriers enter these GNs, their transport becomes band-like and the overall charge carrier

mobility increases. With further increasing the concentration of GNs, the mobility starts to drop because of the contact resistance at the GN/P3HT interface due to mismatching of the energy levels. At higher concentration of GNs, the number of interconnecting junctions also increases, dominating the channel resistance and leads to poor mobility. With increasing the concentration of GNs, due to the formation of percolating networks I_{off} current starts to increase, since graphene has no bandgap. In addition to that, higher concentration of GNs leads to morphological changes and disrupts molecular ordering of the P3HT molecules and agglomeration of the graphene flakes leads to poor performance of the device.

In a similar way, we have added GNs to PDIF-CN2, which is high-mobility n-type semiconductor and we have increased the electron mobility as determined both by measuring the FETs transfer curve and by transient photoconductivity of thin films in coplanar electrode arrangement. The FET mobility increases from 10^{-4} cm^2/Vs in pristine PDIF-CN2 thin films to $0.2 \text{ cm}^2/\text{Vs}$ in thin films of GN:PDIF-CN2. The same improvement in mobility is observed from the TOF measurements. By exciting the carriers into the transporting states that reside higher in energy we have also demonstrated the existence of a high-electron-mobility channel comprising quasi-extended states within the blend, resulting in further increase in electron mobility. The mobility increases due to the incorporation of graphene flakes which acts as conducting bridges connecting the grains of OS. From these measurements we can conclude that the graphene can improve the mobility of OS, when the work function of graphene matches with the HOMO for a p-type OS and LUMO for an n-type OS. The mismatching of the energy levels leads to contact resistance at the GN/OS interface. At higher concentration of GNs, the number of interconnecting junctions increase, hence the contact resistance dominates the channel resistance and leads to poor performance of the device. We have further observed that at higher concentrations due to the incompatibility of OS and GNs, it disrupts the molecular ordering and leads to morphological changes.

In order to avoid the problem of percolating networks and to reduce the number of interconnecting junctions that are encountered with the GN/OS blends, we proposed an alternative approach to improve the mobility of OS. Since the charge flow takes place in the first few monolayers, we have placed mechanically exfoliated graphene flakes between the dielectric surface and the OS film. We demonstrated that

the effective mobility of the P3HT-based FETs could be enhanced as high as 100 times without reduction of the $I_{\text{on}}/I_{\text{off}}$ upon incorporation of graphene flakes in the channel of the device. The remarkable increase in the FET mobility of P3HT with graphene flakes over that of pristine P3HT is due to the incorporation of highly conductive graphene flakes between the source and drain electrodes, which are acting as conducting bridges and reduce the effective channel length of the device. In addition to that, this method also reduces the number of interconnecting junctions, since the flake size is several μm . But the low yield and poor controllability over the mechanically exfoliated graphene films is a severe problem for large-scale production of such devices.

In order to avoid the controllability problem, we have used single-layer graphene flakes produced by electrochemically exfoliation between the OS/dielectric interface, where we can control the size and surface coverage by dip coating method. The linear mobility of P3HT-based FETs has increased from $0.005 \text{ cm}^2/\text{Vs}$ to $0.2 \text{ cm}^2/\text{Vs}$ due to the incorporation of ECG flakes between the gate dielectric/OS interface. In addition to that, these flakes are p-type graphene due to chemical residues of the solvent, which will reduce the barrier for injection of holes from graphene into OS. Similar results were obtained in the BC configuration of P3HT-based FETs. However, the performance of these FETs is inferior in BC configuration compared to TC configuration due to the formation of poor thin growth on Au and Au/dielectric interface.

We also studied the channel length dependent mobility of GNRs on the microscopic level produced by intramolecular cyclodehydrogenation of polyphenylene precursors. The mobility decreases with increasing the channel length due to the presence of insulating alkyl chains at the edge of GNRs, which acts as traps, prevents the charge transport from one GNR to another. GNR-based FETs exhibit large amount of hysteresis, due to presence of interface traps at GNR/ SiO_2 , and the traps due to alkyl chains that are present at the edges of GNRs. The mobility estimated from the TOF measurements is relatively two orders of magnitude high compared to FET mobility, since these measurements avoids the effect of contacts and GNR/ SiO_2 interface effects, since the charge can flow through the bulk of the film.

List of publications:

- [1] S. R. Pathipati, E. Pavlica, E. Treossi, R. Rizzoli, G. P. Veronese, V. Palermo, L. Chen, D. Beljonne, J. M. Cai, R. Fasel, P. Ruffieux, and G. Bratina; Modulation of charge transport properties of reduced graphene oxide by submonolayer physisorption of an organic dye *Org. Electron.* **14**, 1787 (2013).
- [2] S. R. Pathipati, E. Pavlica, A. Schlierf, M. El Gemayel, P. Samorì, V. Palermo, and G. Bratina; Graphene-induced enhancement of n-type mobility in perylenediimide thin films (**In communication**).
- [3] S. R. Pathipati, E. Pavlica, E. Treossi, R. Rizzoli, G. P. Veronese, V. Palermo, and G. Bratina; The role of charge transfer at reduced graphene oxide/organic semiconductor interface on the charge transport properties (**To be communicated**).
- [4] S. R. Pathipati, E. Pavlica, R.B. Penumala and G. Bratina; The charge transport between graphene nanoflakes and organic semiconductor (**In manuscript**).

Appendix A

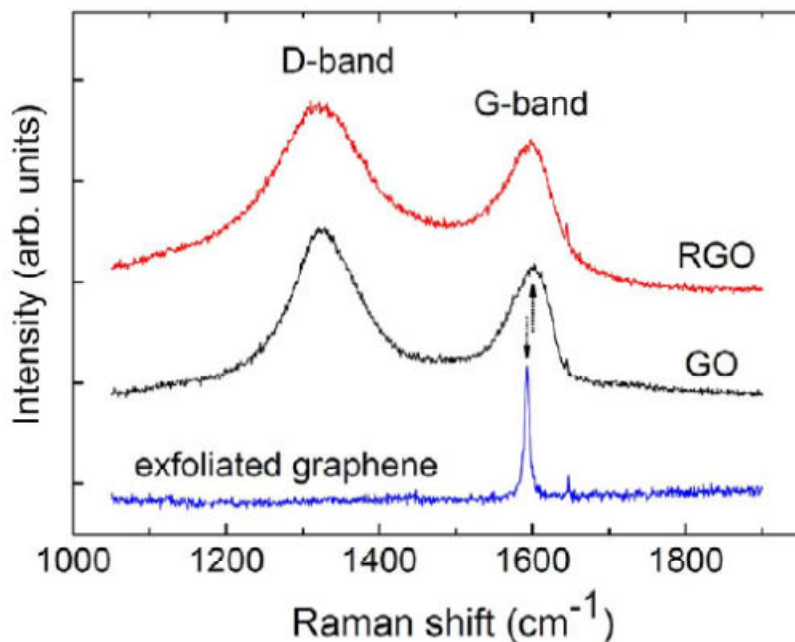


Figure A: The Raman spectra of GO, rGO and exfoliated graphene in the region of D- and G-band. The spectra were normalized to the G-band intensity. The arrows visualize the shift of the G-band.

Raman measurements were carried out with a micro-Raman spectrometer (Horiba Jobin-Yvon), using a 100× objective (laser spot diameter $\sim 1 \mu\text{m}$), with a spectral resolution of $\sim 1 \text{ cm}^{-1}$, laser excitation wavelength of 632.8 nm and power $\sim 4 \text{ mW}$. In Fig. A, we present the Raman spectra of the GO and rGO, together with the spectrum of conventional exfoliated graphene. The latter exhibits a sharp G-peak, while GO and rGO show wide D- and G-bands. We find that the G-band of both GO and rGO is shifted to higher frequencies with respect to the G-peak of exfoliated graphene, and this G-peak shift is usually related to doping by chemisorption or physisorption of molecules, ions, functional groups or metal particles, that can take place in the fabrication process of the GO. Moreover, we find that the overall Raman peak intensities are decreased after the thermal treatment, suggesting a partial loss of carbon during reduction. After reduction we observe a small increase of the intensity ratio $I(\text{D})/I(\text{G})$ (from 1.30 to 1.35), finding a similar trend the area ratio $A(\text{D})/A(\text{G})$. These observation show that GO and rGO feature a very similar degree of disorder; the reduction process, thus, does not re-establish the pristine graphenic lattice, but has the only function of restoring conjugation of the carbon bonds which survived to

the initial oxidation process. However, it is difficult to estimate the number of layers from the Raman measurements.

Appendix B

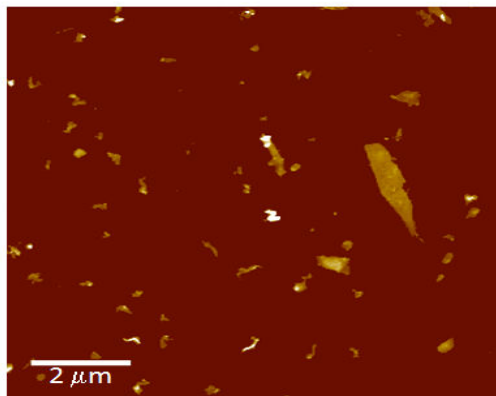


Figure B: AFM image of graphene exfoliated in 0.1 mg/ml PDIF-CN2 chloroform solution. Z-scale is 50 nm.

Fig. B shows the AFM topography image of a film prepared by spin-coating on SiO₂ a suspension obtained by liquid phase exfoliation of 3 mg/ml natural graphite flakes in 0.1 mg/ml PDIF-CN2 solutions in chloroform. It displays isolated graphene nanoflakes adsorbed on a flat substrate as evidenced in both the height image. Their lateral size spans from 200 nm to several μm, and their thickness varies from monolayer to multilayer's of nanoflakes.

Appendix C

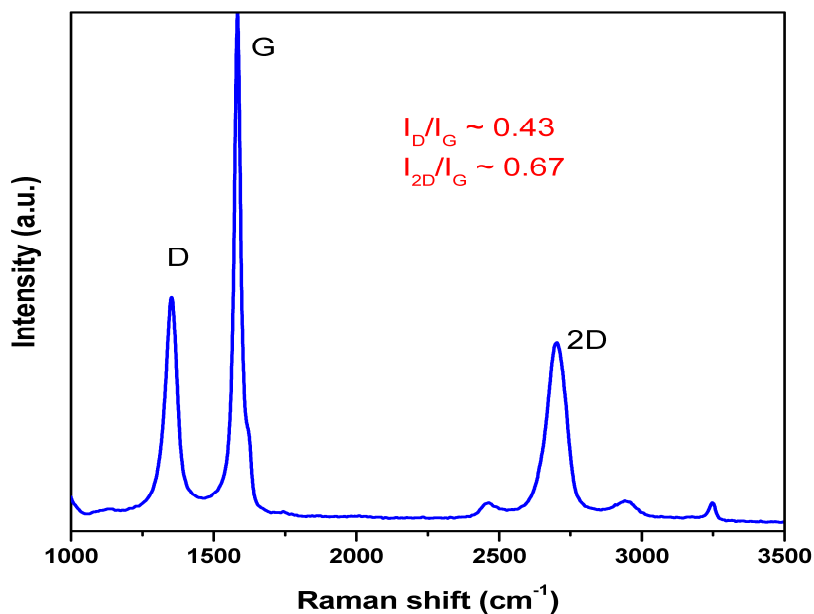


Figure C: Raman spectrum (excited by 488 nm laser) of a selected bilayer ECG sheet. The ratios of I_D/I_G and I_{2D}/I_G peaks are indicated.

The Raman spectra of a bilayer ECG sheet displayed an intense 2D and G peak at ~ 2710 and ~ 1586 cm^{-1} , respectively (Figure C). Moreover, a defect-related D peak was observed at ~ 1356 cm^{-1} . The intensity ratio of D to G (i.e., I_D/I_G) was calculated to be 0.43. This is much lower than that of chemically or thermally reduced GO (~ 1.2 to 1.5). The intensity ratio of 2D to G (i.e., I_{2D}/I_G) is normally related to the graphitization degree (for C=C sp^2 bonds) in graphitic carbons. The I_{2D}/I_G ratio (0.67) of bilayer ECG graphene sheets produced in this work is significantly higher than that of rGO, further suggesting the high quality of the ECG.

Appendix D

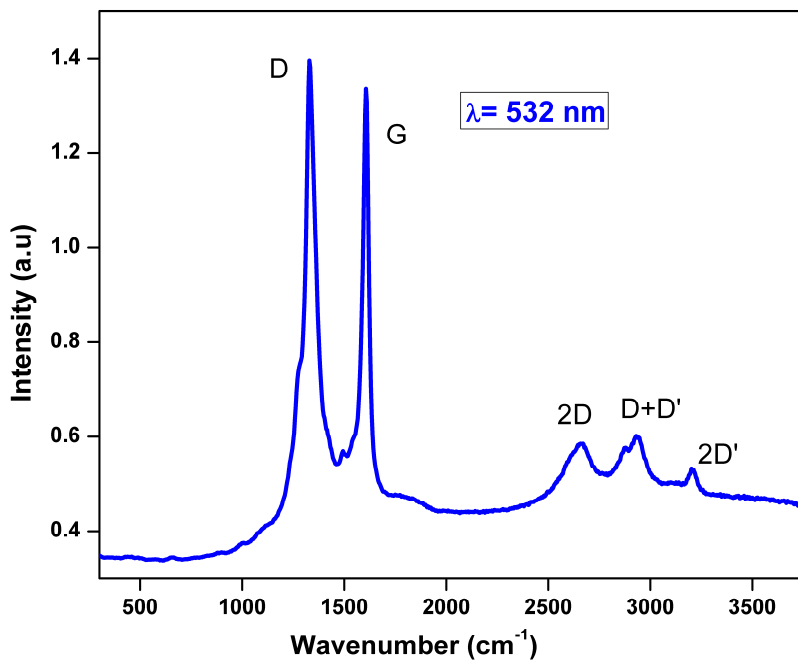


Figure D. Raman spectrum of GNR (532 nm, powder sample)

The Raman spectrum of GNR (532 nm, powder sample) is shown in Fig. D. The G peak is up-shifted ($\sim 1,605 \text{ cm}^{-1}$) and has a larger full width at half maximum ($\sim 25 \text{ cm}^{-1}$), which is expected from quantum confinement because this relaxes the Raman selection rule. The intense D peak is activated by the confinement of π -electrons into a finite-size domain.

References

1. H. W. Kroto, J. R. Heath, S. C. O'Brien, R. F. Curl, and R. E. Smalley, *Nature* **318**, 162 (1985).
2. S. Iijima, *Nature* **354**, 56 (1991).
3. K. S. Novoselov, A. K. Geim, S. V. Morozov, D. Jiang, Y. Zhang, S. V. Dubonos, I. V. Grigorieva, and A. A. Firsov, *Science* **306**, 666 (2004).
4. K. Geim and K. S. Novoselov, *Nat. Mater.* **6**, 183 (2007).
5. M. I. Katsnelson, *Mater. Today* **10**, 20 (2007).
6. P. R. Wallace, *Phys. Rev.* **71**, 622 (1947).
7. K. S. Novoselov, Z. Jiang, Y. Zhang, S. V. Morozov, H. L. Stormer, U. Zeitler, J. C. Maan, G. S. Boebinger, P. Kim, and A. K. Geim, *Science* **315**, 1379 (2007).
8. Y. B. Zhang, Y. W. Tan, H. L. Stormer, and P. Kim, *Nature* **438**, 201 (2005).
9. K. S. Novoselov, A. K. Geim, S. V. Morozov, D. Jiang, M. I. Katsnelson, I. V. Grigorieva, S. V. Dubonos, and A. A. Firsov, *Nature* **438**, 197 (2005).
10. F. Schedin, A. K. Geim, S. V. Morozov, E. W. Hill, P. Blake, M. I. Katsnelson, and K. S. Novoselov, *Nat. Mater.* **6**, 652 (2007).
11. X. Du, I. Skachko, A. Barker, and E. Y. Andrei, *Nat. Nanotechnol.* **3**, 491 (2008).
12. X. Liang, Z. Fu, and S. Y. Chou, *Nano Lett.* **7**, 3840 (2007).
13. L. Song, L. J. Ci, W. Gao, and P. M. Ajayan, *ACS Nano* **3**, 1353 (2009).
14. T. N'Diaye, J. Coraux, T. N. Plasa, C. Busse, and T. Michely, *New J. Phys.* **10** (2008).
15. P. W. Sutter, J. I. Flege, and E. A. Sutter, *Nat. Mater.* **7**, 406 (2008).
16. K. S. Kim, Y. Zhao, H. Jang, S. Y. Lee, J. M. Kim, J. H. Ahn, P. Kim, J. Y. Choi, and B. H. Hong, *Nature* **457**, 706 (2009).
17. N. Obraztsov, E. A. Obraztsova, A. V. Tyurnina, and A. A. Zolotukhin, *Carbon* **45**, 2017 (2007).
18. A. Reina, X. T. Jia, J. Ho, D. Nezich, H. B. Son, V. Bulovic, M. S. Dresselhaus, and J. Kong, *Nano Lett.* **9**, 30 (2009).

19. X. Li, W. Cai, J. An, S. Kim, J. Nah, D. Yang, R. Piner, A. Velamakanni, I. Jung, E. Tutuc, S. K. Banerjee, L. Colombo, and R. S. Ruoff, *Science* **324**, 1312 (2009).
20. S. Bae, H. Kim, Y. Lee, X. F. Xu, J. S. Park, Y. Zheng, J. Balakrishnan, T. Lei, H. R. Kim, Y. I. Song, Y. J. Kim, K. S. Kim, B. Ozyilmaz, J. H. Ahn, B. H. Hong, and S. Iijima, *Nat. Nanotechnol.* **5**, 574 (2010).
21. X. S. Li, C. W. Magnuson, A. Venugopal, J. H. An, J. W. Suk, B. Y. Han, M. Borysiak, W. W. Cai, A. Velamakanni, Y. W. Zhu, L. F. Fu, E. M. Vogel, E. Voelkl, L. Colombo, and R. S. Ruoff, *Nano Lett.* **10**, 4328 (2010).
22. M. P. Levendorf, C. S. Ruiz-Vargas, S. Garg, and J. Park, *Nano Lett.* **9**, 4479 (2009).
23. A. Mattevi, H. Kim, and M. Chhowalla, *J. Mater. Chem.* **21**, 3324 (2011).
24. D. C. Elias, R. V. Gorbachev, A. S. Mayorov, S. V. Morozov, A. A. Zhukov, P. Blake, L. A. Ponomarenko, I. V. Grigorieva, K. S. Novoselov, F. Guinea, and A. K. Geim, *Nat. Phys.* **7**, 701 (2011).
25. A. Dikin, S. Stankovich, E. J. Zimney, R. D. Piner, G. H. B. Dommett, G. Evmenenko, S. T. Nguyen, and R. S. Ruoff, *Nature* **448**, 457 (2007).
26. C. Gomez-Navarro, M. Burghard, and K. Kern, *Nano Lett.* **8**, 2045 (2008).
27. C. Botas, P. Alvarez, P. Blanco, M. Granda, C. Blanco, R. Santamaria, L. J. Romasanta, R. Verdejo, M. A. Lopez-Manchado, and R. Menendez, *Carbon* **65**, 156 (2013).
28. T. Chen, Baoqing Zeng, J. L. Liu, J. H. Dong, X. Q. Liu, Z. Wu, X. Z. Yang, and Z. M. Li, *J. Phys.: Con. Ser.* **188**, 012051 (2009).
29. H. L. Poh, F. Sanek, A. Ambrosi, G. J. Zhao, Z. Sofer, and M. Pumera, *Nanoscale* **4**, 3515 (2012).
30. S. Stankovich, D. A. Dikin, R. D. Piner, K. A. Kohlhaas, A. Kleinhammes, Y. Jia, Y. Wu, S. T. Nguyen, and R. S. Ruoff, *Carbon* **45**, 1558 (2007).
31. S. C. Youn, J. Geng, B. S. Son, S. B. Yang, D. W. Kim, H. M. Cho, and H. T. Jung, *J. Nanosci. Nanotechnol.* **11**, 5959 (2011).
32. H. A. Becerril, J. Mao, Z. Liu, R. M. Stoltenberg, Z. Bao, and Y. Chen, *ACS Nano* **2**, 463 (2008).

33. H. A. Becerril, R. M. Stoltenberg, M. L. Tang, M. E. Roberts, Z. F. Liu, Y. S. Chen, D. H. Kim, B. L. Lee, S. Lee, and Z. A. Bao, *ACS Nano* **4**, 6343 (2010).
34. Z. T. Luo, Y. Lu, L. A. Somers, and A. T. C. Johnson, *J. Am. Chem. Soc.* **131**, 898 (2009).
35. G. H. Lu, S. Park, K. H. Yu, R. S. Ruoff, L. E. Ocola, D. Rosenmann, and J. H. Chen, *ACS Nano* **5**, 1154 (2011).
36. H. J. Shin, K. K. Kim, A. Benayad, S. M. Yoon, H. K. Park, I. S. Jung, M. H. Jin, H. K. Jeong, J. M. Kim, J. Y. Choi, and Y. H. Lee, *Adv. Funct. Mater.* **19**, 1987 (2009).
37. G. X. Wang, J. Yang, J. Park, X. L. Gou, B. Wang, H. Liu, and J. Yao, *J. Phys. Chem. C* **112**, 8192 (2008).
38. Z. S. Wu, W. C. Ren, L. B. Gao, B. L. Liu, C. B. Jiang, and H. M. Cheng, *Carbon* **47**, 493 (2009).
39. M. J. Fernandez-Merino, L. Guardia, J. I. Paredes, S. Villar-Rodil, P. Solis-Fernandez, A. Martinez-Alonso, and J. M. D. Tascon, *J. Phys. Chem. C* **114**, 6426 (2010).
40. X. B. Fan, W. C. Peng, Y. Li, X. Y. Li, S. L. Wang, G. L. Zhang, and F. B. Zhang, *Adv. Mater.* **20**, 4490 (2008).
41. I. Jung, D. A. Dikin, R. D. Piner, and R. S. Ruoff, *Nano Lett.* **8**, 4283 (2008).
42. Y. Hernandez, V. Nicolosi, M. Lotya, F. M. Blighe, Z. Y. Sun, S. De, I. T. McGovern, B. Holland, M. Byrne, Y. K. Gun'ko, J. J. Boland, P. Niraj, G. Duesberg, S. Krishnamurthy, R. Goodhue, J. Hutchison, V. Scardaci, A. C. Ferrari, and J. N. Coleman, *Nat. Nanotechnol.* **3**, 563 (2008).
43. N. Liu, F. Luo, H. X. Wu, Y. H. Liu, C. Zhang, and J. Chen, *Adv. Funct. Mater.* **18**, 1518 (2008).
44. S. De, P. J. King, M. Lotya, A. O'Neill, E. M. Doherty, Y. Hernandez, G. S. Duesberg, and J. N. Coleman, *Small* **6**, 458 (2010).
45. X. L. Li, G. Y. Zhang, X. D. Bai, X. M. Sun, X. R. Wang, E. Wang, and H. J. Dai, *Nat. Nanotechnol.* **3**, 538 (2008).
46. K. Parvez, R. J. Li, S. R. Puniredd, Y. Hernandez, F. Hinkel, S. H. Wang, X. L. Feng, and K. Mullen, *ACS Nano* **7**, 3598 (2013).

47. A. Kumatani, Y. Li, P. Darmawan, T. Minari, and K. Tsukagoshi, *Sci. Rep.* **3** (2013).
48. Z. H. Chen, Y. M. Lin, M. J. Rooks, and P. Avouris, *Physica E* **40**, 228 (2007).
49. M. Y. Han, B. Ozyilmaz, Y. B. Zhang, and P. Kim, *Phys. Rev. Lett.* **98** (20) (2007).
50. V. Kosynkin, A. L. Higginbotham, A. Sinitskii, J. R. Lomeda, A. Dimiev, B. K. Price, and J. M. Tour, *Nature* **458**, 872 (2009).
51. X. L. Li, X. R. Wang, L. Zhang, S. W. Lee, and H. J. Dai, *Science* **319**, 1229 (2008).
52. A. Narita, X. Feng, Y. Hernandez, S. A. Jensen, M. Bonn, H. Yang, I. A. Verzhbitskiy, C. Casiraghi, M. R. Hansen, A. H. Koch, G. Fytas, O. Ivasenko, B. Li, K. S. Mali, T. Balandina, S. Mahesh, S. De Feyter, and K. Mullen, *Nat. Chem.* **6**, 126 (2014).
53. X. Y. Yang, X. Dou, A. Rouhanipour, L. J. Zhi, H. J. Rader, and K. Mullen, *J. Am. Chem. Soc.* **130**, 4216 (2008).
54. D. V. Kosynkin, W. Lu, A. Sinitskii, G. Pera, Z. Z. Sun, and J. M. Tour, *ACS Nano* **5**, 968 (2011).
55. M. Y. Han, B. Ozyilmaz, Y. B. Zhang, and P. Kim, *Phys. Rev. Lett.* **98** (20) (2007).
56. J. S. Wu, L. Gherghel, M. D. Watson, J. X. Li, Z. H. Wang, C. D. Simpson, U. Kolb, and K. Mullen, *Macromolecules* **36**, 7082 (2003).
57. M. Koch, F. Ample, C. Joachim, and L. Grill, *Nat. Nanotechnol.* **7**, 713 (2012).
58. X. Y. Yang, X. Dou, A. Rouhanipour, L. J. Zhi, H. J. Rader, and K. Mullen, *J. Am. Chem. Soc.* **130**, 4216 (2008).
59. Y. Fogel, L. J. Zhi, A. Rouhanipour, D. Andrienko, H. J. Rader, and K. Mullen, *Macromolecules* **42**, 6878 (2009).
60. L. Chen, Y. Hernandez, X. L. Feng, and K. Mullen, *Angew. Chem. Int. Ed.* **51**, 7640 (2012).
61. M. G. Schwab, A. Narita, Y. Hernandez, T. Balandina, K. S. Mali, S. De Feyter, X. L. Feng, and K. Mullen, *J. Am. Chem. Soc.* **134**, 18169 (2012).

62. L. Dossel, L. Gherghel, X. L. Feng, and K. Mullen, *Angew. Chem. Int. Ed.* **50**, 2540 (2011).
63. J. M. Cai, P. Ruffieux, R. Jaafar, M. Bieri, T. Braun, S. Blankenburg, M. Muoth, A. P. Seitsonen, M. Saleh, X. L. Feng, K. Mullen, and R. Fasel, *Nature* **466**, 470 (2010).
64. S. A. Jensen, R. Ulbricht, A. Narita, X. L. Feng, K. Mullen, T. Hertel, D. Turchinovich, and M. Bonn, *Nano Lett.* **13**, 5925 (2013).
65. H. M. Lv, H. Q. Wu, J. B. Liu, J. H. Yu, J. B. Niu, J. F. Li, Q. X. Xu, X. M. Wu, and H. Qian, *Appl. Phys. Lett.* **103**, 193102 (2013).
66. Meric, M. Y. Han, A. F. Young, B. Ozyilmaz, P. Kim, and K. L. Shepard, *Nat. Nanotechnol.* **3**, 654 (2008).
67. F. Young and P. Kim, *Nat. Phys.* **5**, 222 (2009).
68. T. O. Wehling, K. S. Novoselov, S. V. Morozov, E. E. Vdovin, M. I. Katsnelson, A. K. Geim, and A. I. Lichtenstein, *Nano Lett.* **8**, 173 (2008).
69. L. A. Majewski, R. Schroeder, and M. Grell, *Adv. Funct. Mater.* **15**, 1017 (2005).
70. D. Zielke, A. C. Hubler, U. Hahn, N. Brandt, M. Bartzsch, U. Fugmann, T. Fischer, J. Veres, and S. Ogier, *Appl. Phys. Lett.* **87**, 123508 (2005).
71. S. V. Novikov, *Russ. J. Electrochem.* **48**, 388 (2012).
72. L. B. Lin, C. W. Cheng, C. A. Dai, and Y. P. Lee, *J. Appl. Phys.* **112**, 073715 (2012).
73. W. E. Spear, *Proc. Phys. Soc. London, Sect. B* **70**, 669 (1957).
74. P. M. Borsenberger and H. Bässler, *J. Chem. Phys.* **95**, 5327 (1991)
75. P. M. Borsenberger, L. Pautmeier, and H. Bässler, *J. Chem. Phys.* **94**, 5447 (1991).
76. P. M. Borsenberger, L. Pautmeier, and H. Bässler, *J. Chem. Phys.* **95**, 1258 (1991).
77. P. M. Borsenberger, H. C. Kan, and W. B. Vreeland, *Phys. Stat. Sol. a-Appl. Res.* **142**, 489 (1994).
78. Y. Kanemitsu, H. Funada, and Y. Masumoto, *Appl. Phys. Lett.* **59**, 697 (1991).
79. P. M. Borsenberger and H. Bassler, *Phys. Status Solidi B* **170**, 291 (1992).
80. P. M. Borsenberger and L. J. Rossi, *J. Chem. Phys.* **96**, 2390 (1992).

81. Y. Kanemitsu, H. Funada, and Y. Masumoto, *J. Appl. Phys.* **71**, 300 (1992).
82. R. P. Rocha and J. A. Freire, *J. Appl. Phys.* **112**, 083717 (2012).
83. M. Vanderauweraer, F. C. Deschryver, P. M. Borsenberger, and H. Bäessler, *Adv. Mater.* **6**, 199 (1994).
84. T. Kreouzis, D. Poplavskyy, S. M. Tuladhar, M. Campoy-Quiles, J. Nelson, A. J. Campbell, and D. D. C. Bradley, *Phys. Rev. B* **73**, 235201 (2006).
85. H. Scher and E. W. Montroll, *Phys. Rev. B* **12**, 2455 (1975).
86. M. M. Perlman and S. Bamji, *Appl. Phys. Lett.* **33**, 581 (1978).
87. J. A. Freire and M. G. E. da Luz, *J. Chem. Phys.* **119**, 2348 (2003).
88. A. Lorincz and F. Belezny, *Solid State Commun.* **44**, 109 (1982).
89. H. Bassler, *Phys. Status Solidi B* **175**, 15 (1993).
90. A. J. Heeger, *Rev. Mod. Phys.* **73**, 681 (2001).
91. A. Pivrikas, G. Juska, R. Osterbacka, M. Westerling, M. Viliunas, K. Arlauskas, and H. Stubb, *Phys. Rev. B* **71**, 125205 (2005).
92. N. S. Sariciftci, L. Smilowitz, A. J. Heeger, and F. Wudl, *Science* **258**, 1474 (1992).
93. C. J. Brabec, N. S. Sariciftci, and J. C. Hummelen, *Adv. Funct. Mat.* **11**, 15 (2001).
94. K. J. Donovan and T. Kreouzis, *J. Appl. Phys.* **88**, 918 (2000).
95. A. J. Campbell, D. D. C. Bradley, and H. Antoniadis, *Appl. Phys. Lett.* **79**, 2133 (2001).
96. A. Pivrikas, G. Juska, K. Arlauskas, M. Scharber, A. Mozer, N. S. Sariciftci, H. Stubb, and R. Österbacka, 2005 (unpublished).
97. S. M. Sze, *Physics and Technology of the semiconductor devices*, John Wiley&sons, 2nd Edition (2001).
98. A. Binnig, C. F. Quate, and C. Gerber, *Phys. Rev. Lett.* **56**, 930 (1986).
99. T. R. Albrecht and C. F. Quate, *J. Vac. Sci. Technol. A* **6**, 271 (1988).
100. A. Binnig, C. Gerber, E. Stoll, T. R. Albrecht, and C. F. Quate, *Surf. Sci.* **189**, 1 (1987).
101. Y. Martin, C. C. Williams, and H. K. Wickramasinghe, *J. Appl. Phys.* **61**, 4723 (1987).
102. S. Morita, F.J. Giessibl, R. Wiesendanger, *Non contact atomic force microscopy*, Springer (2009).

103. X. Lv, Y. Huang, Z. B. Liu, J. G. Tian, Y. Wang, Y. F. Ma, J. J. Liang, S. P. Fu, X. J. Wan, and Y. S. Chen, *Small* **5**, 1682 (2009).
104. M. Wang, Y. H. Wu, C. X. Cong, J. Z. Shang, and T. Yu, *ACS Nano* **4**, 7221 (2010).
105. M. Lafkioti, B. Krauss, T. Lohmann, U. Zschieschang, H. Klauk, K. von Klitzing, and J. H. Smet, *Nano Lett.* **10**, 1149 (2010).
106. H. Xu, Y. B. Chen, J. Zhang, and H. L. Zhang, *Small* **8**, 2833 (2012).
107. Z. Liu, A. A. Bol, and W. Haensch, *Nano Lett.* **11**, 523 (2011).
108. X. Wang, J. B. Xu, C. Wang, J. Du, and W. Xie, *Adv. Mater.* **23**, 2464 (2011).
109. Z. Yan, Z. Z. Sun, W. Lu, J. Yao, Y. Zhu, and J. M. Tour, *ACS Nano* **5**, 1535 (2011).
110. H. Castro Neto, F. Guinea, N. M. R. Peres, K. S. Novoselov, and A. K. Geim, *Rev. Mod. Phys.* **81**, 109 (2009).
111. H. Liu, Y. Liu, and D. Zhu, *J. Mater. Chem.* **21**, 3335 (2011).
112. X. Dong, D. Fu, W. Fang, Y. Shi, P. Chen, and L. J. Li, *Small* **5**, 1422 (2009).
113. R. Ishikawa, M. Bando, Y. Morimoto, and A. Sandhu, *Nanoscale Res. Lett.* **6**, 111 (2011).
114. M. Kim, N. S. Safron, C. Huang, M. S. Arnold, and P. Gopalan, *Nano Lett.* **12**, 182 (2012).
115. D. B. Farmer, R. Golizadeh-Mojarad, V. Perebeinos, Y. M. Lin, G. S. Tulevski, J. C. Tsang, and P. Avouris, *Nano Lett.* **9**, 388 (2009).
116. T. Hu and I. C. Gerber, *J. Phys. Chem. C* **117**, 2411 (2013).
117. F. Yavari, C. Kritzing, C. Gaire, L. Song, H. Gulapalli, T. Borca-Tasciuc, P. M. Ajayan, and N. Koratkar, *Small* **6**, 2535 (2010).
118. S.-M. Park, S.-N. Yang, H.-S. Lim, and H.-G. Lee, *Bull. Korean Chem. Soc.* **32**, 2199 (2011).
119. X. Q. Tian, J. B. Xu, and X. M. Wang, *J. Phys. Chem. B* **114**, 11377 (2010).
120. C. Coletti, C. Riedl, D. S. Lee, B. Krauss, L. Patthey, K. von Klitzing, J. H. Smet, and U. Starke, *Phys. Rev. B* **81**, 235401 (2010).
121. Y.-C. Lin, C.-Y. Lin, and P.-W. Chiu, *Appl. Phys. Lett.* **96**, 133110 (2010).
122. B. Guo, Q. Liu, E. Chen, H. Zhu, L. Fang, and J. R. Gong, *Nano Lett.* (2010).

123. P. L. Levesque, S.S. Sabri, C.M. Aguirre, J. Guillemette, M. Siaj, P. Desjardins, T. Szkopek, R. Martel, *Nano Lett.* **11**, 132 (2011).
124. H. Xu, Z. Zhang, H. Xu, Z. Wang, S. Wang, L.-M. Peng, *ACS Nano* **5**, 5031 (2011).
125. S. Adam, E.H. Hwang, V.M. Galitski, S. Das Sarma, *Proc. Natl. Acad. Sci. U.S.A.* **104**, 18392 (2007).
126. F. Schedin, A.K. Geim, S.V. Morozov, E.W. Hill, P. Blake, M.I. Katsnelson, K.S. Novoselov, *Nat. Mater.* **6**, 652 (2007).
127. Z. Liu, A.A. Bol, W. Haensch, *Nano Lett.* **11**, 523 (2011).
128. C.-J. Shih, G.L.C. Paulus, Q.H. Wang, Z. Jin, D. Blankschtein, M.S. Strano, *Langmuir* **28**, 8579 (2012).
129. A. Bagri, C. Mattevi, M. Acik, Y.J. Chabal, M. Chhowalla, V.B. Shenoy, *Nat. Chem.* **2**, 581 (2010).
130. K. Erickson, R. Erni, Z. Lee, N. Alem, W. Gannett, A. Zettl, *Adv. Mater.* **22**, 4467 (2010).
131. C. Mattevi, G. Eda, S. Agnoli, S. Miller, K.A. Mkhoyan, O. Celik, D. Mastrogiovanni, G. Granozzi, E. Garfunkel, M. Chhowalla, *Adv. Funct. Mat.* **19**, 2577 (2009).
132. C. Gómez-Navarro, R. T. Weitz, A. M. Bittner, M. Scolari, A. Mews, M. Burghard, and K. Kern, *Nano Lett.* **7**, 3499 (2007).
133. G. Lee, K.S. Kim, K. Cho, *J. Phys. Chem. C* **115**, 9719 (2011).
134. A. Liscio, G.P. Veronese, E. Treossi, F. Suriano, F. Rossella, V. Bellani, R. Rizzoli, P. Samorì, V. Palermo, *J. Mater. Chem.* **21**, 2924 (2011).
135. M.K. Shin, B. Lee, S.H. Kim, J.A. Lee, G.M. Spinks, S. Gambhir, G.G. Wallace, M.E. Kozlov, R.H. Baughman, S.J. Kim, *Nat. Commun.* **3**, 650 (2012).
136. J.-H. Jang, D. Rangappa, Y.-U. Kwon, I. Honma, *J. Mater. Chem.* **21**, 3462 (2011).
137. X. Dong, C.-Y. Su, W. Zhang, J. Zhao, Q. Ling, W. Huang, P. Chen, L.-J. Li, *Phy. Chem. Chem. Phy* **12**, 2164 (2010).
138. Y. Xu, H. Bai, G. Lu, C. Li, G. Shi, *J. Am. Chem. Soc.* **130**, 5856 (2008).
139. S. Myung, A. Solanki, C. Kim, J. Park, K.S. Kim, K.-B. Lee, *Adv. Mater.* **23**, 2221 (2011).

140. G. Kresse, J. Furthmüller, *Comp. Mater. Sci.* **6**, 15 (1996).
141. G. Kresse, J. Hafner, *Phys. Rev. B* **47**, 558 (1993).
142. G. Kresse, J. Hafner, *Phys. Rev. B* **49**, 14251 (1994).
143. J. P. Perdew, K. Burke, M. Ernzerhof, *Phys. Rev. Lett.* **77**, 3865 (1996).
144. S. Grimme, *J. Comput. Chem.* **27**, 1787 (2006).
145. E. Pavlica, G. Bratina, *Phys. Stat. Sol. B* **243**, 473 (2006).
146. E. Pavlica, G. Bratina, *J. Phys. D: Appl. Phys.* **41**, 135109 (2008).
147. E. Pavlica, G. Bratina, *Appl. Phys. Lett.* **101**, 093304 (2012).
148. E. Treossi, M. Melucci, A. Liscio, M. Gazzano, P. Samorì, V. Palermo, *J. Am. Chem. Soc.* **131**, 15576 (2009).
149. Y. W. Tan, Y. Zhang, K. Bolotin, Y. Zhao, S. Adam, E.H. Hwang, S. Das Sarma, H.L. Stormer, P. Kim, *Phys. Rev. Lett.* **99**, 246803 (2007).
150. S. Ryu, L. Liu, S. Berciaud, Y.-J. Yu, H. Liu, P. Kim, G.W. Flynn, L.E. Brus, *Nano Lett.* **10**, 4944 (2010).
151. T. Ando, *Rev. Mod. Phys.* **54**, 437 (1982).
152. P. M. Borsenberger, R. Richert, H. Bässler, *Phys. Rev. B* **47**, 4289 (1993).
153. P. Borsenberger, L. Pautmeier, H. Bässler, *Phys. Rev. B* **46**, 12145 (1992).
154. L. Chen, L. Wang, Z. Shuai, and D. Beljonne, *J. Phys. Chem. Lett.* **4**, 2158 (2013).
155. L. Zuppiroli, M. N. Bussac, S. Paschen, O. Chauvet, and L. Forro, *Phys. Rev. B* **50**, 5196 (1994).
156. J. Akesson, O. Sundborg, O. Wahlstrom, and E. Schroder, *J. Chem. Phys.* **137**, 174702 (2012).
157. H. Yang, Y. Hernandez, A. Schlierf, A. Felten, A. Eckmann, S. Johal, P. Louette, J. J. Pireaux, X. Feng, K. Muellen, V. Palermo, and C. Casiraghi, *Carbon* **53**, 357 (2013).
158. A. Schlierf, H. F. Yang, E. Gebremedhn, E. Treossi, L. Ortolani, L. P. Chen, A. Minoia, V. Morandi, P. Samorì, C. Casiraghi, D. Beljonne, and V. Palermo, *Nanoscale* **5**, 4205 (2013).
159. R. Voggu, B. Das, C. S. Rout, and C. N. R. Rao, *J. Phys.: Condens. Matter* **20**, 472204 (2008).
160. D. J. Late, A. Ghosh, B. Chakraborty, A. K. Sood, U. V. Waghmare, and C. N. R. Rao, *J. Exp. Nanosci.* **6**, 641 (2011).

161. D. Choudhury, B. Das, D. D. Sarma, and C. N. R. Rao, *Chem. Phys. Lett.* **497**, 66 (2010).
162. Y. H. Lu, W. Chen, Y. P. Feng, and P. M. He, *J. Phys. Chem. B* **113**, 2 (2009).
163. H. Pinto, R. Jones, J. P. Goss, and P. R. Briddon, *J. Phys.: Condens. Matter* **21**, 402001 (2009).
164. X. M. Wang, J. B. Xu, W. G. Xie, and J. Du, *J. Phys. Chem. C* **115**, 7596 (2011).
165. W. Chen, S. Chen, D. C. Qi, X. Y. Gao, and A. T. S. Wee, *J. Am. Chem. Soc.* **129**, 10418 (2007).
166. J. Park, S. B. Jo, Y. J. Yu, Y. Kim, J. W. Yang, W. H. Lee, H. H. Kim, B. H. Hong, P. Kim, K. Cho, and K. S. Kim, *Adv. Mater.* **24**, 407 (2011).
167. C. J. Shih, G. L. C. Paulus, Q. H. Wang, Z. Jin, D. Blankschtein, and M. S. Strano, *Langmuir* **28**, 8579 (2012).
168. Y. D. Park, J. A. Lim, J. A. Yunseok, M. Hwang, H. S. Lee, D. H. Lee, H. J. Lee, J. B. Baek, and K. Cho, *Org. Electron.* **9**, 317 (2008).
169. X. Z. Bo, C. Y. Lee, M. S. Strano, M. Goldfinger, C. Nuckolls, and G. B. Blanchet, *Appl. Phys. Lett.* **86**, 182102 (2005).
170. S. H. Liu, S. C. B. Mannsfeld, M. C. LeMieux, H. W. Lee, and Z. N. Bao, *Appl. Phys. Lett.* **92**, 053306 (2008).
171. X. Z. Bo, N. G. Tassi, C. Y. Lee, M. S. Strano, C. Nuckolls, and G. B. Blanchet, *Appl. Phys. Lett.* **87**, 203510 (2005).
172. J. Geng, B.-S. Kong, S. B. Yang, S. C. Youn, S. Park, T. Joo, and H.-T. Jung, *Adv. Funct. Mater.* **18**, 2659 (2008).
173. J. Huang, D. R. Hines, B. J. Jung, M. S. Bronsgeest, A. Tunnell, V. Ballarotto, H. E. Katz, M. S. Fuhrer, E. D. Williams, and J. Cumings, *Org. Electron.* **12**, 1471 (2011).
174. X. Li, A. Kadashchuk, I. I. Fishchuk, W. T. T. Smaal, G. Gelinck, D. J. Broer, J. Genoe, P. Heremans, and H. Bässler, *Phys. Rev. Lett.* **108**, 066601 (2012).
175. P. Kumar, S. C. Jain, V. Kumar, S. Chand, and R. P. Tandon, *Appl. Phys. A* **94**, 281 (2009).
176. B. A. Jones, M. J. Ahrens, M.-H. Yoon, A. Facchetti, T. J. Marks and M. R. Wasielewski, *Angew. Chem. Int. Ed. Engl.* **43**, 6363 (2004).

177. S. Molinari, H. Alves, Z. Chen, A. Facchetti and A. F. Morpurgo, *J. Am. Chem. Soc.* **131**, 2462 (2009).
178. K. Willa, R. Häusermann, T. Mathis, A. Facchetti, Z. Chen and B. Batlogg, *J. Appl. Phys.* **113**, 133707 (2013).
179. C. Piliago, F. Cordella, D. Jarzab, S. Lu, Z. Chen, A. Facchetti and M. A. Loi, *Appl. Phys. A* **95**, 303 (2008).
180. C. Piliago, D. Jarzab, G. Gigli, Z. Chen, A. Facchetti and M. A. Loi, *Adv. Mater.* **21**, 1573 (2009).
181. S. Fabiano, H. Wang, C. Piliago, C. Jaye, D. A. Fischer, Z. Chen, B. Pignataro, A. Facchetti, Y.-L. Loo and M. A. Loi, *Adv. Funct. Mater.* **21**, 4479 (2011).
182. C. Piliago, F. Cordella, D. Jarzab, S. Lu, Z. Chen, A. Facchetti and M. Loi, *Appl. Phys. A* **95**, 303 (2009).
183. N. A. Minder, S. Ono, Z. Chen, A. Facchetti and A. F. Morpurgo, *Adv. Mater.* **24**, 503 (2012).
184. L. Pautmeier, R. Richert and H. Bässler, *Philos. Mag. B* **63**, 587 (1991).
185. P. Borsenberger, L. Pautmeier and H. Bässler, *Phys. Rev. B* **46**, 12145 (1992).
186. H. Bässler, *Phys. Status Solidi B* **175**, 15 (1993).
187. V. Arkhipov, E. Emelianova, P. Heremans and H. Bässler, *Phys. Rev. B* **72** (2005).
188. L. Sorba, G. Bratina, A. Antonini, A. Franciosi, L. Tapfer, A. Migliori and P. Merli, *Phys. Rev. B* **46**, 6834 (1992).
189. R. Yan, Q. Zhang, W. Li, I. Calizo, T. Shen, C. A. Richter, A. R. Hight-Walker, X. Liang, A. Seabaugh, D. Jena, H. G. Xing, D. J. Gundlach and N. V. Nguyen, *Appl. Phys. Lett.* **101**, 022105 (2012).
190. B. A. Jones, A. Facchetti, M. R. Wasielewski, and T. J. Marks, *J. Am. Chem. Soc.* **129**, 15259 (2007).
191. M. Kin Fai, J. Long, W. Feng and T. F. Heinz, *Solid State Commun.* **152**, 1341 (2012).
192. V. G. Kravets, A. N. Grigorenko, R. R. Nair, P. Blake, S. Anissimova, K. S. Novoselov and A. K. Geim, *Phys. Rev. B* **81**, 155413 (2010).

193. K. F. K. Mak, C. H. C. Lui, J. J. Shan and T. F. T. Heinz, *Phys. Rev. Lett.* **102**, 256405 (2009).
194. K. F. Mak, J. Shan and T. F. Heinz, *Phys. Rev. Lett.* **106**, 046401 (2011).
195. A. Pirkle, J. Chan, A. Venugopal, D. Hinojos, C. W. Magnuson, S. McDonnell, L. Colombo, E. M. Vogel, R. S. Ruoff, and R. M. Wallace, *Appl. Phys. Lett.* **99**, 122108 (2011).
196. T. Muck, V. Wagner, U. Bass, M. Leufgen, J. Geurts, and L. W. Molenkamp, *Synth. Met.* **146**, 317 (2004).
197. F. Dinelli, M. Murgia, P. Levy, M. Cavallini, F. Biscarini, and D. M. de Leeuw, *Phys. Rev. Lett.* **92** (11), 116802 (2004).
198. Ç. Ö. Girit, J. C. Meyer, R. Erni, M. D. Rossell, C. Kisielowski, L. Yang, C.-H. Park, M. F. Crommie, M. L. Cohen, S. G. Louie, and A. Zettl, *Science* **323**, 1705 (2009).
199. C. Gómez-Navarro, R. T. Weitz, A. M. Bittner, M. Scolari, A. Mews, M. Burghard, and K. Kern, *Nano Lett.* **7**, 3499 (2007).
200. T. Kobayashi, N. Kimura, J. Chi, S. Hirata, and D. Hobar, *Small* **6**, 1210 (2010).
201. E. W. J. Mitchell and J. W. Mitchell, *Proc. R. Soc. London, Ser. A* **210**, 70 (1951).
202. C. D. Dimitrakopoulos and D. J. Masecaro, *IBM J. Res. Dev.* **45**, 11 (2001).
203. L. Bürgi, T. J. Richards, R. H. Friend, and H. Sirringhaus, *J. Appl. Phys.* **94**, 6129 (2003).
204. J. A. Nichols, D. J. Gundlach, and T. N. Jackson, *Appl. Phys. Lett.* **83**, 2366 (2003).
205. N. Yoneya, M. Noda, N. Hirai, K. Nomoto, M. Wada, and J. Kasahara, *Appl. Phys. Lett.* **85**, 4663 (2004).
206. M. Kiguchi, M. Nakayama, T. Shimada, and K. Saiki, *Phys. Rev. B* **71**, 035332 (2005).
207. C.-Y. Huang, S.-Y. Lin, S.-S. Cheng, S.-T. Chou, C.-Y. Yang, T.-M. Ou, M.-C. Wu, I.-M. Chan, and Y.-J. Chan, *J. Vac. Sci. Technol., A* **25**, 43 (2007).
208. K. A. Singh, G. Sauvé, R. Zhang, T. Kowalewski, R. D. McCullough, and L. M. Porter, *Appl. Phys. Lett.* **92**, 263303 (2008).

209. W. Zhu, T. Low, V. Perebeinos, A. A. Bol, Y. Zhu, H. Yan, J. Tersoff, and P. Avouris, *Nano Lett.* **12**, 3431 (2012).
210. M. Kitamura and Y. Arakawa, *J. Phys.: Condens. Matter* **20**, 184011 (2008).
211. M. N. Nordin, K. N. Bourdakos, and R. J. Curry, *Phy. Chem. Chem. Phy* **12**, 7371 (2010).
212. M. Pope and E. C. Swenberg, *Electronic Processes in Organic Crystals and Polymers.* (Oxford University Press, Oxford, 1999)
213. K. J. Tielrooij, J. C. W. Song, S. A. Jensen, A. Centeno, A. Pesquera, A. Zurutuza Elorza, M. Bonn, L. S. Levitov and F. H. L. Koppens, *Nat. Phys.* **9**, 248 (2013).
214. W. Shockley, *J. Appl. Phys.* **9**, 635 (1938).
215. S. Ramo, *Proc. IRE* **27**, 584 (1939).